Title
Symmetry-Allowed Spin-Orbit Coupling in Quantum Materials

Author
Gotlieb, Kenneth H.

Publication Date
2017

Peer reviewed|Thesis/dissertation

Symmetry-Allowed Spin-Orbit Coupling in Quantum Materials

By

Kenneth H. Gotlieb

A dissertation submitted in partial satisfaction of the

requirements for the degree of

Doctor of Philosophy

in

Engineering - Applied Science and Technology

in the

Graduate Division

of the

University of California, Berkeley

Committee in charge:

Professor Alessandra Lanzara, Chair
Professor James Analytis
Professor Dung-Hai Lee

Fall 2017

Symmetry-Allowed Spin-Orbit Coupling in Quantum Materials

by

Kenneth H. Gotlieb

Abstract

Symmetry-Allowed Spin-Orbit Coupling in Quantum Materials

by

Kenneth H. Gotlieb

Doctor of Philosophy in Engineering - Applied Science and Technology

University of California, Berkeley

Professor Alessandra Lanzara, Chair

Strong interaction between the spin and orbital angular momentum of electrons in a material can give that material unusual quantum properties beyond what can be described by textbook band theory. It can lift the spin degeneracy of electronic bands and create a spin-momentum locking that can be a lever for electrical control of a material's magnetism. It creates a new state of matter: topological insulators, by twisting the energy ordering of electronic states. It adds complexity to how light interacts with the material, enabling some means for pointing photoelectron spins in a chosen direction.

However, the way spin-orbit coupling is manifested in a material is shaped by the symmetries of the crystal. In presenting findings from topological insulators, this dissertation demonstrates how those symmetries can force a material to have multiple spin textures in momentum space, each coupled to a distinct atomic orbital. Further, it shows how changes to those symmetries can eliminate those orbital-dependent spin textures and leave a single overall spin texture. Lastly, it shows how symmetries can allow crystals to harbor hidden spin textures in certain parts of their real space unit cells even when the overall band structure is spin degenerate. This last point is demonstrated in a cuprate high temperature superconductor, in which the newly discovered spin structure could have profound implications for the nature of superconductivity.

The results presented in this dissertation come from spin- and angle-resolved photoemission measurements of several quantum materials using a uniquely efficient and high resolution spectrometer. The details of how the spectrometer works when coupled with a laboratory-based laser and how that enables new experiments that were otherwise infeasible are given.

This dissertation is organized into six chapters. Chapter 1 reviews atomic spin-orbit coupling and ways it can influence the properties of materials. Chapter 2 explains spin- and angle-resolved photoemission and the unique instrumentation used for experiments in this work. Chapter 3 details experiments that show how spin textures in materials can couple to different orbitals. Chapter 4 shows how that coupling can break down when symmetry no longer requires it. Chapter 5 presents surprising findings of a spin texture hidden in a cuprate superconductor. Chapter 6 presents discussion of future research directions on the study and manipulation of the spin-orbit interaction in materials.

For Larry, Ginny, Shana and Rebecca

Contents

List of Figures

Acknowledgments

I am very grateful to so many people who have helped me realize the dream of becoming a scientist. First, my advisor, Alessandra Lanzara, has provided opportunities to work at the cutting edge and has pushed me to understand the big picture of why our research is important. All of the exciting experiments I have gotten to do are thanks to her vision and insight about where the field is going, her ability to bring together teams for successful collaborations, and her skill in explaining to the broader community the importance of our group's work. Quite a few collaborators have correctly identified her as a "visionary" in our field. Alessandra's guidance through all stages of research and through my development as a scientist in graduate school has been invaluable.

Next, I am so thankful to Chris Jozwiak for taking the time and summoning the patience to teach me everything I know, though not everything he knows, about being an experimentalist in our field. In fact, it is due to his immense skill in instrumentation that the spin-TOF was built and I was able to try all sorts of measurements on a one-of-a-kind tool. His physics explanations are thorough and intuitive and shape my understanding of most of what we do. More importantly, his calm presence was reassuring when I was lost in our experiments or had made big mistakes. I am very grateful to Chris for making the most of all of the teachable moments I provided over the years, and for providing me with very thoughtful advice throughout graduate school. I am very fortunate to have apprenticed under a very skilled, and one of the best-liked scientists at the ALS.

I have been very lucky to have a wonderful teammate in most of the work I've done in graduate school, Chiu-Yun Lin. Work got a lot better when she showed up in our group; some of the most challenging parts of managing the spin-TOF became routine for us as a team. Having essentially lived at the ALS with her during several multi-week experiments, I benefited tremendously from her hard work, experimental savvy, deep physical insight, and perhaps most importantly, cheerful level-headedness when things weren't working at four in the morning. The spin-TOF and the ongoing projects we have been working on are in very good hands with her.

More broadly, the Lanzara group has provided a fun and supportive environment in which to try out difficult experiments. I have been fortunate to parallel Tristan Miller through graduate school. A friendly face in and out of the lab, Tristan has always been very generous with the time he gives to helping me understand elusive concepts. Chris Smallwood's leadership kept the whole group working together well. It was so much easier to keep pushing along in research when I knew I could always talk to him about physics or life as a graduate student. I will forever be grateful for his mentorship, as I am certain many future physicists will be. Wentao Zhang, similarly, instilled confidence in the group with his calm demeanor and constant willingness to help. I am thankful to him for the hundreds of occasions that he came to our aid to help push projects forward.

During my first year of graduate school, I got to share an office with David Siegel and Sebastien Lounis, but the truth is that they began providing valuable advice before I arrived at Berkeley and have remained people I am grateful to be abe to turn to. Greg Affeldt, upon joining our group, took over the role of friendly Michigander, keeping the mood in

the lab light and everyone's spirits up. I am grateful for the many times he helped me talk through difficult physics concepts and more so, the many times we got to talk about things far afield of physics. Drew Latzke is quietly as talented of a basketball player as a physicist, and I have thoroughly enjoyed spending time with him in both roles. Though I never had overlapping projects with them, Irene Lo Vecchio, and Ryo Mori, Cassi Hunt, all contributed meaningfully to my graduate school experience by boosting group camaraderie.

The arrival of some newer students has ensured the success of the Lanzara group for years to come. Jonathan Ma has always been willing to share his electronics skills and help out with anything in the lab at the drop of a hat. Alex Nguyen's excitement for physics research is often like a breath of fresh air. I look forward to seeing the new directions the group is taken towards by Sam Ciocys, Conrad Stansbury, Nick Dale, Prosper Dzanwa, and Kayla Currier, who have enthusiastically thrown themselves into all of the workings of the lab.

Outside of the Lanzara group, Professors Dung-Hai Lee, James Analytis, and Joe Orenstein have provided very valuable insight and feedback on experiments we've done over the years. Collaborators Jonathan Denlinger, Andreas Schmid, and Aaron Bostwick, among many scientists at LBL, have provided countless hours of advice and experimental help. John Pepper and Monroe Thomas have fixed more than a few of my mistakes and made our measurements possible.

I am very grateful to physics mentors I've had throughout my education. In my work in the Lanzara group, I sought to follow the advice of Prof. Chris Stubbs to work on the most important scientific questions that new instruments are just allowing us to study. Prof. Stubbs provided me incredibly enriching opportunities and encouragement in his research group at Harvard. Prof. Melissa Franklin demonstrated what it really means to care about one's students, taking the time to provide very honest advice and helping me define my educational path. My high school physics teacher, Dr. Antonio Nassar, bubbled over with enthusiasm for physics that students couldn't help but join in. I will always be very grateful to him for sparking that passion in me and helping me realize that I can be a scientist.

I owe the greatest thanks to my parents, Larry and Ginny Gotlieb, who began to suggest the enormous possibilities in the world when I was very young by reading to me books about the cosmos. My grandparents, Sam and Sally Gotlieb and Warren and Betty Moorman, encouraged all of their grandchildren by demonstrating a sincere interest in their pursuits. My sisters, Shana and Rebecca, have shown me the best examples of diligent work driven by one's passions. I will be grateful to have those examples throughout my life. Our close family friends Hana and Tibor Zemplenyi made sure I knew from a young age that I should be a scientist. Thank you to all of the people mentioned here, for showing me that I could.

Kenneth Gotlieb

August 3, 2017

Curriculum Vitæ

Kenneth H. Gotlieb

Education

2017 University of California, Berkeley, CA, USA
Ph.D., Applied Science and Technology

2010 Harvard University, Cambridge, MA, USA
A.B., Physics

Honors and Awards

2012 NSF Graduate Research Fellowship

2015 Best Poster, U.C. Berkeley Physics Department poster session

Publications

1. K. Gotlieb, C.-Y. Lin, M. Serbyn, W. Zhang, C. L. Smallwood, C. Jozwiak, H. Eisaki, Z. Hussain, A. Vishwanath, and A. Lanzara. Revealing Hidden Spin Textures in a High Temperature Cuprate Superconductor. Submitted (2017)
2. C.-Y. Lin, K. Gotlieb, M. Serbyn, W. Zhang, C. L. Smallwood, C. Jozwiak, H. Eisaki, Z. Hussain, A. Vishwanath, and A. Lanzara. Universal Spin Texture in a Cuprate Superconductor. In preparation (2017)
3. C.-Y. Lin, K. Gotlieb, Z. Li, C. Jozwiak, S. G. Louie, Z. Hussain, and A. Lanzara. Spin and Orbital Textures in Bi_2Se_3 Quantum Well States. In preparation (2017)
4. K. Gotlieb, Z. Li, C.-Y. Lin, C. Jozwiak, J. H. Ryoo, C.-H. Park, Z. Hussain, S. G. Louie, and A. Lanzara. Symmetry Rules Shaping Spin-Orbital Textures in Surface States. **Phys. Rev. B** 95, 245142 (2017)
5. C. Jozwiak, J. Sobota, K. Gotlieb, A. Kemper, C. Rotundu, R. Birgenau, Z. Hussain, D.-H. Lee, Z.-X. Shen, and A. Lanzara. Spin-Polarized Surface Resonances Accompanying Topological Surface State Formation. **Nat. Comms.** 7, 13143 (2016)
6. K. Gotlieb, Z. Hussain, A. Bostwick, A. Lanzara, and C. Jozwiak. Rapid High-Resolution Spin- and Angle-Resolved Photoemission Spectroscopy with Pulsed Laser Source and Time-of-Flight Spectrometer. **Rev. Sci. Inst.** 84, 093904 (2013)
7. C. Jozwiak, C.-H. Park, K. Gotlieb, C. Hwang, D.-H. Lee, S. G. Louie, J. Denlinger, C. Rotundu, R. Birgenau, Z. Hussain, and A. Lanzara. Photoelectron Spin-Flipping and Texture Manipulation in a Topological Insulator. **Nat. Phys.** 9, 293-298 (2013)

Talks

1. "Laser-based spin- and angle-resolved photoemission spectroscopy for rapid, high-resolution measurements." APS March Meeting, Mar. 2014
2. "Efficient, high-resolution spin-resolved ARPES: instrumentation and studies of hexaborides." Advanced Light Source Users' Meetng, Oct. 2014
3. "Photoelectron spin control in spin-orbit systems." APS March Meeting, Mar. 2015
4. "Symmetry rules and spin-orbital texture in Sb surface state." Quantum Materials Group Seminar, UC Berkeley, Nov. 2016
5. "Symmetry rules and spin-orbital texture in Sb surface state." Forum@MSD, Lawrence Berkeley Lab, Nov. 2016
6. "Spin-polarized surface resonances accompanying topological surface state formation." APS March Meeting, Mar. 2017

Patent

1. C. Jozwiak, C.-H. Park, K. Gotlieb, S. G. Louie, Z. Hussain, and A. Lanzara. Versatile Spin Polarized Electron Source. U.S. Patent 9,142,634. September 22, 2015.

Chapter 1

Spin-Orbit Coupling in Materials

Quantum materials cannot be described by textbook band theory. Their key electronic characteristics come not just from the interaction of electron charge with atomic nuclei, but from electron-electron attraction or repulsion, spin-spin exchange interaction, and coupling of electrons to lattice vibrations, or phonons.

In particular, materials with strong spin-orbit interaction have grown in importance recently as exotic properties have been discovered that lead to new states of matter and opportunities to control magnetism electrically. In these materials, an electron's behavior depends on the orientation of its spin and how that couples to its orbital angular momentum.

This chapter begins with a review of atomic spin-orbit coupling before proceeding to discuss how the interaction can be manifested in a crystal. Subsequently, it presents how broken inversion symmetry can allow for spin-polarized electronic states, especially the key cases of Rashba systems, topological insulators, and crystals with unit cell sectors where inversion is broken locally. Finally, it explains the excitement for using such states in spintronics applications and the new types of materials that emerge when strong spin-orbit coupling is combined with electron correlation.

1.1 Atomic spin-orbit interaction

The spin-orbit interaction in solids derives from the atomic spin-orbit coupling of its constituent atoms, where it is responsible for fine electronic structure. Below, a rough classical argument following Sakurai[1] is presented for how the effect comes about and scales with atomic number.

In the case of an electron moving relativistically around a nucleus with positive charge, the Coulomb attraction of the nucleus appears as an effective magnetic field

$$\vec{B} = -\frac{\vec{v}}{c^2} \times \vec{E} \tag{1.1}$$

where the electron's velocity as it orbits a distance r from the nucleus relates to its orbital angular momentum by

$$\vec{L} = m_e \vec{r} \times \vec{v} \tag{1.2}$$

and the Coulomb field is

$$\vec{E} = -\frac{1}{e} \nabla V_C(r) \tag{1.3}$$

The electron's spin will interact with the effective magnetic field due to the nucleus with perturbative Hamiltonian

$$H_{LS} = -\vec{\mu_s} \cdot \vec{B}. \tag{1.4}$$

Plugging in, this becomes

$$H_{LS} = \frac{1}{2m_e^2 c^2} \frac{1}{r} \frac{dV_C}{dr} (\vec{S} \cdot \vec{L}) \tag{1.5}$$

$$= \frac{a}{2}(j(j+1) - l(l+1-s(s+1)), \tag{1.6}$$

where

$$a = \frac{\hbar^2}{2m_e^2 c^2} \frac{1}{r} \frac{dV_C}{dr}. \tag{1.7}$$

Hence, individual energy levels will be split based on the magnitude and alignment of orbital angular momentum to spin. Those in which $\vec{L}$ is antiparallel to $\vec{S}$, i.e. minimal $\vec{J}$ are favored.

Now, for a hydrogen-like atom, the Coulomb potential is

$$V_C = \frac{Ze^2}{r} \tag{1.8}$$

such that

$$\frac{1}{r} \frac{dV_C}{dr} = \frac{Ze^2}{r^3}. \tag{1.9}$$

From atomic physics, the expectation value for the radius of an electron's orbit in a Coulomb potential about a nucleus of atomic number Z scales as $\langle r \rangle \propto \frac{1}{Z}$. Hence,

$$\Delta E_{SOC} \propto Z^4. \tag{1.10}$$

The overall strength of the spin-orbit splitting rises dramatically with atomic number. It is no coincidence that the materials of interest for properties derived from the spin-orbit interaction tend to have heavy atoms: bismuth is a common constituent. Moreover, the Rashba states on the (111) surface of Au that will be presented in this work are routinely used to characterize photoemission instruments[2,3,4]. These derive from a manifestation of spin-orbit coupling on materials' surfaces. The analogous states on the (111) surface of Cu, two rows directly above Au on the periodic table, were only recently able to be resolved with ultrahigh momentum resolution photoemission[5].

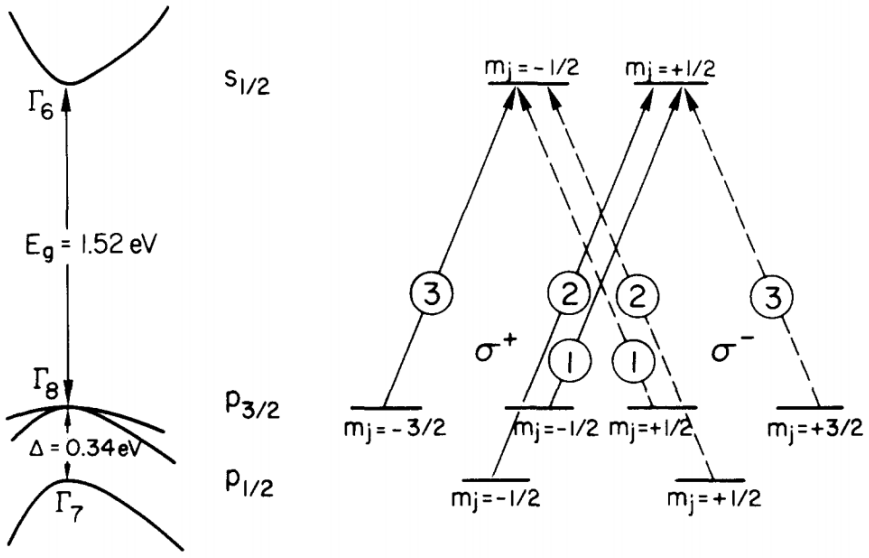

Figure 1.1. **Spin-orbit effects on GaAs band structure and photoemission from Ref.[6].** At left, the band structure of GaAs, with the top $J = \pm 3/2$ valence band and the split-off $J = \pm 1/2$ band 0.34 eV below. The valence band is split away from Γ into heavy holes ($m_j = \pm 3/2$) dispersing slowly and energeticaly higher than light holes ($m_j = \pm 1/2$). At right, photoexcitation probabilities (circled along each possible transition) from the valence to conduction band at Γ with both helicities of circular light. The differences in excitation probabillity are the origin of the spin-polarized electron beams with carefully tuned photon energy.

1.2 Spin-orbit coupling in crystals

The atomic spin-orbit coupling effects that split electron levels based on total angular momentum, J, can extend to crystals, where they can have important impacts on the electronic band structure. In a tight-binding picture, this can be thought of as the electron retaining some of the characteristics of the orbital from which it comes, even as it is now free to hop along atomic sites. In a free electron picture, this can be thought of as the effect on the electron's spin of the electron's motion past ionic nuclei in the crystal. Because it is a relativistic effect, the spin-orbit interaction is a weak perturbation in most materials. However, even where bands remain spin-degenerate, spin-orbit coupling can shape properties of common materials and at more extreme strengths, can give rise to very exotic new types of materials.

The most prominent example of a material with band structure shaped by spin-orbit coupling is GaAs, a widely used semiconductor. The spin-orbit interaction splits the p orbital-dertived valence band into $J = 1/2$ and $J = 3/2$, separated in energy by a so-called "spin-orbit gap"[7]. This is an energy offset between states based on how orbital and spin angular momenta add. The higher energy $J = 3/2$ band sets the band gap to the conduction band, a key quantity of this semiconductor.

However, this upper valence band is itself split into two sub-bands with different effective

mass: heavy holes with $m_j = \pm 3/2$ and light holes with $m_j = \pm 1/2$[8]. In this way, angular momentum affects the effective mass with which holes move through the crystal. It is worth noting that in GaAs, the zincblende crystal lacks an inversion center, and thus actually allows for a spin splitting due to the Dresselhaus effect (discussed below)[9].

In this case, the band splitting due to the spin-orbit interaction enables the generation of spin-polarized photoelectron beams from unpolarized bands through a process summarized in Fig. 1.1. When irradiated with circularly polarized light, electrons must make a transition with $\Delta m_j = +1$ or $\Delta m_j = -1$ depending on the helicity of the light. If the photon energy used only allows for transitions from the top valence band to the s orbital-derived conduction band, then transition probabilities dictate that a majority of photoexcited electrons will have spins pointing into or out of the surface plane. The choice of photon polarization helicity sets which way the photoelectron spins point. If the photon energy is turned up to allow for excitation from the split-off hole band ($J = 1/2$), then the effect is washed away.

1.3 Broken inversion symmetry

So far, we have seen energy splittings based on the total angular momentum, J, of electronic states in a material. Still, the bands are spin degenerate: they are populated with equal numbers of up and down spins along any axis, and the splitting is based on the relative alignment of spin to orbital angular momentum.

When time reversal symmetry is respected (typically meaning there is no magnetic field), electronic states at a momentum k must allow for

$$E(k, \uparrow) = E(-k, \downarrow) \tag{1.11}$$

as the time reversal operation flips both linear and angular momenta. When crystals respect inversion symmetry, it is also true that

$$E(k, \uparrow) = E(-k, \uparrow) \tag{1.12}$$

where inversion flips linear but not angular momentum. If both of these conditions are true, then bands are required to be spin degenerate, i.e.,

$$E(k, \uparrow) = E(k, \downarrow). \tag{1.13}$$

However, in many instances, inversion symmetry is broken and the spin degeneracy may be lifted. Most often, this occurs at surfaces, where a crystal meets the vacuum, or at interfaces between two crystals.

Without the requirement of spin degeneracy, band structure can have a spin texture in momentum space: a correspondence between an electron's momentum and its preferred spin orientation. Typically, electrons of opposite momentum will still have opposite spin. Spin textures are of great interest because they couple a material's magnetic and electrical

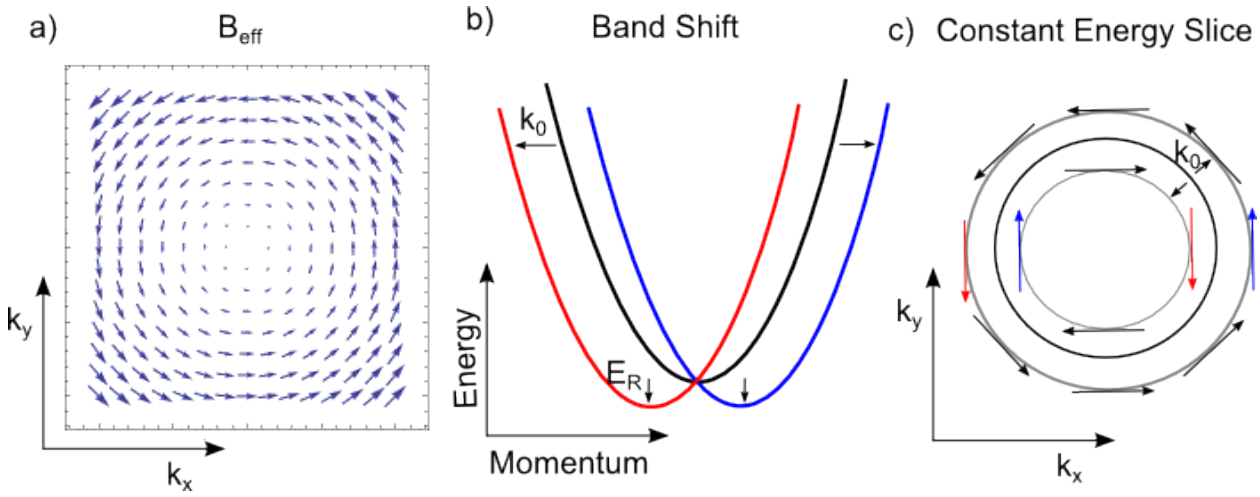

Figure 1.2. **Schematics of Rashba effect. a,** Effective magnetic field as a function of two-dimensional electron momentum, k_y and k_x. **b,** Band dispersions along a momentum cut, showing two parabolic nearly free electron bands each offset in momentum by $\pm k_0$ from the black band that would be present without the Rashba effect. Each band minimum is lowered by an amount E_R from the minimum without the Rashba effect. **c,** The constant energy maps that result. From a single spin-degenerate circular Fermi surface (black, middle) we get two concentric Fermi surfaces with opposite spin helicity (gray, inner and outer circles).

properties; they provide a way to manipulate magnetism electrically. The following sections will present the most common and important types of spin textures found on surfaces.

1.3.1 Rashba Effect

Every crystal loses its inversion symmetry at a boundary with the vacuum or with another material. At these boundaries, the electronic environment is different than in the bulk, and distinct electronic states can form inside bulk energy band gaps. Electrons occupying these surface states are trapped on the surface as there are no bulk states energetically available to move into. In the prominent case of the L-gap in noble metals Cu, Ag, and Au, for example, these electrons populate a two dimensional electron gas on the (111) surface, moving in free electron dispersions on the surface.

Moreover, the electrons will move within an electric field $E_{surf}\hat{z}$ perpendicular to the boundary due to the discontinuity there. There is no in-plane electric field due to the preserved crystal symmetry there. In the relativistic limit, they will experience the electric field as a magnetic field that is in their plane and proportional in magnitude but perpendicular to their momentum

$$B_{eff} = \frac{-1}{c^2}\left(\frac{\hbar\vec{k}}{m^*} \times E_{surf}\hat{z}\right). \tag{1.14}$$

This k-dependent magnetic field is plotted in 1.2a. In the two dimensions of momentum that

surface electrons can move, B_{eff} circles the $\bar{\Gamma}$ point. This field gives electrons in the surface state an effective Hamiltonian $H_R \propto B_{eff} \cdot \sigma$:

$$H_R = \alpha_R(\vec{k} \times \hat{z}) \cdot \sigma = \alpha_R(k_x\sigma_y - k_y\sigma_x) \tag{1.15}$$

where the Rashba constant α_R tidies up the other constants.

In this way, the Rashba effect will split the surface state bands based on spin, lowering and raising the energies of spins parallel and anti-parallel to B_{eff}, respectively,[10]. It leaves the free electron dispersions split in an amount proportional to momentum, i.e.,

$$E(k_{||}) = E_0 + \frac{\hbar^2 k_{||}^2}{2m^*} \pm \alpha_R k_{||} \tag{1.16}$$

where the $\pm$ refers to opposite spins. Figure 1.2b shows what Rashba splitting does: what would have been a single parabolic dispersion is split in half, with the two halves shifted in opposite momentum directions by $\pm k_0$. Each band is lowered to a new energy minimum by an amount E_R.

Figure 1.2c shows the constant energy slices that result from the Rashba effect. What would have been a single spin-degenerate Fermi surface is split into two concentric rings circling the $\bar{\Gamma}$ point, each with electron spin locked perpendicular to momentum and in the plane of the surface due to the effective magnetic field felt. The two rings, though, have opposite spin helicity: clockwise spins (anti-parallel to B_{eff}) are inside of counter-clockwise (parallel to B_{eff}), as the former are raised in energy and the latter lowered.

The magnitude of the Rashba splitting, given by α_R, can relate to the strength of the surface electric field or the intrinsic atomic spin-orbit coupling. For the best known case, the Au(111) surface states that are discussed more in this dissertation, the symmetry breaking at the surface is crucial for the existence of the Rashba effect, but the magnitude can only be accounted for by the strong atomic spin-orbit interaction[11]. The Au(111) surface states may be the prototypical Rashba states[2,12,13], but the effect can occur in many materials[14,15,16,13,17,18,19,20,21,22] and heterostructures[23,24,25].

1.3.2 Dresselhaus Effect

Inversion symmetry is not only broken at material boundaries; many crystals are non-centrosymmetric even in the bulk. The zincblende structure of III-V semiconductors like GaAs does not have an inversion center in its unit cell. This means that spin textures are allowed throughout the material due to the Dresselhaus effect[9].

Specifically, electrons in crystals with bulk inversion *asymmetry* will be subject to a Hamiltonian[26]:

$$H_D \propto k_x(k_y^2 - k_z^2)\sigma_x + k_y(p_z^2 - k_x^2)\sigma_y + k_z(k_x^2 - k_y^2)\sigma_z \tag{1.17}$$

The strength of this spin-orbit interaction is cubic in electron momentum, higher order than Rashba. However, to understand the shape of spin textures that this creates within a plane

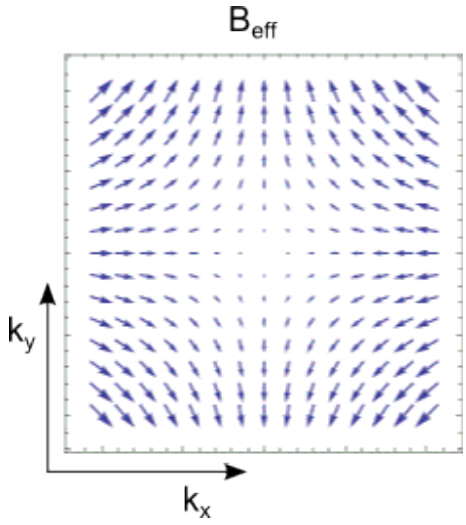

Figure 1.3. **Effective magnetic field in k_x-k_y momentum space on a (001) surface due to Dresselhaus effect.**

of the material, we can integrate over the [001] or k_z direction. This yields a simplified linear form more analogous to the Rashba Hamiltonian:

$$H_D = \beta_D(-k_x\sigma_x + k_y\sigma_y). \tag{1.18}$$

The corresponding effective B field is plotted in Figure 1.3. Unlike the case of Rashba, where B_{eff} circles $\bar{\Gamma}$, here there is a saddle point at $\bar{\Gamma}$. Bands experiencing this form of spin-orbit coupling will be split in energy into spin components that are parallel and anti-parallel to that effective field. The former will be shifted down in energy and have a larger Fermi surface, the latter will be shifted up and have a smaller Fermi surface. This spin texture will be present on, e.g., the GaAs(001) surface.

However, all of the materials studied in this dissertation have bulk inversion symmetry. The spin textures presented are present either due to symmetry breaking at a surface, or to a newly appreciated form of *local* symmetry breaking within parts of a unit cell.

1.3.3 Locally Broken Inversion Symmetry

It has recently become apparent that another form of symmetry breaking can give rise to a spin structure in momentum space that had prevously been hidden from phyisicists. Because spin-orbit coupling is a relativistic effect stemming from the interaction of an electron's spin with the electric fields felt locally, it can cause spin splittings if the sites where the electrons sit are not inversion centers.

As an example, consider a material AB_2 whose unit cell has layers A-B-A, with charge carriers primarily moving in the A layers. Each A layer is locally asymmetric: there are different ions above and below: an A layer on one side and a B layer on the other. This

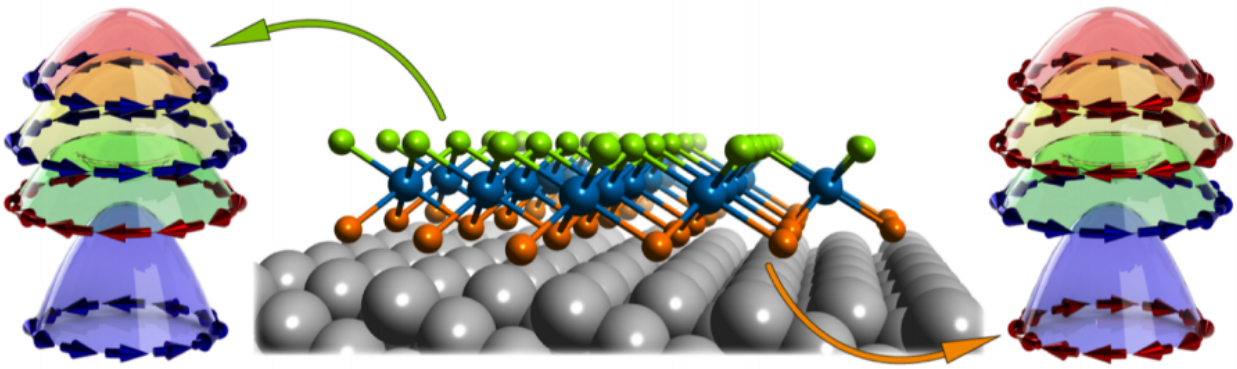

Figure 1.4. **Spin textures of $PtSe_2$ from Ref.[28].** Cartoon of monolayer $PtSe_2$ on Pt(111) with green and orange indicating the two Se layers that are carried into each other by inversion. Each of these layers has a corresponding spin texture for bands near the Fermi level, but these two sets of spin textures are opposite to each other.

creates an electric field through each layer. Similar to what can happen at material surfaces, this electric field can give rise to a Rashba-like effect, creating a spin-momentum locking within the layer. However, the top and bottom A layers of a given unit cell are the inverse of each other: if one has an electric field pointing up, the other will have an electric field pointing down. Hence, they will have Rashba textures of opposite chirality, effectively canceling each other out.

In total, the unit cell will have no net spin polarization; its band are fully spin degenerate. However, this fact belies the spin structure that does exist within the unit cell. Wave function components with opposite spin are spatially separated, a form of spin order that does not exist in normal spin degenerate bands, in which spins are randomly oriented and the spin degree of freedom does not affect the electron's behavior at all. Even if there is no dipole electric field, if the sites where electrons sit are not inversion centers, then an analogous form of the Dresselhaus effect is allowed, in which one spin texture is balanced by the opposite in another part of the unit cell[27].

This form of spin ordering in k space is somewhat analogous to antiferromagnetic ordering in real space. In contrast to non-magnetic materials, in which spins point randomly and average to zero magnetic moment, in antiferromagnetic materials, spins are aligned in a very specific way so as to cancel each other out and make the magnetization vanish.

This new type of spin texture had eluded physicists until now because it does not readily reveal itself in most experiments. Each spin is counter-balanced by another within the same unit cell, so transport experiments, for example, would not see any spin currents develop with an electrical current. However, a probe that couples to one spatial part of the wave function more than the other will be sensitive to such an ordering. Spin-resolved ARPES is such a probe, thanks to its surface sensitivity, discussed in the next chapter.

In this way, these "hidden" spin textures have been found in WSe_2[29] and $PtSe_2$[28], which provide nice examples of the phenomenon. A cartoon of the latter is shown in Figure 1.4. There, a single layer of $PtSe_2$ is grown on a Pt(111) substrate. Top and bottom Se layers

are shown in green and orange, respectively, on either side of the blue Pt layer. The two Se layers are inversion partners with opposite dipole fields in each. As was revealed by spin-ARPES[28], the bands near the Fermi level all have helical spin textures, but those spins circle in opposite directions for the wave function component within the green Se layer and the orange Se layer.

Whereas magnetism creates spin ordering in real space, the Rashba and Dresselhaus effects create spin ordering in momentum space. This new form of hidden order exists in both real and momentum space. Probing in just real or momentum space will reveal a balance of spins, but looking preferentially at one spatial component of the wave function and mapping its spins in momentum space will show that the spins do order themselves thanks to spin-orbit coupling.

1.4 Consequences of spin-orbit coupling in materials

We have seen how spin-orbit coupling comes about in atoms. Then we saw the various ways it can be manifest in crystals, depending on the crystal symmetry. Now, we look at some of the important consequences of its presence in materials. These include novel and useful transport phenomena and new states of matter. When spin-orbit coupling is combined with other strong electronic interactions, still more new types of exotic materials are possible.

1.4.1 Spin Hall Effect and Quantum Spin Hall Effect

The spin-orbit interaction is behind a novel transport phenomenon of potential great utility[30,31,32]. The Spin Hall Effect causes up and down spins to accumulate at opposite ends of a sample perpendicular to the direction of electrical current, much as the Hall effect causes positive and negative charge to accumulate on opposite surfaces. In this case, no magnetic field is needed to cause the phenomenon to occur: spin-orbit is enough.

As charge carriers move with electrical current, they may scatter laterally. In this process, the momentum that they pick up perpendicular to the direction of current flow gives them some effective angular momentum about atomic nuclei. Scattering to the left means circling the nuclei in one direction, while scattering right means circling the nuclei the other way. That effective orbital angular momentum can be coupled to spin, setting up a preference to scatter to the left or to the right depending on the carrier's spin in order to minimize $L \cdot S$. Whereas the applied magnetic field in a Hall effect measurement causes positive and negative charge to curve their paths in opposite directions, in the spin Hall effect, intrinsic atomic spin-orbit coupling causes up- and down- spins to curve their paths in opposite directions.

In this way, up spins will tend to accumulate at one boundary, down spins at the opposite boundary. In analogy to a Hall voltage, one could say that a "spin voltage" develops perpendicular to the direction of applied electrical voltage. Figure 1.5c demonstrates this

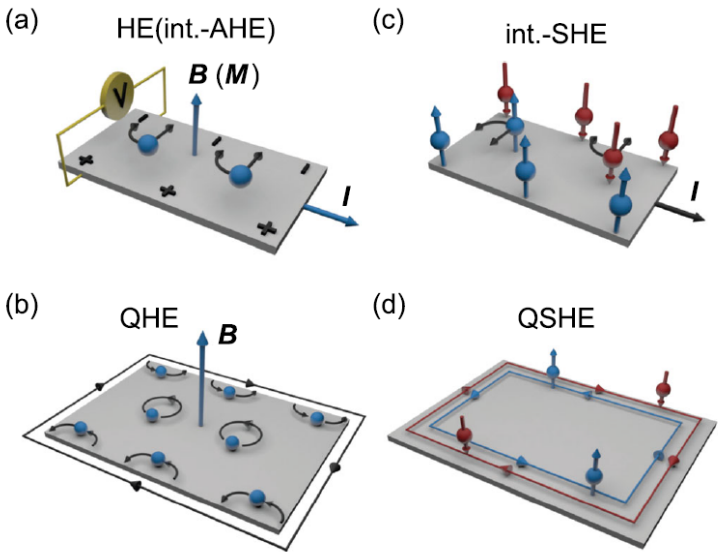

Figure 1.5. **Hall and Spin Hall Effects from Ref.[32]. a,** In the Hall Effect, charge accumulates on surfaces perpendicular to the direction of current when a transverse magnetic field is applied. **c,** In the Spin Hall Effect, spin accumulates on opposite surfaces perpendicular to the direction of current flow without the need for an electric field. **b,d,** Similar to the above phenomena, the Quantum Hall Effect and Quantum Spin Hall Effect have discrete edge transport channels.

concept in the context of the various Hall effects. The spin Hall effect was first realized experimentally in none other than GaAs, whose spin-orbit-induced properties were discussed previously[33].

However, the related quantum spin Hall effect, instances of which are discussed in the next section, might prove to be the most scientifically and technologically revolutionary. To understand it, begin with the quantum Hall effect, the limit of the Hall effect when an electron gas is quantum confined to a two-dimensional plane. In that case, Landau levels create gaps in the electronic spectrum, making the material an insulator. The magnetic field also causes cyclotron orbits to have a certain handedness. At the edges of the material, electrons cannot backscatter into cyclotron orbits of the opposite handedness. Thus, they must continuously hop forward, bouncing along the edges in half orbits of the one handedness. In this way, there is a single conduction channel running along all of the edges of the material, and charge carriers traveling in opposite directions are spatially separated on opposite sides of the sample. Transport along the edge is ballistic as backscattering is disallowed.

A quantum spin Hall material, would then, analogously constrain all transport to the edges of a two dimensional material and it would spatially separate charge carriers *with the same spin* to opposite edges. A single ballistic transport channel would circle the sample edges in one direction for spin-up, a second channel would circle in the opposite direction for spin-down. This situation is shown in Figure 1.5d. As long as time reversal symmetry is respected (no magnetic field is applied), then there is no mechanism to flip spin, and thus

no way for a charge carrier to backscatter into the channel moving in the opposite direction along the same edge of the material.

Learning from the spin Hall effect, we see that spin-orbit coupling can link the direction a charge carrier is moving to the orientation of its spin and which edge it accumulates on. Thus, we expect that dissipationless spin currents can be achieved in a two dimensional material if it has sufficiently strong spin-orbit coupling as well as a mechanism to force all conduction to happen at the sample edges. Such a quantum spin Hall state was achieved in HgTe quantum wells sandwiched between thick CdTe layers[34]. The HgTe provides strong spin-orbit coupling, and the edge conduction comes about due to the different topology of bands in HgTe versus CdTe, a revolutionary new way of characterizing materials explained in the next section.

1.4.2 Topological Insulators

Spin-orbit coupling is responsible for a fundametally new type of material: topological insulators that are bulk insulators, but have metallic surfaces[35,31,36]. These metallic surface states are said to be topologically protected: the nature of the bulk band structure requires them to be there even if disorder is introduced on the surface. However, it is not just because of their electrical behavior that topological insulators have generated excitement. More important is the fact that they are new states of matter that had been hiding in plain sight: the commonly studied Bi_2Se_3 and Bi_2Te_3 have been used widely in thermoelectrics applications without condensed matter theorists considering the deep implications of their band structure.

Most states of matter are distinguished from each other by different symmetries: liquids have continuous translational symmetry while crystalline solids have only discrete translations throiugh which they return to themselves. These new states of matter are distinguished instead by topology, invariant quantum numbers that characterize a material and categorize them into the trivial (ν_0=0) and nontrivial (ν_0=1). To borrow an overused analogy, a doughnut can be smoothly transformed into a coffee mug in the sense that both have a single hole punched through them, but it cannot be smoothly transferred into an orange that is entirely without holes. In the same sense, materials of different topology cannot be continuously adjusted from one to the other; they are stuck with the topological invariant ν_0 and trivial or nontrivial nature that they've got.

So how does one smoothly transform a material, and what would change a material's topology? Adjusting the Hamiltonian that describes an electronic state can continuously alter the shape of the band structure and the associated electrical properties. However, to fully close the electronic band gap is to fundamentally alter the material, and to tune the Hamiltonian past that point is to create a different material. A material becomes topologically non-trivial when interactions within the crystal cause energy levels of valence and conduction band states to be inverted relative to what they would be in the atomic limit. Most often, this is due to strong spin-orbit coupling, but even the crystal field can cause this. The concept of this band inversion is shown in Figure 1.6.

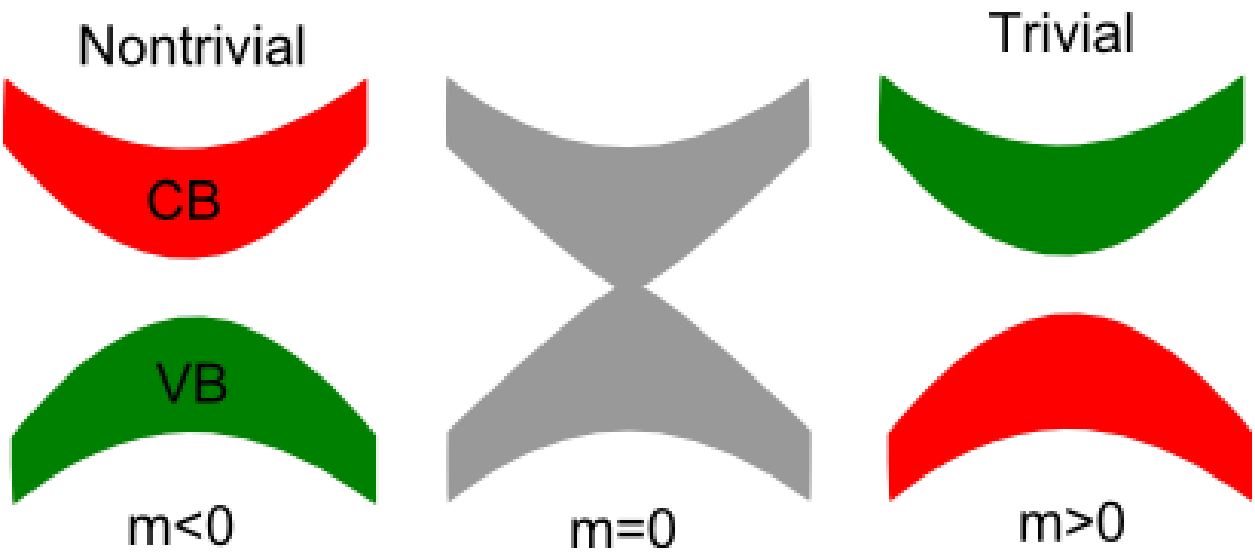

Figure 1.6. **Band inversion in a topological insulator.** The electronic states that contribute to the valence band and conduction band are opposite in the case of trivial and nontrivial insulators: the two cases can be thought of as having opposite signs of effective mass. Between the two, the two bands must cross each other with a massless dispersion.

Consider a standard "trivial" insulator, in which the electronic states that constitute the valence band are marked in orange, and those that constitute the conduction band are marked in green. Now turn on an interaction that treats the orange and green states differently: the two bands will move in energy relative to each other. Turn up the interaction enough, and they may change energy ordering such that the states that made up the valence band now populate the conduction band, and vice versa. Essentially, the electron's effective mass m^* has changed sign. The band gap between these valence and conduction bands is inverted relative to what it had been before. At the point between these two types of insulators when m^*=0, the bands had to cross each other and close the gap, creating a metal of massless fermions. This moment of discontinuity represents an unsmooth change of the Hamiltonian The inverted band gap indicates that the material is "nontrivial;" its topological invariant is ν_0=1 and is distinct from the trivial insulator with ν_0=0 in an important way.

At the interface between a trivial and nontrivial insulator, the electronic wave functions must continuously transform themselves: the valence and conduction bands must undo their energy inversion. Thus, they must cross each other, closing the band gap at the surface, creating a metallic surface state with a linear Dirac dispersion. Given that the vacuum is the simplest insulator, the surface of any topological insulator hosts these metallic states. They are the three dimensional analog of the two dimensional quantum spin Hall insulator with edge channels for ballistic spin-polarized transport. Note that these surface properties are required by the nature of the *bulk* band structure. In this way, they are totally robust: no amount of dirtying the surface can cause them to disappear.

What are the signatures of topology in a material's band structure? How does an inverted gap appear differently than an uninverted gap? At time reversal invariant momenta (TR

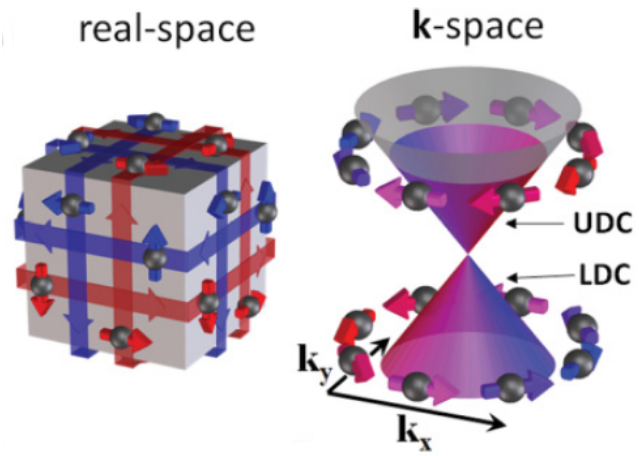

Figure 1.7. **Real and k space depictions of topological surface state from Ref.[37].** In real space, electrons move on the surface of a material with spin locked perpendicular to their direction of motion. In momentum space, they are arranged in a cone with a helical spin texture circling the $\bar{\Gamma}$ point.

points) in a material's Brillouin zone, all bands must be spin degenerate. Between these points in k space, surface states may be spin-split, as seen, for example, in the case of the Rashba effect. In the case of a trivial insulator, the two spin split bands remain partnered to each other, meaning that they would be degenerate in the absence of spin-orbit coupling. These two partnered bands will cross the Fermi level or merge into the bulk continuum together.

However, in a nontrivial material, meaning one that has an inversion at one of the TR points, an odd number of surface bands will span the band gap and connect the conduction to the valence band (where a spin-degenerate band counts doubly). Thus, a single spin polarized cone may encircle one of these TR points, with its only spin degeneracy coming in a Dirac point at the TR momentum. Alternatively, there could be multiple surface bands present, with degeneracies at multiple TR points. In this case, the bands must switch partners between TR points in k space: within a pair of spin-split bands, one will separate off to join the bulk bands while the other may find a new partner surface band emerging out of the bulk continuum.

Either way, the material's topology is encoded in its Fermi surface. In a trivial material, the TR points are circled in total by an even number of (spin-polarized) bands. In a nontrivial material, there is an odd number of Fermi surface rings around TR points.

This relates to the Berry's phase that is a signature of topology. The wave function of spin-$\frac{1}{2}$ particles picks up a negative sign or phase of π upon traveling a closed loop, such as a Fermi surface ring around a TR point. That loop must be traversed twice to return the wave function to itself. Nontrivial materials, with their odd number of enclosures of TR points, thus have a Berry's phase of π, whereas trivial materials have a Berry's phase of 0 or equivalently, 2π. The Berry's phase is an invariant (essentially $\pi\nu_0$) characterizing the topology of a material, and it can be measured with spin-resolved ARPES by the number of spin-polarized Fermi surface rings around TR points.

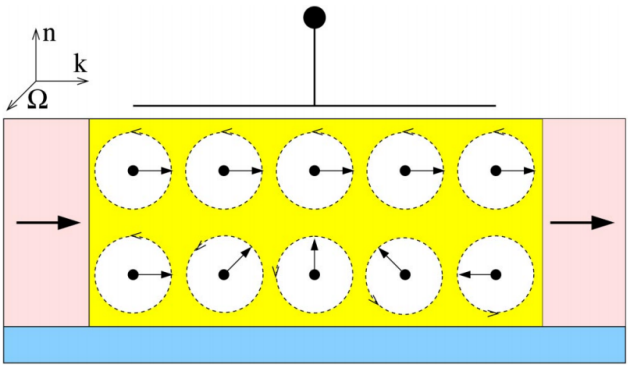

Figure 1.8. **Conceptual drawing of Datta-Das Spin FET from Ref.[26].** A magnetized ferromagnet acts as source and drain (pink). In between, a very thin channel is controlled by a gate voltage.

So what does a typical surface state look like? Figure 1.7 shows a cartoon of the topological surface states of Bi_2Se_3 in both real and k space. The $\bar{\Gamma}$ point, a TR point, is encircled by a single Dirac cone with helical spin texture. This property is referred to as spin-momentum locking: the direction an electron travels in determines which way its spin must point. The upper and lower halves of the cone have opposite helicity such that a given slice through the cone would yield two branches of opposite spin that each connect the valence band below the cone to the conduction band above the cone. The spin orientation associated with each (k,E) point on the Dirac cone is matched by the opposite spin at ($-k$,E), as required by time reversal symmetry. Only by breaking this symmetry (e.g., by applying a magnetic field), is backscattering allowed and the surface able to be gapped out.

In real space, this shows up as two dimensional metals on each surface with spins locked perpendicular to the direction of propagation. Opposite surfaces have opposite spins for the same momentum direction: reversed chirality in k space. In this way, two opposite surfaces together form one complete spin-degenerate metal. In this manifestation of the quantum spin Hall effect on the two-dimensional surface of a three-dimensional crystal, any currents are dissipationless. In order for a carrier to backscatter (switch direction of momentum), its spin would also need to flip, which would require a magnetic field. There is considerable excitement for using these spin-polarized dissipationless currents in electronics.

1.4.3 Spintronics

Spin-orbit materials have generated excitement for the opportunity to manipulate spin electrically. A spin texture in momentum space is a preference for electrons traveling in a certain direction to have spins point a certain way. In passing current, an excess of electrons traveling in a given direction or with a certain direction of k, one also creates an excess of spins. Thus, a material like a topological insulator provides a mechanism to magnetize materials by applying a voltage.

This has led to ideas for using spin-orbit materials in "spintronics:" new forms of elec-

tronic devices that perform computation based on electron spin.[38] In such a device, bits would be written and read as 0 or 1 based on the direction a spin pointed rather than on voltage, which is the presence or absence of charge. This could carry advantages of faster computation with lower energy consumption. Spin could either add to the complexity of information stored in traditional bits or allow it to be nonvolatile. Thus, there is ongoing research to develop spintronic devices, such as a spin field effect transistor, a spin-based analog to normal transistors.[39,40,41]

Consider, for example, the proposed Datta-Das spin-FET shown in Figure 1.8[26]. A magnetized ferromagnetic material, shown in pink, acts as both source and drain, injecting a spin-polarized current into the yellow channel. The channel is very thin, effectively a two-dimensional electron gas subject to an electric field controlled by the top gate. This is precisely the arrangement of a Rashba system, with α_R again controlled by the gate. Spins traveling to the right ballistically will feel an effective magnetic field pointing out of the page, causing them to precess counter-clockwise. Their phase upon arrival at the drain determines whether they are transmitted. If spins arrive at the drain well aligned to its direction of magnetization (top row), then current will pass well; if they do not, the interface will act as a barrier, transmitting little current (bottom row). In this way, the spin-orbit coupling is tuned by a gate voltage and allows that voltage to open and close a channel based on the effect that it has on a spin current.

Still, engineering such devices will require deeper understanding of spin-orbit materials, their dynamics, and the properties that emerge at their surfaces and boundaries with other materials. Both generation of spin polarized currents and reading of spins can be done purely in solid state or by the interaction of circularly polarized light with a material. Thus, there is a need for ongoing research into how spin polarized currents are transmitted between ferromagnets and spin-orbit coupled semiconductors and other spin-dependent properties of interfaces. Moreover, there is a need to understand how light can generate spins, and how intrinsic spin textures control a material's interaction with light.

Lastly, spintronics devices will need long-lived spin states, but spin-orbit coupling renders spin not a good quantum number. A precisely prepared spin state will not remain in that spin state. There is a need to study spin-orbit materials in the time domain to understand the parameters that control the depolarization times of a material: how can we engineer systems to progress out of a pure spin state as slowly as possible. In all of these ways, spin-orbit coupling presents opportunities for radically new devices as well as materials research challenges before those devices can be built.

1.4.4 Spin-orbit coupling with electron correlation

Spin-orbit coupling can take on added importance when it is combined with other strong interactions in a crystal. In particular, electron-electron correlation is the other key ingredient that gives rise to exotic materials outside of classic band theory. One can plot a phase diagram, as in Figure 1.9 from Ref.[42], of quantum materials as a function of spin-orbit

coupling strength (λ/t where t is the hopping term) versus electron correlation strength (U/t).

In the bottom left corner are all of the materials traditionally studied in solid state physics: normal metals, semiconductors, and band insulators. Moving along the x axis by turning up the strength of spin-orbit, one creates new topological states of matter that were described previously. In this case, spin-orbit is not a weak perturbation, but rather defines important new physics.

However, this dissertation will also present work on materials from the top left of the phase diagram. In that regime, strong onsite electron-electron repulsion U, causes electrons to strongly prefer to be on different atomic sites. Near half-filling, electrons become very localized on particular sites and do not hop to their neighbors much: the strong interaction among electrons causes the material to be a Mott insulator. These materials are, for example, the parent compounds of the cuprate superconductors.

Still, one might ask what effect any finite spin-orbit coupling has on materials in this regime. In the presence of superconductivity, it is likely to change the symmetry of Cooper pairs[43,44] as they cannot be in a pure singlet or triplet state if spin is not a good quantum number. To be sure, it would also dramatically alter any spin fluctuation model for unconventional superconductivity[45]. Chapter 5 will show that a cuprate superconductor, the most studied correlated material, has important properties derived from spin-orbit coupling.

Spin-orbit coupling provides opportunities to create heterostructures with novel superconducting properties such as bilayer Rashba systems[46] or topological insulator/ferromagnet interfaces with a new Amperean pairing mechanism where attraction is mediated by spin fluctuations[47]. The interaction between materials at the two corners of the phase diagram can create surprising results: thin films of topological insulator Bi_2Se_3 become superconducting when layered on high temperature superconductor $Bi_2Sr_2CaCu_2O_{8+\delta}$ due to proximity effects, though the superconductivity has a different symmetry than that of the cuprate[48]. Intriguingly, the interface between the two materials is also likely to host mysterious Majorana fermions, particles that are their own antiparticles and might be used in quantum computers[49,50,51].

New properies start to emerge in materials where both spin-orbit coupling and electron correlation have meaningful strength, the top right quadrant of the phase diagram. This occurs especially in $5d$ materials whose d orbitals are still fairly localized, but whose heavy nuclei cause strong coupling between spin and orbital degrees of freedom. Rather than fight each other, spin-orbit coupling and Coulomb repulsion can conspire together to create an insulating state where there might not have otherwise been one.

When spin-orbit coupling is still the stronger of the two effects, the physics can still be defined by band topology, and new states of matter like axion insulators and Weyl semimetals emerge. The former are similar to topological insulators, but magnetic ordering due to electron correlation spontaneously breaks time reversal symmetry and causes a strictly quantized electrical polarization to develop due to applied magnetic fields. The latter are similar in that U breaks time reversal symmetry, creating a *bulk* band structure reminiscent of the topological surface states with massless Dirac fermions. Meanwhile, the surfaces of

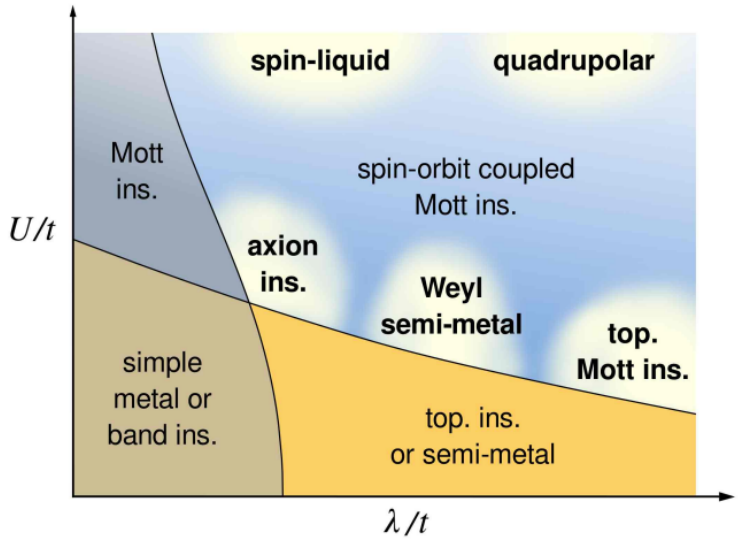

Figure 1.9. **Phase diagram of spin-orbit coupling and electron correlation from Ref.[42].**

Weyl semimetals have strange Fermi arcs that only complete a full Fermi surface when adding the arcs on two opposite sides of the sample.

As electron-electron interactions are turned up even more, electrons become more localized and band topology is no longer relevant, but new phases such as spin liquids emerge that can only exist with large U and λ. The iridates have recently generated considerable excitement as analogs of the cuprate superconductors with a key difference: strong spin-orbit defines their electronic properties[52,53], becoming Mott insulators thanks to the assistance of spin-orbit coupling. In honeycomb iridates like Na_2IrO_3, as in GaAs, spin-orbit coupling splits the band nearest the Fermi level into $J = 1/2$ and $J = 3/2$ bands, lifting orbital degeneracy. With the states that would be at the Fermi level having only $J = 1/2$ character, the band is half-filled. Electron-electron correlation is then able to split it, leaving behind a Mott gap at the Fermi level. The strength of the spin-orbit interaction actually enables the parent compound to become an antiferromagnetic Mott insulator.

As has been described, the interactions that give materials novel quantum properties: electron-electron correlation and spin-orbit coupling, define a two-dimensional phase space in which to see what new states of matter are possible. Within this playground, condensed matter physicists can tune materials properties and even create new types of particles. This dissertation will jump around that phase diagram. Using an innovative tool that can bring unique insight about the effects of spin-orbit coupling in a material, it will show how the interaction shapes physics in the strong spin-orbit limit, and how the presence of non-negligible spin-orbit can alter properties in the strong correlation limit.

Chapter 2

Laser-Based Spin- and Angle-Resolved Photoemission Spectroscopy

This chapter explains the instrumentation and techniques used in the experiments presented in this dissertation. To begin with, it covers the technique of angle-resolved photoemission spectroscopy (ARPES) as it has been commonly used to study materials' band structure.

Next, it explains the challenges of adding spin resolution to an ARPES instrument and how the spin-resolved spectrometer developed by Chris Jozwiak within the Lanzara group improves the situation meaningfully. This chapter will then describe progress in extending the capabilities of the instrument: coupling it with a laboratory-based laser to achieve very high-resolution, rapid measuremnts, and then subsequently using that laser in a pump-probe setup to study spin-dependent dynamics.

2.1 Angle-Resolved Photoemission as a tool for studying electronic interactions

Angle-resolved photoemission spectroscopy has provided key insights about wide-ranging materials. While the drive to study cuprate superconductors was perhaps the biggest motivation for improvement of photoemission instrumentation over the last three decades[54,55,56,57,58],

ARPES now regularly allows for breakthroughs in topological materials[59,60,61,62,63], low-dimensional materials[64,65,29], and materials with exotic properties owing to the strength of one or several electronic interactions[42,66,44,67,68].

Beyond visualizing materials' band structure, ARPES provides a window into various types of electronic interactions, including spin-orbit coupling[13,59,69,44], electron-electron correlation[55,70], and electron-phonon coupling[71]. The delocalized electrons that occupy a material's band structure have their properties modified by many-body effects in their surrounding environment. For example, dragging around a cloud of phonons or scattering off of other electrons will alter an electron's energy and cause it to remain in a state for only a finite time. We can treat individual carriers as quasiparticles whose spectral function $A(k, \omega)$ encodes all of the modifications to the bare band structure due to this mess of interactions. Indeed, careful analysis of this single particle spectral function that is directly measured by ARPES (and discussed below) allows for quantitative analysis of quasiparticle self-energies and lifetimes as well as the energies of bosons that couple to quasiparticles[72]. Below, we explain how the photoemission process plays out and encapsulates these microscopic details of the electronic environment in the material, following Ref.[55].

2.1.1 Three Step Model of Photoemission

The ARPES technique relies on the photoelectric effect[73], in which a single photon with energy above a material's work function causes an electron to be ejected from a material. The process is a quantum mechanical transition from an initial to a final state of an N electron system that has probability given by Fermi's Golden Rule:

$$w_{fi} = \frac{2\pi}{\hbar}|\langle\psi_f^N|H_{int}|\psi_i^N\rangle|^2\delta(E_f^N - E_i^N - h\nu), \tag{2.1}$$

where the δ function enforces energy conservation (more on that later). In this case, the interaction Hamiltonian is that of a photon with an electron in the system:

$$H_{int} = -\frac{e}{mc}\vec{A}\cdot\vec{p} \tag{2.2}$$

with $\vec{A}$ the electromagnetic vector potential and $\vec{p}$ the electron momentum operator.

To understand how this interaction plays out, we can break the photoemission process into three distinct steps: 1. an electron is photoexcited to a higher energy state, 2. that electron travels through the sample to the surface, and 3. photoelectrons with sufficient energy overcome the material's work function and escape into the vacuum. Step 1 merits careful analysis as it encodes all of the information on the electron initial state and interaction with the light. Step 2 gives ARPES its surface sensitivity as electrons have a finite mean free path before scattering in a crystal. For $h\nu = E_{kin} = 6$ eV, this is 1-10 nm, but for synchrotron energies of ≈30-100 eV, it is less than 1 nm. Thus, ARPES is only able to probe very near-surface layers. Lastly, step 3 forces a careful analysis of photoelectron momentum in the direction perpendicular to the surface, discussed later. As sample surfaces

accumulate adsorbed gas molecules over the course of an experiment, photoemission intensity will diminish as photoexcited electrons are scattered at the surface.

Returning to Step 1 and the key question of which electrons are photoexcited, we are aided by an important assumption: the sudden approximation. If the photoexcitation happens quickly enough, then the relaxation of the many-body system due to the loss of one of its electrons will not have a chance to affect the outgoing electron; the photoelectron can be thought of as reflecting the initial many-body state before arrival of the photon. Thus, the N electron system can be written as

$$\psi_f^N = \mathcal{A}\phi_f^k \psi_m^{N-1} \tag{2.3}$$

where ϕ_f^k is the wave function of a single photoelectron with momentum k, ψ_m^{N-1} is the excited state m of the N-1 electron system left behind, and the antisymmetrization operator $\mathcal{A}$ ensures that the Pauli exclusion principle is met. A similar factorization of the initial state wave function leaves the matrix element in 2.1 as

$$\langle \psi_f^N | H_{int} | \psi_i^N \rangle = \langle \phi_f^k | H_{int} | \phi_i^k \rangle \langle \psi_m^{N-1} | \psi_i^{N-1} \rangle. \tag{2.4}$$

The first matrix element, which we label $M_{f,i}^k$ is for excitation of a single electron, while the second, $c_{m,i}$ is the overlap between the initial state ψ_i^{N-1} and final state ψ_m^{N-1}. If this were a system of non-interacting particles, then $c_{m,i}$ would be 1 for a particular final state and 0 for all others: the removal of the Nth electron would not affect the other N-1 electrons, whose final state would exactly match their initial ground state. However, given electron-electron interaction, the removal of the Nth electron will alter the state of the other N-1 electrons, which now have finite overlap with multiple excited states m.

These electron interactions have strong implications for the photoemission spectra measured. The intensity of electrons excited in step 1 by a photon $h\nu$ to an energy E_{kin} and momentum k will be

$$I(k, E_{kin}) \propto \sum_{f,i} |M_{f,i}^k|^2 \sum_m |c_{m,i}|^2 \delta(E_{kin} + E_m^{N-1} - E_i^N - h\nu). \tag{2.5}$$

Intensity will be contributed from a range of excited multi-particle states m, yielding an ARPES spectrum that is broadened in a way that reflects the range of excitations that are left behind by the photoelectron. We now present a way to interpret these spectra to understand the microscopic environment inside the crystal.

2.1.2 Single Particle Spectral Function

To understand how an electron behaves in an interacting many-body system, we can imagine adding one to a state with momentum k. Then the probabilty of it remaining in that state at a time t will be given by a Green's function $\mathcal{G}(t - t')$. A Fourier transform would yield a Green's function in energy and momentum $G(k, \omega)$ and allow us to define a

spectral function for removal of a single particle

$$A(k,\omega) = \frac{-1}{\pi} ImG(k,\omega) = \sum_m |\langle \psi_m^{N-1}|c_k|\psi_i^N\rangle|^2 \delta(\hbar\omega - E_m^{N-1} + E_i^N) \tag{2.6}$$

where c_k annihilates an electron with momentum k.

Defining things this way allows us to recast the photoemission intensity of 2.5 as

$$I(k,\omega) \propto |M_{f,i}^k|^2 f(\omega) A(k,\omega) \tag{2.7}$$

where the Fermi distribtuion $f(\omega)$ results from the fact that electrons can only be photoemitted from states that are populated. This organization highlights the fact that there is an underlying spectrum for quasiparticles $A(k,\omega)$ that will be thermally occupied according to $f(\omega)$ and from that occupation, you can have photoemission probability $|M_{f,i}^k|^2$. After accounting for the latter two functions, the single particle spectral function is fundamentally what is measured by ARPES.

How does this object encapsulate both the band structure and renormalization due to many-body interactions? If we define an electron's self-energy $\Sigma(k,\omega) = \Sigma'(k,\omega) + i\Sigma''(k,\omega)$, then the Green's function and spectral function are given by

$$G(k,\omega) = \frac{1}{\hbar\omega - \epsilon_k - \Sigma(k,\omega)} \tag{2.8}$$

$$A(k,\omega) = \frac{-1}{\pi} \frac{\Sigma''(k,\omega)}{[\hbar\omega - \epsilon_k - \Sigma'(k,\omega)]^2 + [\Sigma''(k,\omega)]^2} \tag{2.9}$$

where ϵ_k is the unrenormalized band energy at momentum k before consideration of many-body interactions. The real self-energy $\Sigma'(k,\omega)$ shifts the spectrum in energy; it accounts for the change in an electron's energy because it is constantly interacting with other particles. The imaginary self-energy $\Sigma''(k,\omega)$ broadens the spectrum and is inversely proportional to the lifetime of a particle in a state with k and ω before it is scattered to another state. The self-energy corrections due to electron-electron interactions and various electron-boson interactions will each have their own characteristic dependence on ω that allow for analysis of the strength of various interactions inside of a material[72].

Having established a formalism for the object that photoemission measures, we now proceed to how the experiment actually works.

2.1.3 Energy and momentum analysis

Through the photoemisson process, conservation of energy allows an experimenter to relate the binding energy of an electron inside of a material to the kinetic energy of the resultant photoelectron. Specifically,

$$E_B = h\nu - \Phi - E_{kin}, \tag{2.10}$$

where Φ is the material's work function and hν is the photon energy used to probe it[55].

Next, conservation of momentum in the plane of the material's surface means that the angle that a photoelectron leaves a sample is a direct function of its crystal momentum inside of the sample as well as its kinetic energy after photoemission. With the latter independently measured, the former can be calculated by

$$\hbar k_{||} = \sqrt{2mE_{kin}} sin\theta \tag{2.11}$$

where θ is the angle a photoelectron is emitted from the sample normal[55]. The sample's polar and tilt angles can be rotated to adjust the photoelectron emission angle being measued by a fixed detector.

Lastly, a quasiparticle's crystal momentum perpendicular to a sample surface is uniquely fixed by the combination of kinetic energy and momentum via:

$$\hbar k_{\perp} = \sqrt{2m(E_{kin} cos^2\theta + V_0)} \tag{2.12}$$

where V_0 is an "inner potential" related to the loss of energy and momentum in overcoming the material's work function at the sample surface[74]. Thus, any single ARPES measurement is of electrons at a single $k_{\perp}$. In practice, the inner potential is measured experimentally by scanning a range of photon energies until band structure is repeated in $k_{\perp}$ and the size of the reciprocal lattice in the z direction is used to extract V_0. In this way, photon energy scans are used to track band dispersion in $k_{\perp}$, and a lack of dispersion is taken as evidence of the two-dimensional nature of a material.

Standard ARPES measurements are conducted with commercially available hemispherical energy analyzers, which acquire a two-dimensional energy-momentum map all at once. Photoelectrons travel through the vacuum between two concentric hemispheres held at a potential difference, creating radial electric fields. As the photoelectrons bend around the hemisphere, the curvature of their path, and thus where along the plane of their motion they strike an imaging detector at the far side, is set by their kinetic energy. Where they hit along the perpendicular axis of the detector is determined by the angle they left the sample.

2.1.4 Role of photoemission process

Interpreting ARPES maps means accounting for the quantum mechanical transition that takes an electron from its initial state inside of a material to a final state as a free electron in the vacuum. The quantum mechanical matrix elements that determine the probability of such a transition occurring, $M^k_{f,i}$ discussed previously, can depend on the geometry of the photoemission experiment and components of the electron's wave function. Thus, ARPES measurements made with varying photon energies, photon polarizations, or angles of incidence of light may be sensitive to different atomic orbitals and yield different results[75,76].

To understand how photon polarization can affect photoemission intensity, consider the experimental geometry of Fig. 2.2, where the Cu $d_{x^2-y^2}$ orbitals are probed. The detector

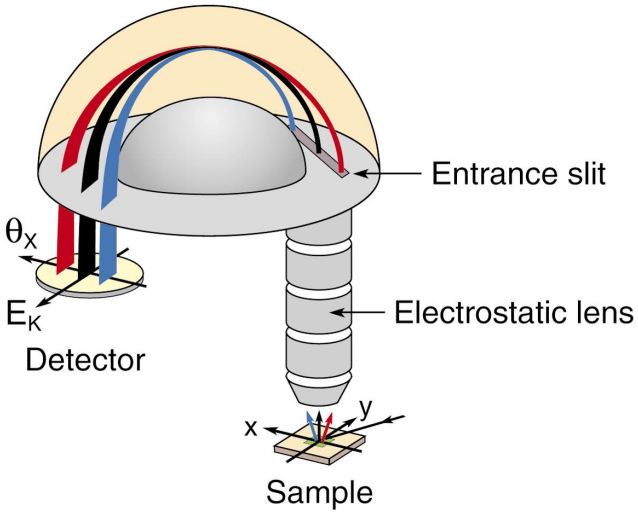

Figure 2.1. Diagram of a typical hemispherical energy analyzer for ARPES, from Ref.[55].

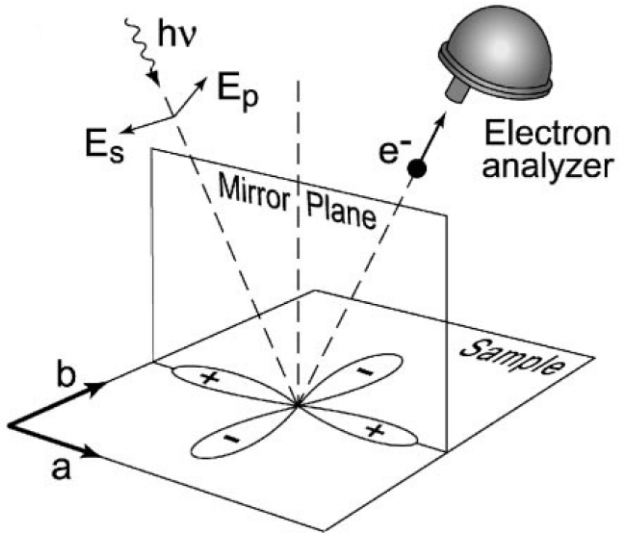

Figure 2.2. Photoemission geometry requiring p-polarized light in order to achieve nonzero $M^k_{f,i}$, from Ref.[55].

is in the plane determined by the incident light and sample normal, defining a relevant mirror plane. In order to photoemit electrons, there must be nonzero $M^k_{f,i} \propto \langle \phi^k_f | \vec{A} \cdot \vec{p} | \phi^k_i \rangle \propto \langle \phi^k_f | \vec{\epsilon} \cdot \vec{x} | \phi^k_i \rangle$ (invoking $\hbar \vec{p}/m = -i[\vec{x}, H]$ and defining $\vec{\epsilon}$ to be a unit vector along the direction of $\vec{A}$ and the light polarization). Both $M^k_{f,i}$ and the final state ϕ^k_f must be even upon reflection about the mirror plane in order to be nonzero within the plane, where the detector is. Thus, $\vec{\epsilon} \cdot \vec{x} | \phi^k_i \rangle$ must also be even. The orbital sketched there is even upon mirror reflection, and will thus require p-polarized light (light polarization within that plane) in order to be photoemitted. $M^k_{f,i}$ would go to zero for s-polarized light perpendicular to that plane, whereas initial states of odd parity would require s-polarized light.

Cross sections for different initial states can also depend strongly on photon energy. For example, the strength of photoemission from bonding versus anti-bonding bands in bilayer cuprate superconductors can be a strong function of photon energy and varies with crystal momentum across the Brillouin zone[77]. To study the bilayer splitting means adjusting experimental parameters such as photon energy so as not to be misled by matrix elements that favor anti-bonding over bonding bands[78,79].

2.1.5 Example ARPES spectra and energy and momentum analysis

Properly processed ARPES results consists of maps of photoelectrons as a function of crystal momentum along one, two, or three dimensions and binding energy, typically referenced to the Fermi level. Extraction of band dispersions, self-energies, and other features of the spectral function typically require careful analysis of spectra along one of those dimensions: through energy distribution curves (EDCs) or momentum distribution curves (MDCs).

The first approach, viewing the data through EDCs is most effective for studying energy-dependent features of the spectral function, such as self-energy[72] and energy gaps[80]. For example, consider the ARPES results of Fig. 2.3, from Ref.[72]. The two-dimensional map shows the spectral function $A(k, \omega)$ of the surface state of Mo(110). The inset highlights the near Fermi level features. One notices the band become broader as it disperses down from E_F.

However, the real insight comes from viewing individual line cuts at fixed k: EDCs, from which one can extract the contributions of various scattering mechanisms to the quasiparticles' self-energy. The top set of EDCs in the middle panel shows select EDCs taken between k_F, the Fermi momentum, and the band minimum. It is clear that the cut at k_F gives the narrowest peak; the peaks get broader as the band disperses down. Fitting the peaks with a Lorentzian yields quantitative results plotted in the right panel. The peak widths, which correspond to the imaginary self-energy, $2|\Sigma''(\omega)|$, show a sharp rise from when the band is at the Fermi level to ≈ 40 meV. Following that, they show a more gradual quadratic rise. The initial jump can be attributed to electron-phonon coupling while the quadratic increase

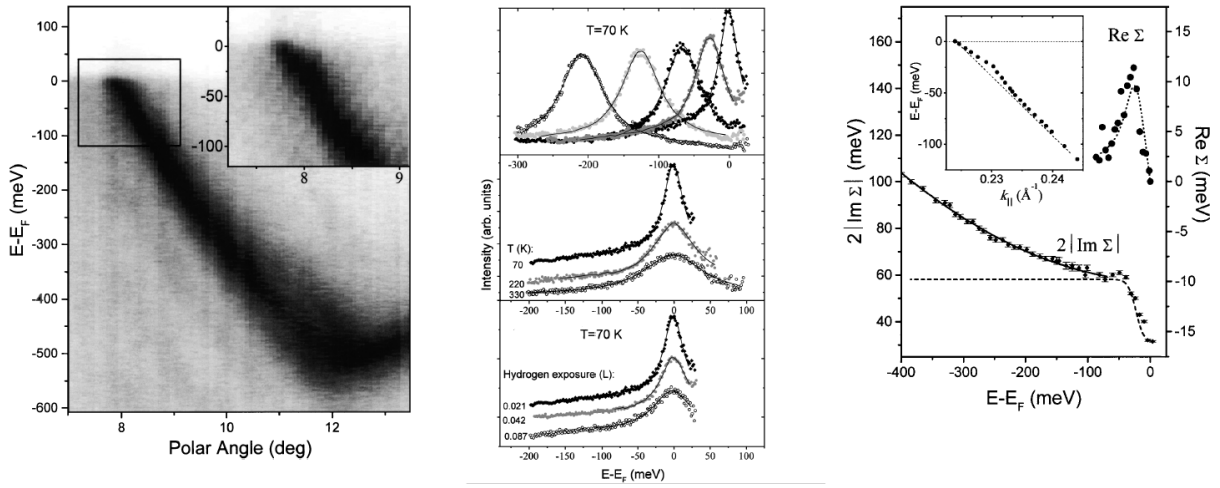

Figure 2.3. Photoemission maps and EDCs of Mo(110), from Ref.[72]. At left, a map of energy vs. momentum (which corresponds to photoemission angle). The inset shows near E_F features. The middle column shows EDCs as a function of binding energy, temperature, and surface exposure to gas, showing how the band broadens with each. At right, the real and imaginary self-energies, $\Sigma'(\omega)$ and $\Sigma''(\omega)$, respectively, extracted from the maps.

from the Fermi level to high energy is due to electron-electron scattering. Fitting allows for quantitative assessment of the magnitude of each scattering mechanism.

Moreover, one can extract the real self-energy $\Sigma'(\omega)$, the energy renormalization due to many-body effects. The inset of the right panel shows a bare band dispersion connecting the band at the Fermi level and at high binding energy. The deviation of the positions of EDC peaks from that straight line dispersion are plotted at right. They show a peak at $\approx$ 40 meV, where phonons most strongly interact with quasiparicles and the spectral function deviates most dramatically from the bare band dispersion.

Further insight can be gained from repeating these measurements as a function of temperature (middle plots in the middle panel) and surface exposure to hydrogen gas (bottom plots in the middle panel). With the former, one can see the peak at k_F broaden as the sample warms due to increased electron-phonon coupling. Extraction of $\Sigma'(\omega)$ and $\Sigma''(\omega)$ functions can be repeated at the various temperatures to coroborate the model of electron-phonon coupling.

Moreover, the peaks broaden with extra hydrogen exposure, which effectively adds to impurity scattering. Once more, extracting $\Sigma'(\omega)$ and $\Sigma''(\omega)$ as a function of gas exposure and extrapolating down to zero exposure gives the intrinsic contribution of impurity scattering to quasiparticle lifetimes.

As has been seen, EDC analysis is ideal for extracting self-energies. Careful analysis of spectra near the Fermi level also yields insight about superconducting gaps and pseudogaps: comparing EDCs at different momenta reveals the directional dependence of these[80].

For years, photoemission data were usually analyzed through EDCs as instruments lacked

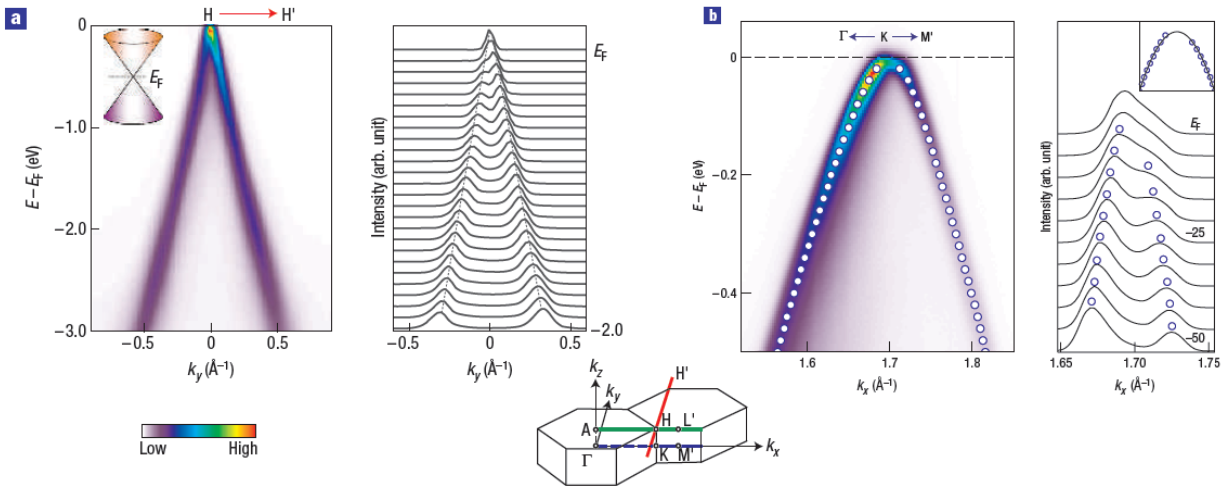

Figure 2.4. Photoemission spectra and MDCs of graphite, from Ref.[81]. At left, a Dirac cone at the H point. Peajs in the corresponding MDCs help verify the dispersion. At right, a parabolic dispersion at the K point, showing massive fermions.

the momentum resolution to see MDCs. Most of the results presented in this dissertation will be presented as EDCs or as two-dimensional maps because that is how the spin-resolved spectrometer acquires data. More on that in the next section.

On the other hand, MDC analysis is most useful for studying band dispersions without worrying about energy-dependent effects. Taking a slice at constant energy means not needing to worry about the Fermi function f(ω) or self-energy, which is typically only weakly momentum dependent within an area study. Fitting MDC peaks is thus the most straightforward way to place the bands.

For example, Fig. 2.4 shows ARPES maps from graphite, as reported in Ref.[81]. In 2.4a, we see the bands at the H point, with individual MDCs shown on the right. By finding the momenta of each peak, one can track the band dispersion across MDCs and readily verify the linear, Dirac-like band structure. In contrast, 2.4b shows the band near the K point, which deviates slightly from linear. Even though the two branches of the band have very different intensity, the authors were able to find the positions of the peaks of each with Lorentzian fits. The accurate mapping of dispersion clarifies the point that the band is parabolic: these fermions are massive.

In this way, ARPES was used to provide insight about a material through its bare band structure just as it was used in the previous example to learn about the many-body interactions in the material.

2.2 Spin- and Angle-Resolved Photoemission Spectroscopy

The preceding discussion of ARPES neglected an important degree of freedom for quasiparticles and photoelectrons: spin. Indeed, both the electronic structure and the photoemission process can carry spin dependence that can be investigated by measuring the spin polarization of photoelectrons. To see explicitly the spin dependence, we can write the photoemission intensity

$$I(k,\omega,\sigma) \propto |M^k_{f,i,\sigma}|^2 f(\omega) A(k,\omega,\sigma) \tag{2.13}$$

where $M^k_{f,i,\sigma} = \sum_{f,i} \langle \phi^{k,\sigma}_f | H_{int} | \phi^{k,\sigma}_i \rangle$. Hence, the final state spin is shaped by the spins σ of initial states $\phi^{k,\sigma}_i$, by spin-dependent interactions and relaxation processes accounted for by $A(k,\omega,\sigma)$, and by spin-dependent photoexcitation $M^k_{f,i,\sigma}$ selectively emitting electrons with spin σ.

Interest in spin polarized electronic states $\phi^{k,\sigma}_i$ provides the primary motivation for the development of spin- and angle-resolved photoemission spectroscopy (spin-ARPES), which has benefited the study of materials such as ferromagnets[82,83,84], Rashba systems[16,13,18,85,86,87,88] and topological insulators[89,90,91,92,93,94,37,95,96]. Indeed, without spin resolution, ARPES would be blind to some of the crucial properties of these materials.

In each case, electrons populating a particular band have a majority of spins point along a certain direction. In the case of ferromagnets, there is an exchange splitting between spins pointing along the direction of magnetization and those pointing opposite to it. Hence, at all momenta, the band structure is split in two, with minority spin bands pushed up in energy relative to majority spins.

In the cases of Rashba and topological insulator systems, a *spin-momentum locking* means that the direction that spins point depend on electron momentum within the Brillouin zone. Though there is no magnetization, no imbalance of spins along any spatial direction, there is an order to electron spins in k space. Hence, studying these materials requires a detector that can measure $I(k,\omega,\sigma)$, simultaneously resolving momentum, energy, and spin.

In truth, one does not measure the spin of an individual photoelectron, but the spin polarization along a chosen axis of an ensemble of electrons,

$$P(k,\omega) = \frac{I(k,\omega)_\uparrow - I(k,\omega)_\downarrow}{I(k,\omega)_\uparrow + I(k,\omega)_\downarrow}. \tag{2.14}$$

By measuring the relative intensity of photoelectrons with spin pointing up along the chosen axis, $I(k,\omega)_\uparrow$ and down along that axis, $I(k,\omega)_\downarrow$, it is possible to quantify the strength of preference for electron alignment. Spin-degenerate bands will have $P = 0$, while a band with all spins aligned together will have $P = \pm 1$. By quantitatively measuring the spin polarization as a function of energy and momentum, spin-ARPES is able not only to find spin splittings of bands, but to probe how different components of a wave function, such as

different orbitals, combine to create incomplete polarization $0 < |P| < 1$. Precise measurement of the spin polarization will become especially important in the time domain, when spin-dependent dynamical processes are studied.

2.2.1 Spin- and Time-resolved ARPES

There is yet one more parameter on which an ARPES map can depend: time since exciting a sample and driving its electronic population out of equilibrium. Indeed, the pump-probe technique has been used widely in spin-integrated ARPES to see how the electronic population behaves on a femtosecond or picosecond timescale after an intense laser pulse. By following this pump pulse at time t_0 with a probe at time t, the ARPES experiment now reveals $A(k, \omega, \sigma, t - t_0)$: the spectral function of the excited system.

Optical excitation that couples directly to the electrons in the system will drive population to states above the Fermi level. Initially, the electronic population may be non-thermal and not be well described by equation 2.13; over time the electrons can thermalize with each other, yielding an elevated electronic temperature for the Fermi-Dirac distribution $f(\omega, t-t_0)$. Eventually, they will thermalize with the lattice as the system returns to equilibrium.

The spectral function may change due to excitation of collective modes or altered electron coupling to those modes[97,27], altered electron correlation[98], or transient phase changes[99,80,100,101]. Sometimes pumping even alters the electronic structure itself by creating new states[102,103].

By tracking $f(\omega, t-t_0)A(k, \omega, \sigma, t-t_0)$, the pump-probe technique allows us to understand how electronic populations and band structure itself are affected by excitation, and what interactions are available to allow a material to return to equilibrium[104,105,106,107,108,109,110]. This technique reveals unoccupied band structure and yields insight about electron dynamics[111,112,113,114].

Interest in the fundamental physics and application of ferromagnets, topological insulators, Rashba systems, and other spin-orbit materials necessitates understanding how the spin degree of freedom affects electron dynamics. What distinct excitation and decay channels are available to different spins? Are transient spin polarizations created? Do electron populations depolarize?

Many experiments have measured $I(k, \omega, t - t_0)$, the transient photoemission spectra of materials without spin sensitivity, and some two-photon photoemission experiments have measured $I(\omega, \sigma, t - t_0)$ to study spin-resolved electron dynamics in ferromagnets without momentum resolution[115,116,117,118,119,120]. Spin- and time-resolved ARPES (STARPES), on the other hand, will measure $I(k, \omega, \sigma, t - t_0)$, resolving all of the degrees of freedom that are important to understanding decay channels, especially in the study of non-magnetic spin-orbit materials.

2.3 Photoemission effects yielding spin polarization

Having discussed how a spin polarized initial state $\phi_i^{k,\sigma}$ can be revealed by spin-ARPES, we now turn to how the photoemission process can yield a spin polarization different than that of the initial state. The dipole operator $\vec{A}\cdot\vec{p}$ that governs the interaction between photon and electron will not act on the electron's spin and alter the spin during photoemission. It can, however, photoexcite some spins more strongly than others.

2.3.1 Spin-dependent matrix elements

Spin-dependent matrix elements (SMEs) can occur in materials with significant spin-orbit coupling and are discussed in detail in Ref.[61]. Briefly, they have been observed in photoemission from core levels of various metals with strong spin-orbit coupling such as Cu[121], W[122], Pt[123], and Bi[37] and even from bulk bands[37,61]. In chapter 3 we present the important case of SMEs in Bi_2Se_3. A commonly exploited example of SMEs is the ejection of photoelectrons with spins into or out of the plane of a sample of GaAs when irradiated with circularly polarized light[6,124]. This effect has been used to generate spin polarized electron beams.

The photoemission matrix element $M^k_{f,i,\sigma} = \sum_{f,i}\langle\phi_f^{k,\sigma}|H_{int}|\phi_i^{k,\sigma}\rangle$ can be stronger for one spin than another (i.e., $M_{f,i,\uparrow} > M_{f,i,\downarrow}$) if that spin is coupled to orbital angular momentum. Different optically allowed transitions $\Delta j = 0, \pm 1$, $\Delta l = \pm 1$ have distinct probabilities, resulting in different intensities $I_\uparrow$ and $I_\downarrow$ in the presence of spin-orbit coupling. This fact can create a background spin polarization on top of that due to the initial state being probed.

For the case of linearly polarized light that is used in most of the experiments presented here, the three dimensional vector spin polarization due to SMEs is given by[125,61]:

$$\vec{P}_{SME} = \frac{2\xi(\hat{k_e}\cdot\hat{\epsilon})}{1+\beta(\frac{3}{2}(\hat{k_e}\cdot\hat{\epsilon})^2-\frac{1}{2})}[\hat{k_e}\times\hat{\epsilon}] \tag{2.15}$$

where $\hat{\epsilon}$ gives the direction of photon polarization and $\hat{k_e}$ gives the direction that a photoelectron travels from the sample to detector. β reflects the asymmetry in photoemission between opposite spin states and ξ comes from the interference between final states with $l+1$ and $l-1$ from an initial state with angular momentum l.

From this formula, we can observe that the SMEs depend on experimental geometry: they will be nonzero only if the angle between photon polarization and outgoing photoelectrons is finite but less than 90°. In the present experimental setup, this typically means that p-polarized light is incident on a sample 45° from the path from the sample to detector. Even as the sample is rotated to scan k space, this light polarization to detector geometry is constant. Indeed, in Bi_2Se_3 there was an SME-induced offset to the spin polarization that was constant across a momentum cut when probed with p-polarized light, but no such offset when probed with s-polarized light[37,61].

2.3.2 Differential coupling to wave function components

Similar to SME effects due to different excitation pathways, a particular photoemission geometry may preferentially eject electrons from a certain orbital or from real space parts of the crystal[75,76,29,28]. These wave function components may correspond to spin structure in the case of strong spin-orbit coupling and spin-polarized surface states. Chapter 3 will show how the spin polarization measured can depend on which orbitals are probed in an experiment.

Indeed, the final measured spin texture results from the interference pattern of electrons emitted from a mix of orbitals in the top several atomic layers, through which the spin texture may be changing.[76]. This interference process will depend strongly on photon energy, polarizaion, and angle of incidence, which all affect which orbitals are photoemitted and how much intensity comes from each near-surface layer. Zhu et al showed that this will cause the spin polarization to reverse as a function of photon energy in Bi_2Se_3, and we demonstrate experimentally that this occurs in Bi2212 in chapter 5.

Broadly speaking, the photoemission matrix elements that bring an electron from a sample to an ARPES detector can become more complex in the presence of spin-oribt coupling when the spin component of the wave function is of interest. Much of the work presented here studies that complication. While this means that spin-ARPES results must be interpreted with caution, it also means that the technique can give intricate details of the wave function of interest through its ability to preferentially probe certain orbitals or near surface layers. Geometric and photon energy considerations are key to interpretation.

2.4 Highly efficient spin-ARPES instrument

Having discussed the objects that contribute to the intensity $I(k, \omega, \sigma)$ measured by spin-ARPES, we now turn to how those measurements are actually performed. Any spin-ARPES instrument must combine some sort of angle-resolved electron spectrometer with a spin polarimeter.

The spin-ARPES technique is usually limited by very inefficient detection that forces the experimenter to use broadened energy and momentum resolution in order to achieve feasible count rates. Fundamentally, this limits potential experimental scope. There are two key problems: first, spin polarimeters only detect a small fraction of the electrons in a beam. Secondly, polarimeters lose all spatial information. Therefore, if detection of energy and momentum is done by spatially locating the photoelectron's trajectory, then only one point on an E vs. k map can be acquired at a time.

A surge in interest in spin-dependent research has resulted in numerous recent developments in improving the performance of spin-ARPES instrumentation[126,127,128,129,130,131,132,133,134,135]. One such spin-ARPES system is the 'spin-time-of-flight (spin-TOF)' spectrometer based on low-energy exchange scattering spin detection with TOF energy analysis[136]. This system, developed by Chris Jozwiak within the Lanzara group

and Advanced Light Source at Lawrence Berkeley Lab, provides greatly increased energy resolution and data acquisition efficiency.

In this section, we briefly discuss the original types of spin-ARPES instruments as well as the advances made by the new spectrometer developed in the Lanzara group. We further discuss quantitative measures of detector efficiency and statistical considerations on spin polarimetry.

2.4.1 Energy analysis in spin-ARPES

Most spin-ARPES instruments use a hemispherical energy analyzer of the sort described in section 2.1.3. The spin detector is positioned at a particular place at the end of the electron trajectory in the hemisphere, meaning that spin-resolved data are acquired at a single point in energy-momentum space at a time ('0-dimensional' detection). Rather than measure photoelectron kinetic energy by bending an electron's path, the Lanzara group spectrometer measures it by time from photoemission to detection at the end of a ≈1 meter drift tube. An aperture selects the photoelectrons emitted within a certain solid angle, selectable between ± 0.5° and ±2°, effectively setting the momentum resolution for the EDC being acquired.

TOF-based measurements boost overall efficiency by multiplexing energy detection and taking full spin-resolved energy distribution curves (EDCs) at once ('1D' detection)[128,129]. In this way, the spin-TOF system overcomes the inherent lack of spatial information in a spin detector by moving energy measurement to the time domain. This results in data acquisition that is at least one order of magnitude faster than with the common spin-ARPES approach that would need to separately acquire each data point. As a practical matter, many spin-ARPES works forgo measuring an EDC, instead cutting across momentum space at a constant energy (albeit at broadened energy resolution).

2.4.2 Spin Polarimentry

Mott detectors, the type of polarimeter that is commercially available, have been the driving force for new research on spin-dependent material properies. They detect the spin polarization of an electron beam by the spin-dependent scattering off of a material with strong spin-orbit coupling, often gold[137,138,126,139]. Mott detectors require electrons to be accelerated to relativistic kinetic energies: 40 keV or even 100 keV, causing most electrons to sail right through the target. Overall reflectivity is less than 1% of incident electrons. Thus, while Mott polarimeters are stable and relatively straightforward to use, they acquire data very slowly, limiting experimental scope.

The spin-TOF spectrometer improves the situation by performing spin polarimetry with a low energy exchange (LEX) polarimeter, based on scattering off of a ferromagnetic material. The significantly higher average cross sections of the low-energy scattering from the ferromagnetic targets[140,141,127,133] can provide nearly 100 times improved detection efficiency

relative to the high energy scattering from heavy nuclei targets in typical Mott-scattering polarimeters[142,143,139]. The improved electron reflectivity stems from the fact that the scattering can occur at relatively low kinetic energy, on the order of eV.

Below, we establish the metrics for polarimeter performance.

2.4.2.1 Sherman function and figure of merit for spin detection

The spin polarization P measured in a spin detector is proportional to the asymmetry of electron counts in two channels representing opposite outcomes of a spin-dependent scattering process. It is given by:

$$P = \frac{N_\uparrow - N_\downarrow}{N_\uparrow + N_\downarrow} = \frac{1}{S_{eff}} \frac{N_1 - N_2}{N_1 + N_2} \tag{2.16}$$

where the effective Sherman function, S_{eff} gives the ability of a spin detector to differentiate between spin-up and spin-down electrons along a given axis. A detector that perfectly discriminated between opposite spins would have a Sherman function of 1. In a Mott detector, channels 1 and 2 are intensitites measured after scattering to the left and right, respectively. In a LEX polarimeter, they are intensities measured when the scattering target is magnetized in one direction, and then in the opposite direction.

The overall performance of a spin detector is given by a figure of merit[143]

$$FOM = S_{eff}^2 \frac{N}{N_0} \tag{2.17}$$

that quantifies how quickly it enables a spin measurement[136]. N/N_0 is the overall reflectivity of the target: the fraction of electrons that scatter off the target and reach the detector to be counted.

An ideal spin detector will have a high reflectivity and high Sherman function, meaning that a large percentage of electrons will be counted and more specifically, counted with other electrons of the same spin. Both the reflectivity and Sherman function depend on electron kinetic energy and thus need to be calibrated in the range of kinetic energies in which they will be operated.

2.4.2.2 Statistical Error Analysis

Spin detectors do not measure the spin of individual electrons but rather the spin polarization of an ensemble of N electrons out of the N_0 electrons incident upon the target. Thus, even if instrumental experimental geometry-based sources of error are eliminated or calibrated, there will always be statistical uncertainty in the spin polarization measured, given by[136]:

$$\Delta P = \frac{1}{\sqrt{N} S_{eff}} = \frac{1}{\sqrt{N_0 \times FOM}} \tag{2.18}$$

Thus, we can see that a spin detector with a Sherman function closer to 1 or with an overall greater figure of merit will need fewer counts to reach a certain precision of measurement. Because it can more effectively discriminate between electrons of opposite spin, it needs fewer electrons to determine the overall balance of spin-up versus spin-down, and measurements can happen more rapidly.

2.4.2.3 Quantitative performance of LEX versus Mott polarimeter

Mott detectors typically have Sherman functions of 0.1-0.2[137,138,126,139], meaning that five to ten times as many counts are needed to reach a certain singal to noise ratio, compared to a spin-integrated measurement. Scattering targets in exchange polarimeters tend to have strong peaks in their effective spin-analyzing power, with reported values up to $S_{\text{eff}} \sim 0.4$[141,127,133]. This is due to the different densities of states for majority and minority spins in the ferromagnetic target. Single-energy-channel systems take advantage of these peaks by tuning the single scattering energy to the maximum FOM.[141,127,144,133].

To enable multiplexed energy detection, the exchange polarimeter in the spin-TOF spectrometer must function with a > 1 eV range of scattering energies. A 50 ML Co/W(110) scattering target is chosen, making use of scattering energies in the range of 6 - 10 eV where the S_{eff} is not peaked, but quite independent of scattering energy, to simplify analysis. Figure 2.5, from Ref.[136] demonstrates that while a higher figure of merit could be achieved at lower energy, this choice allows a single value of S_{eff} to be used for the entire range of data acquired[136]. Improved vacuum and Co surface growth since Ref.[136] have provided for a higher $S_{\text{eff}} \sim 0.2$ in this energy range.

As mentioned previously, the strong advantage of the LEX detector over Mott detectors comes from its reflectivity. Typical Mott detectors will have reflectivities $<1\%$ and overall FOMs of 1-2 $\times 10^{-4}$. A LEX polarimeter can have reflectivity $>10\%$; in the energy range used by the spin-TOF, it achieves $\approx 6\%$. With the improved growth techniques, it now has a corresponding $FOM \sim 2.5 \times 10^{-3}$ in that range. After preparation, the scattering target can be used for $\gtrsim$ 1-2 days, and surface passivation techniques could be investigated to extend target lifetimes similar to Refs.[140,127,144,133].

Recently, other exciting developments in spin-resolved instrumentation have introduced a method for '2D' multiplexed spin detection with high Sherman functions ($S_{\text{eff}} \sim 0.4$) and full imaging capability[134,145,135,146], offering further efficiency gains for a range of spin-resolved techniques.

2.4.3 Overall efficiency of spin-TOF

The spin-TOF spectrometer brings together the ideal combination of time-of-flight spectroscopy, which is at least one order of magnitude more efficient that serial detection of kinetic energies in a hemisphere, and low energy exchange scattering polarimetry, which is two orders of magnitude more efficient than Mott polarimeters.

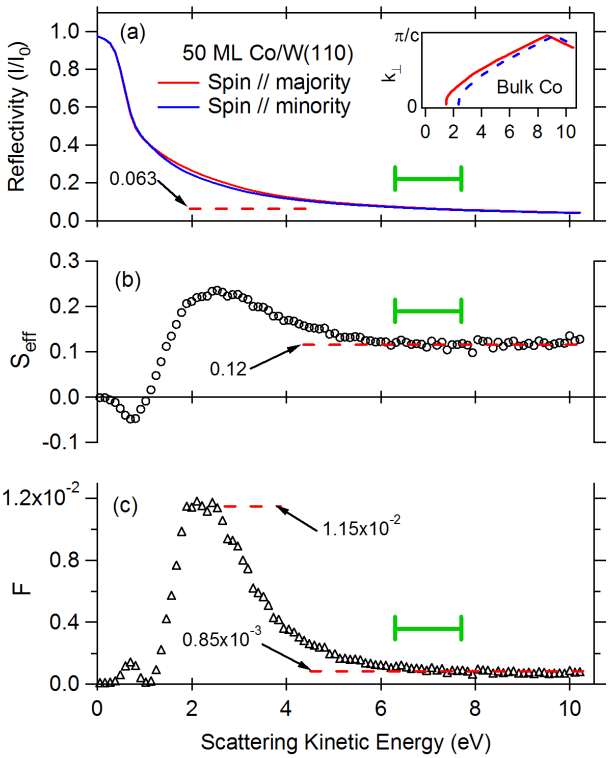

Figure 2.5. **Performance of the low energy exchange scattering polarimeter as a function of incident electron kinetic energy from Ref.[136] a,** Reflectivity for majority and minority spins in the magnetized Co. **b,** Effective Sherman function, relating to the difference in reflectivity of opposite spins. **c,** Figure of merit, peaked at low kinetic energy, but with a region highlighted in green where performance is flat as a function of kinetic energy.

The advantage is not that experiments are quantitatively three orders of magnitude faster than with a standard spin-ARPES setup, but rather that there are qualitatively new types of experiments that would be infeasible with lower efficiency. Not only do some of the experiments presented here have spin-resolved band structure maps along a whole cut through momentum space, but the experiments explored other parameters such as photon polarization, photon energy, sample temperature, and even pump-probe measurements in the time domain. All of these were taken without sacrificing resolution to the extent that would be needed with other instruments. These advantages become particularly apparent in spin-TOF measurements with a laboratory-based laser.

2.5 Light sources for spin-ARPES

Given the way ARPES results can depend on experimental conditions, various light sources can be used for experiments with different requirements. Choice of photon energy can set how much of energy and momentum space is accessible and the resolution with which they are probed. In addition, the timing structure of light: continuous wave versus pulsed, and duration and repetition rate of pulses, can have advantages and disadvantages for different techniques. In this section, we survey some of the light sources used for ARPES, then explain the advantages afforded to the spin-TOF by using an ultrafast laser.

2.5.1 Light sources for photoemission

Historically, synchrotrons were the primary light source for photoemission experiments. Their tunable photon energies and in some cases, polarization facilitate finding strong matrix elements and appropriate $k_\perp$ to probe a state of interest. Different synchrotron beamlines will be optimized for different photon energy ranges: HERS at the Advanced Light Source works well at hν ≈30-60 eV while MERLIN is optimal between hν ≈70-110 eV.

Following work by Koralek *et al*[56], pulsed oscillator lasers have been used to provide very high energy and momentum resolution ARPES measurements[70,56,147,148,149,150,151,152]. Relative to other sources, solid-state laser-based sources have very high photon flux, and the low photon energies can provide strong signal, enhanced momentum resolution, increased bulk sensitivity, and simple photon polarization control. The low photon energy of 6 eV limits experiments to near the Fermi level and Brillouin zone center. Not only do these lasers enable experimentalists to conduct measurements outside of infrequent synchrotron beamtimes, but their ultrafast pulses can be readily adapted to the pump-probe technique, in which ARPES images out-of-equilibrium dynamics in a material after excitation[57,97,153,154,155,156,111,157,107,112,80].

Gas discharge lamps are used for laboratory-based measurements at a fixed photon energy in the range of 8-11 eV for Xe lamps and 21 eV for He lamps, enabling a wider search of the Brillouin zone than can be achieved with hν= 6 eV.[158]. More recently, laboratory-based

pulsed lasers with photon energies of, e.g., 7.5 eV[79] and 11 eV[159] as well as high harmonic generation systems at 22 eV and greater[160] have brought some of the benefits of low and mid-photon energy ranges to timing-based laboratory experiments.

Consistent, with the broader ARPES technique, spin-ARPES systems are most frequently utilized at synchrotron undulator beamlines[3,128,127,132,133] or with high-flux UV lamps[3,126,131,133,134]. The next section, however, discusses the advantages of combining the spin-TOF spectrometer with a laboratory-based laser.

2.5.2 Laser-based spin-ARPES

The spin-TOF spectrometer was designed for synchrotron light sources to take advantage of their high brightness, excellent stability, and wide-range tunability. It demonstrates high performance with synchrotron use[37] but requires a light source with a pulsed time structure that is typically only available for limited amounts of time at most synchrotrons.

Laser sources provide another powerful way to make use of the high efficiency of the spin-TOF system, and when we coupled a laboratory laser to the spectrometer, we found the combined system to give outstanding performance. The pulsed nature of many laser systems also allows natural integration with TOF spectrometers[129,151,161] in addition to allowing ultrafast pump-probe style time-resolved experiments[57,97,153,154,155,156,111,157,107,112,80]. This section presents the highly efficient coupling of the spin-TOF ARPES system with the 4th harmonic light of a cavity-dumped laser system for unprecedented high-speed and high-resolution near-E_F spin-resolved data acquisition.

The experimental setup is shown in Fig. 2.6. A 6 W frequency-doubled Nd:YVO_4 laser pumps a cavity-dumped Ti:sapphire oscillator (Coherent Mira), which generates ≈150 fs pulses tuned to 828 nm (∼1.5 eV). The cavity dumper gives selection of the output repetition rate to be $\sim 54.3/n$ MHz ($n = 1, 2, 3, ...$), allowing repetition rates to be matched to the TOF requirements in each experiment, typically several MHz. The photon energy is frequency-quadrupled to 5.99 eV through second harmonic generation by two cascaded type-I phase-matched beta barium borate (BBO) crystals of thickness 2mm and 5mm. The UV light is then focused onto the sample, entering the chamber through a fused silica viewport.

The pairing of the spin-TOF spectrometer with the cavity-dumped 6 eV laser system has several advantages that give significant gains in performance. Indeed, a rapidly growing literature of regular spin-integrated ARPES experiments demonstrates key benefits of similar laser-based systems for ARPES in general, including extremely high signal due to high photon flux and high photoemission cross sections[70,162,149,150,151,152]. Furthermore, the low kinetic energy of the resulting photoelectrons results in quite high momentum resolution for a given instrumental angular resolution, as momentum resolution scales as the square root of the photoelectron kinetic energy[163]. With angular resolution of $\pm 1^\circ$, it achieves a total momentum resolution of 0.02 $Å^{-1}$. The low photon energy also provides a measure of improved bulk sensitivity due to the typically longer mean free paths of such low energy photoelectrons[164,70,56].

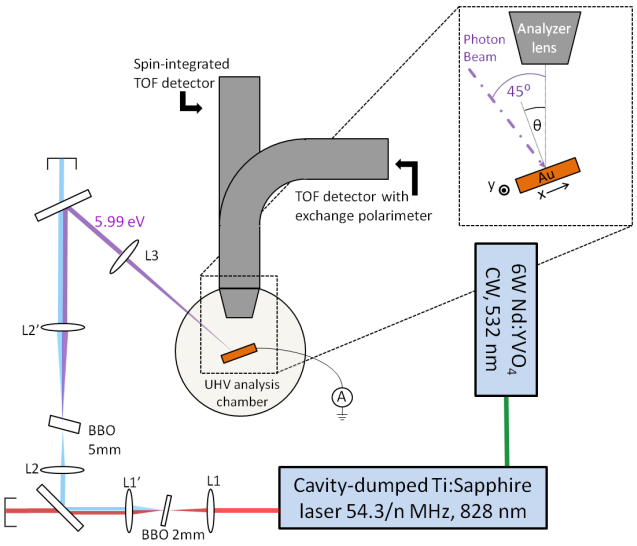

Figure 2.6. Experimental setup of spin-TOF system with laser. A Nd:YVO_4 laser pumps a cavity-dumped Ti:sapphire laser. The pulsed 828 nm light is twice frequency doubled by two type-I phase-matched- beta barium borate (BBO) crystals of thickness 2mm and 5mm, yielding 207 nm, 5.99 eV pulsed light. Focal lengths are L1=L1′=10 cm, L2=10 cm, L2′=20 cm, L3= 30 cm.

The low photoelectron emission kinetic energy has further benefits specific to the TOF technique. Indeed, since the energy resolution (ΔE) of TOF is proportional to the 3/2 power of the photoelectron flight, or drift energy ($\Delta E \propto E_D^{3/2}$), the technique is most powerful with very low drift energies[165,128,129]. The spin-TOF achieves a total instrumental energy resolution of 14 meV under realistic experimental conditions. To our knowledge, this is the highest energy resolution in a spin-resolved ARPES experiment demonstrated by direct fitting of spin-resolved intensities. Recent high profile spin-resolved ARPES works have been performed at ∼80 meV resolution[18,89,92,166], while others have pushed resolutions to 40 meV[93,94,167,168], 30 meV[91,22] and 25 meV[95,96]. We note that slightly higher energy resolutions have been shown in other spin-resolved setups during system calibrations using extreme settings[131,133]. However, these systems have been operated at broadened resolutions in subsequent realistic spin-resolved measurements, e.g.[93,95].

Higher photon energies require electron optics to be set to retard photoelectrons[165,128], which can result in a loss of collection efficiency. The low initial emission kinetic energy with the 6 eV photons means electrons do not need retardation, and can even be accelerated, giving high collection efficiency while still giving high energy resolution. The spin-TOF's integrated bandpass filter passes a ∼1 eV range of kinetic energies[136], sufficient for the full spectrum emitted by a 6 eV laser. Finally, the selectable repetition rate afforded by the current laser system's cavity dumper allows the repetition rate to be optimized for a given experiment, tailored to give the highest repetition rate (for the highest average count rate) that is compatible with the TOF technique and the selected drift energy[136].

For many materials, the spin-TOF can acquire spin-resolved EDCs with high statistics in just several minutes. An example spectrum is shown in Figure 2.7, acquired from the Rashba

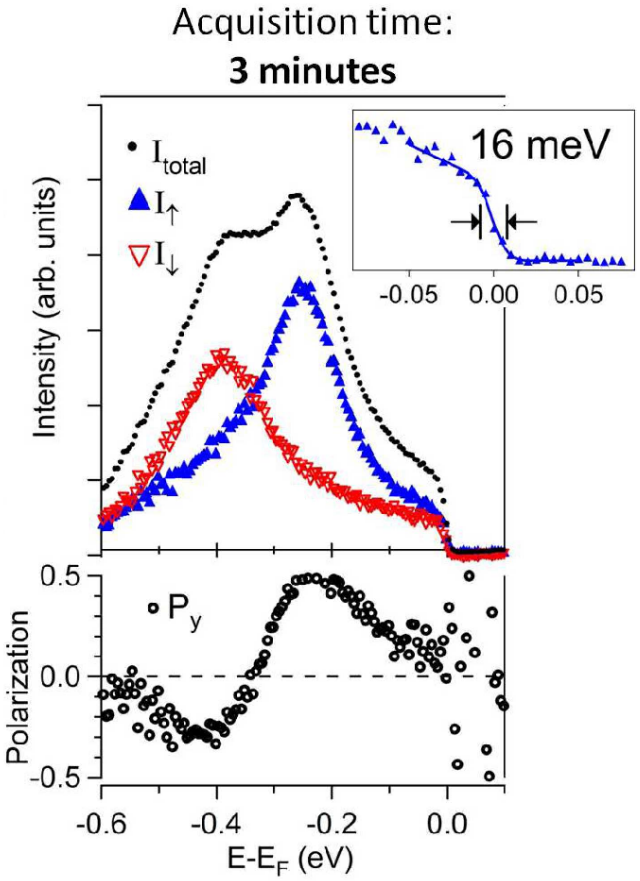

Figure 2.7.

Example spin-resolved EDC from Au(111) Rashba surface state. EDCs for spin-up (blue) and spin-down (red), plus total photoemission intensity. Below, the spin polarization is the normalized difference between spin-up and spin-down EDCs. The inset shows a 16 meV edge. Removing the contribution of the intrinsic Fermi edge width of 7 meV (corresponding to the sample temperature of ∼20 K) gives a total instrumental energy resolution of ∼14 meV.

state on the Au(111) surface. While this physics of this system are discussed in the next chapter, these EDCs demonstrate the capabilities of the spin-TOF. The blue EDC shows intensity of spin-up electrons as a function of binding energy; the red EDC shows the same for spin-down electrons. The total intensity (black) that would be seen in a spin-integrated ARPES instrument does not readily show the Rashba splitting that is clearly apparent in the spin-resolved data. Below, the spin polarization is the normalized difference between red and blue EDCs and shows a clear reversal of spin as a function of binding energy. These very high signal-to-noise data were acquired in just three minutes. Other instruments based on a hemispherical energy analyzer and Mott polarimeter might need several hours for a similar acquisition with broadened resolution.

The extreme low photon energy of the current laser system, of course, limits ARPES experiments to systems with low energy electronic states within an eV of E_F and near the Brillouin zone center due to conservation of energy and momentum[163]. However, the above advantages give the present setup unprecedented resolution and data collection efficiency for studying electronic states near the Fermi level in systems that are accessible with the low photon energy, such as 'near-nodal' states in cuprate superconductors[56,153,80] or the surface states of topological insulators[151,152,156,61].

For the study of materials and electronic structures compatible with the low photon energy, this system offers the capability of spin-ARPES measurements with uniquely high energy resolution and scope. The power of the high data acquisition speed is demonstrated by acquiring full spin-resolved energy-momentum maps, as opposed to single EDCs or MDCs. The high-speed data acquisition can also be leveraged for efficiently performing spin-ARPES with high resolution along additional dimensions of experimental parameter space, such as sample temperature[83,169,82] or photon polarization[61]. Most of the results of chapters 3, 4, and 5 were taken with the 6 eV laser. As the spin degree of freedom continues to rise in importance to a wide range of fundamental and applied condensed matter research, these capabilities have much to offer.

Highly efficient instrumentation is critical for such experiments to be performed with high resolution. The demonstrated high efficiency of the present system shows high potential for simultaneous time- and spin-resolved ARPES experiments with high resolution for powerful and direct insights into spin dynamics. Such experiments could be fundamental in the study of ultrafast magnetization dynamics and control[170,171,172] or spin dependent dynamics in topological insulators[173,156,111,174,112]. The adaptation of the system for time-resolved measurements in presented in the next section.

2.6 Spin-, Time-, and angle-resolved photoemission spectroscopy

To understand the spin dependence of how materials behave out of equilibrium, one must measure the populated electronic structure as a function of energy, momentum, spin *and* pump-probe delay time. Achieving a high signal-to-noise ratio in comparing spectra before and after pumping requires very efficient instrumentation, a great challenge for any spin-resolved experiment. Even spin-integrated time-resolved ARPES experiments are typically very time consuming due to the added experimental dimensionality and the often small change in photoemission signal of interest compared to equilibrium signal.

Nonetheless, there has been considerable progress in the historically inefficient spin-ARPES technique, bringing the time domain within reach[175,176]. We have adapted the spin-TOF spectrometer and laser system for resolving all of these degrees of freedom, the first dedicated tool for spin-, time-, and angle-resolved photoemisson spectroscopy or STARPES. Details of the system are given below.

2.6.1 Time-resolved optical apparatus and techniques

The intrinsic time structure of the Ti:sapphire laser system, with pulse widths down to ∼100 fs possible, naturally enables extension of the system to pump-probe style experiments[57,97,153,154,155,156,111,157,107,112,80]. Figure 2.8a demonstrates the concept of such a measurement. An intense infrared laser pulse irradiates the sample to drive it out of equilibrium, exciting electrons from below the Fermi level to unoccupied states above. Subsequently, an ultraviolet pulse causes photoemission of electrons that are detected by the spin-resolved spectrometer. By controlling the time delay between pump and probe pulses, the spin-dependent electronic population can be imaged at different amounts of time after excitation as electrons are relaxing back towards equilibrium.

A diagram of the instrumental setup is shown in 2.8b. The optical path is similar to one used for pump-probe spin-integrated ARPES measurements[58]. The 1.5 eV light of the laser is put through a 1 mm thick type-I β-barium borate (BBO) crystal, which upconverts a portion of it to 3 eV. The second harmonic light is split off with a dichroic mirror and put through a second 0.5 mm BBO crystal to undergo another stage of frequency doubling to the 6 eV light that is used for photoemission, as had been done for equilibrium measurements. Meanwhile, the remaining fundamental light is used to pump the sample. It reflects off of a retroreflective mirror on a motorized stage (Newport GTS150) with position repeatable to ±100 nm. The position of this mirror is moved to adjust the path length of the pump pulse and therefore its timing relative to the probe. Optional wave plates can be inserted in each beam path to control the polarization of both pump and probe beams.

Both beams are focused to the same spot on the sample. Initial spatial alignment is achieved by imaging the beamspots on a phosphor-coated copper puck, mounted where

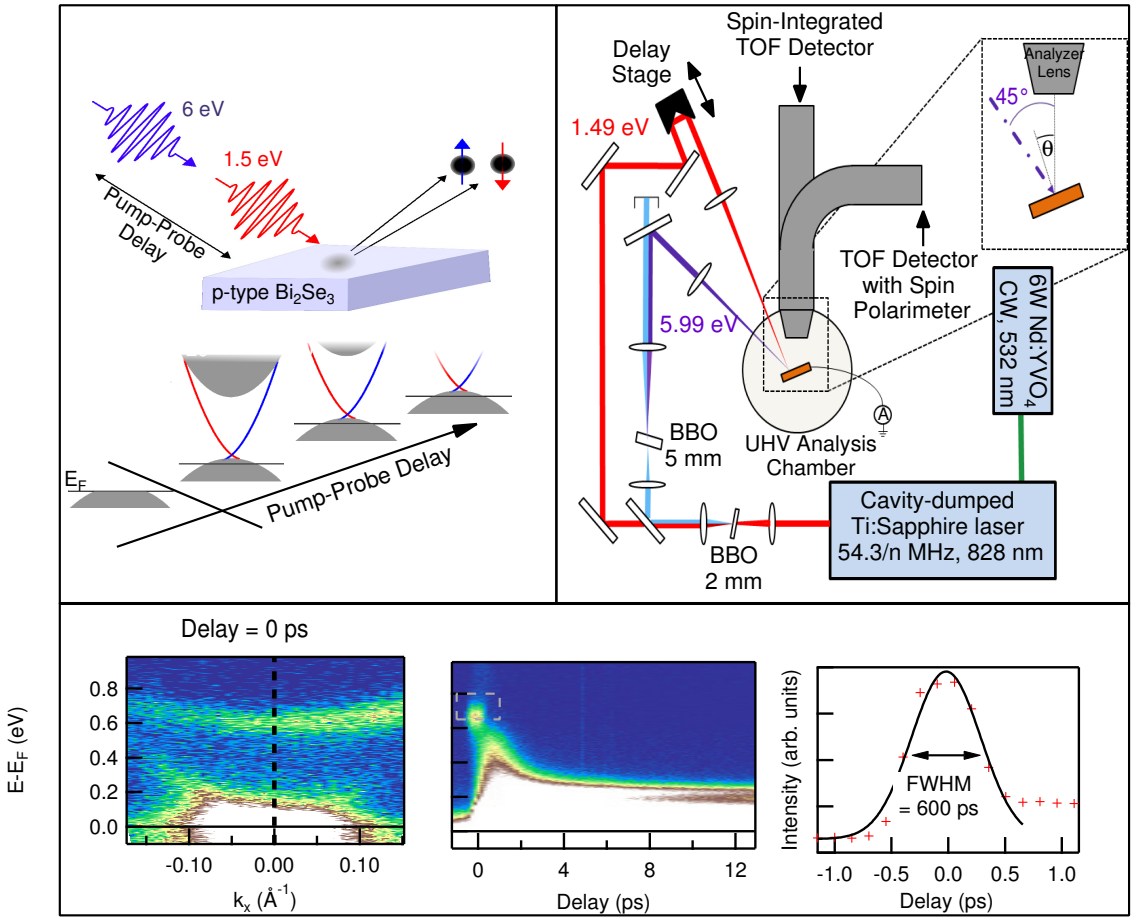

Figure 2.8.

The spin-resolved pump-probe experiment. **(a)** Cartoon of the measurement procedure, in which an ultraviolet probe photon follows an infrared pump photon by a controllable delay time. Photoelectron energy, angle, and spin are measured. These yield spin-resolved maps of the band structure at various delays after excitation of electrons. **(b)** Schematic of the experimental layout. An ultrafast laser produces 1.49 eV light, some of which is used to pump the sample, and some of which is frequency quadrupled to create 5.99 eV light for photoemission. **(c)** Measurement of the time resolution through the photoemission intensity of an image potential state.

samples will be in the measurement chamber. This is fine-tuned by maximizing the count rate above the Fermi level in an actual ARPES measurement. A removeable mirror is able to redirect the beams to a camera for profiling, revealing a ≈ 100 µm radius for the pump and ≈ 50 µm for the probe. The pump beam is larger than the probe so as to ensure that only pumped sample surface is being measured. The pump fluence is tunable up to $\approx 30\mu\text{J/cm}^2$. The tunability of the laser repetition rate is crucial for time-resolved ARPES, as lowering the repitition rate can allow for higher pump fluence from an indiviual pulse, or can provide more time for dissipation of thermal energy between pulses[153,177,80,58].

Rough temporal overlap of pump and probe beams is found by measuring a shift in the band energy of the GaAs valence band due to a surface photovoltage effect[178]. This effect persists for >100 ps towards negative time delay (probe preceding pulse) and does not require excellent spatial overlap of the beams, facilitating initial identification of the time when the two pulses are coincident.

The temporal overlap of the beams can be measured by the occupation of a short-lived image potential state (IPS) on the surface of Bi_2Se_3 that is populated by p-polarized 6 eV photons and emitted from by p-polarized 1.5 eV photons[156]. Figure 2.8c shows this state high above the Fermi level, dispersing as a free electron band. A series of EDCs taken at the Γ point at a range of pump-probe delays shows that the IPS appears and disappears before most of the electron dynamics in the surface state and conduction band begin (those dynamics are discussed in the next chapter). Integrating the electronic population within the range of energies of the IPS measures the convolution of the two beams' intensities in time. These integrated counts show a full width at half maximum of 600 fs, providing an upper bound on the time resolution.

Adding the new dimension of time to the experimental phase space is only realistic because of the high efficiency of the spectrometer: high signal-to-noise delay scans would be infeasible if EDCs were acquired more slowly. Simultaneous energy, angle, and spin resolution have been needed to uncover the momentum-dependent spin texture of materials like topological insulators. Now, only by adding time resolution while measuring all of these degrees of freedom can spin dynamics be measured, affording a window into the spin-dependent interactions that electrons experience in a material. The new insight that will come from watching magnetic and spin-orbit materials in the time domain will help explain the fundamental spin-related properties of the materials and demonstrate how they might perform when incorporated into a device and driven away from equilibrium.

The experimental apparatus described here was used to study dynamics in a topological insulator and learn about the nature of the topological phase transition[63]. In the next chapter, we present insights on how spin-orbit coupling shapes surface states based on equilibrium and dynamical measurements.

Chapter 3

Entangled Spin-Orbital Textures in Surface States

Materials with strong spin-orbit coupling and spin-split surface states have garnered significant attention for possible use in spintronic devices, in which the spin degree of freedom would be manipulated electrically[39,16,13,18,88,31,35,36,179,26,180,181,19,172]. This is thanks to a spin-momentum locking, in which an electron's momentum forces its spin to point a certain way. Thus, passing current through a material would magnetize it.

While the proposed utility of Rashba or topological surface states stems from their spin textures in momentum space, this chapter will show that spin textures can carry complexity not usually considered, following Jozwiak *et al*[61]. We will show that spin-ARPES is the tool to use to fully map out and understand all of the degrees of freedom of these surface states. We begin with an introduction to Bi_2Se_3 , a very commonly studied topological insulator. We then present spin-ARPES results on it that show how the spin and orbital components are entangled and we compare these findings to a prototypical Rashba system. Finally, we present time-resolved measurements on Bi_2Se_3 to demonstrate how the spin-dependent dynamics that can be probed.

3.1 Bi_2Se_3 : a prototypical topological insulator

This chapter will present several spin-ARPES results from Bi_2Se_3 . Indeed, this material is one of the topological insulators most frequently measured in ARPES experiments because it is very easy to work with. Its crystal structure is very similar to related materials like Bi_2Te_3 and Sb_2Te_3, so it provides generalizable lessons for these other topological insulators.

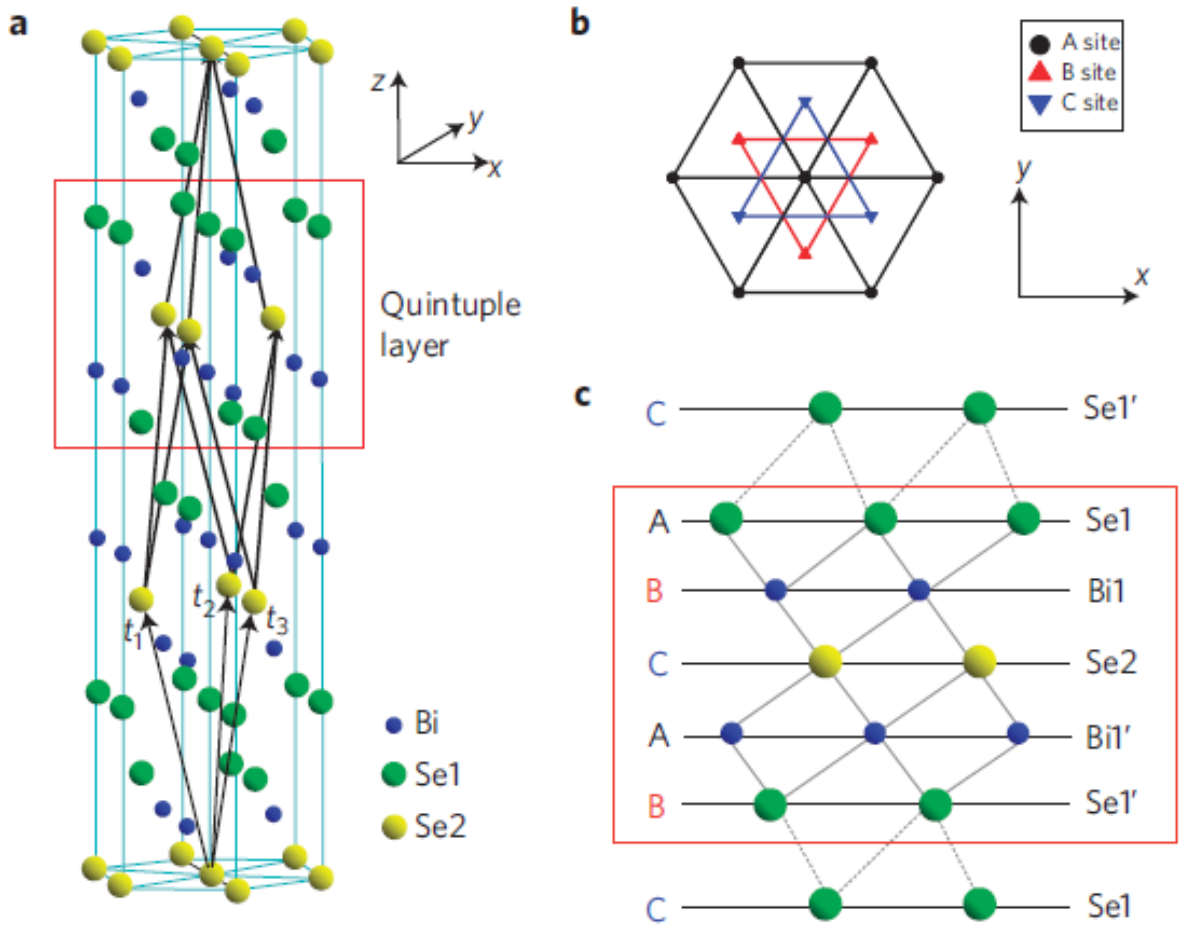

Figure 3.1. **Bi_2Se_3 crystal from Ref.[182].** **a,** Several unit cells, with a single quintuple layer in the red box. **b,** View of the crystal from above **c,** Side view of the crystal, again with a single quintuple layer in the red box.

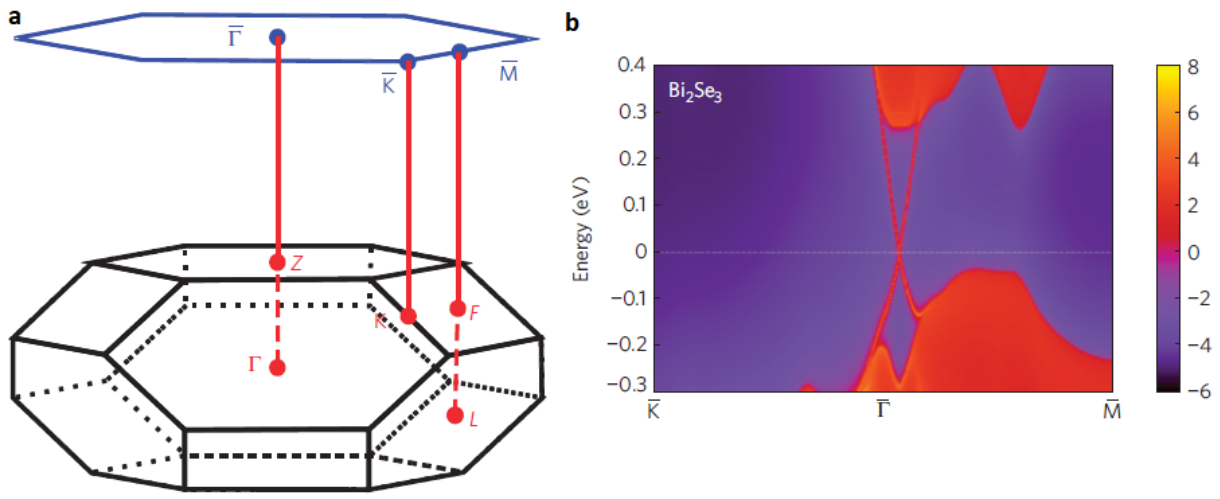

Figure 3.2. **Bi_2Se_3 Brillouin zone from Ref.[182]. a,** Three dimensional Brillouin zone, with the surface-projected two dimensional zone that is relevant for studying surface states. **b,** Calculated band structure near the Fermi level and Γ point.

Bi_2Se_3 has a rhombohedral crystal structure, as shown in Figure 3.1a. It is composed of atomic quintuple layers (QLs): Se-Bi-Se-Bi-Se layers bonded to each other. Each atomic layer has a triangular lattice, as shown in Figure 3.1b, and within a QL, the middle Se layer acts as an inversion center, carrying the Bi and outer Se layers into each other. QLs are stacked and held to each other by van der Waals forces such that coupling is much stronger within a single QL than among adjacent QLs. This creates a natural cleavage plane between QLs, allowing Bi_2Se_3 to be consistently cleaved very easily, exposing a Se surface.

Figure 3.2a shows the Brillouin zone of Bi_2Se_3 , along with the hexagonal two dimensional surface-projected zone that is used in studying surface states. The high symmetry points of Γ, M, and K are all indicated: most results in this work will be along Γ-M or Γ-K directions. In particular, Γ-M is within a bulk mirror plane of the crystal.

Figure 3.2b shows band structure calculated by Ref.[182]. The bulk valence and conduction band continua are evident near the top and bottom of the figure with a $\approx$ 300 meV gap between. A single cone, the topological surface state, crosses the gap and connects the bulk bands. Note that because these states are localized at the surface, this band would not exist within the bulk of material. In this calculated band structure for stoichiometric Bi_2Se_3 , the Fermi level cuts right through the Dirac point. Real samples, however, tend to be n-type as Se vacancies form and drive the Fermi level into the conduction band.

To understand why Bi_2Se_3 is a topological insulator, consider the energy diagram of Ref.[182] for the atomic states that constitute the bulk valence and conduction bands. The Se atomic $4p$ levels are energetically lower than Bi $6p$ levels, as demonstrated in Figure 3.3a. However, for the hybridized states within the crystal, spin-orbit coupling is strong enough to switch the energy ordering of the two p_z levels nearest the Fermi level, which have opposite parity. When the strength of spin-orbit is turned up, as in 3.3b, the conduction and valence

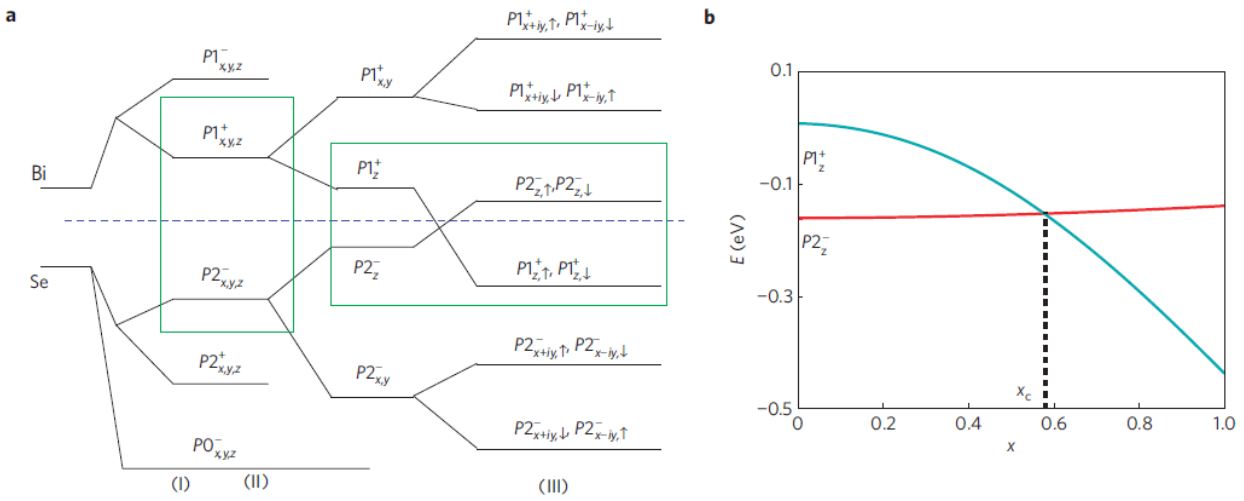

Figure 3.3. **Energy levels of Bi and Se p orbitals in Bi_2Se_3 from Ref.[182]. a,** Energy ordering of electronic levels in going from atomic Bi $6p$ and Se $4p$ to (I) chemically bonded hybridized orbitals, (II) orbitals within the crystal field, in which p_z orbitals are split off from $p_{x,y}$, and (III) spin-orbit effects are turned on. **b,** Energies of the two levels nearest the Fermi level, as a function of spin-orbit coupling strength, showing that their energy ordering inverts due to the interaction.

bands cross each other: an inversion that must be undone at the surface with the topologically trivial vacuum. Hence, a Dirac cone is formed connecting the two.

Among topological insulators, Bi_2Se_3 is especially appealing to study with ARPES because of the simple surface band structure: the topological surface state remains nearly conical throughout the gap. Moreover, this important feature is very near to the Γ point, making it accessible with low 6 eV photon energy and very easy to locate in an ARPES experiment. Lastly, a nice benefit of the topological origin of the surface state is its robustness; nature requires any cleaved surface to have it.

3.2 Spin reversal in Bi_2Se_3

There have been many angle-resolved photoemission spectroscopy (ARPES) and spin-resolved ARPES studies of the topological surface state (TSS) in Bi_2Se_3 and other topological insulators[59,183,184,185,37,156]. This state's Dirac cone is commonly thought of as having a chiral spin texture in which all electrons have their spins locked perpendicular to their momentum.

Figure 3.4 presents spin-integrated and spin-resolved measurements of Bi_2Se_3. These data come from a bulk sample cleaved *in situ* and held at a temperature of 80 K. 3.4a presents a Fermi surface and 3.4b presents a cut through k space, acquired with 35 eV photons. Arrows indicate expected spin directions. The Fermi surface features a ring centered on Γ stemming from the TSS. Inside, the bulk conduction band contributes weight broadly. In 3.4b, the

TSS forms a cone of linearly dispersing "massless" Dirac fermions. The Dirac point (where the two branches of the cone meet) is roughly 350 meV below E_F: undoped Bi_2Se_3 naturally develops Se vacancies and appears n-type. The bulk conduction band is the broad feature inside the upper half of the cone. The bulk valence band overlaps with most of the bottom half of the cone, though its weight does not show up intensely with this photon energy.

3.2.1 Tunable spins

Fig. 3.4c shows a spin-resolved energy distribution curve (EDC) measured at k_F, along the dashed green lines of 3.4b. These measurements with made with 6 eV photons of the laser-based spin-ARPES described in the previous chapter. The blue EDC represents intensity of electrons with spin-up along the in-plane axis perpendicular to k; the red EDC represents spin-down electrons. As expected, the blue EDC dominates. Below, the plot of spin polarization as a function of energy makes this point without reference to total photoemission intensity: the TSS has spin polarization >70%. However, it turns out that this measurement is very dependent on the geometry with which it is made.

Fig. 3.4e shows the experimental geometry used for spin-resolved measurements. The light arrives 45° from the direction that emitted electrons are detected. Spin is measured along the $\hat{y}$ direction. When s-polarized photons are used, the light is linearly polarized along $\hat{y}$, i.e. vertical in the plane of the sample surface. P-polarized photons, like the ones used in 3.4c, are perpendicular to this, with components in $\hat{x}$ and $\hat{z}$.

Fig. 3.4d demonstrates the important role photon polarization plays: s-polarized photons used to probe the exact same angle as in 3.4c will yield the opposite spin polarization. Nothing is changed between the two measurements other than the direction of linear photon polarization, and yet the spin of photoelectrons coming from this surface state is fully reversed.

Moreover, the spin polarization can be fully adjusted from up to down by rotating the angle of light polarization, α_0, between p- (0°) and s-polarized (90°). Fig. 3.4f demonstrates this complete in-plane tunability. This reversal of spin polarization merits further investigation, enabled by the high efficiency of the spin-TOF instrument.

3.2.2 Full momentum mapping

Figure 3.5 shows spins as a function of momentum. The polar angle, θ in 3.4e, is rotated to measure electrons at different emission angles, corresponding to different momenta along a Γ-M cut through k space. In 3.5, the first map at left shows the bands as a function of energy and momentum as probed by p-polarized light. The two-dimensional colorsale, shown at far right, shows total photoemission intensity as darkness, while spin polarization is shown as color from red to blue.

In 3.5a, the left branch of the cone is blue for spin-up, as expected for the helicity of the

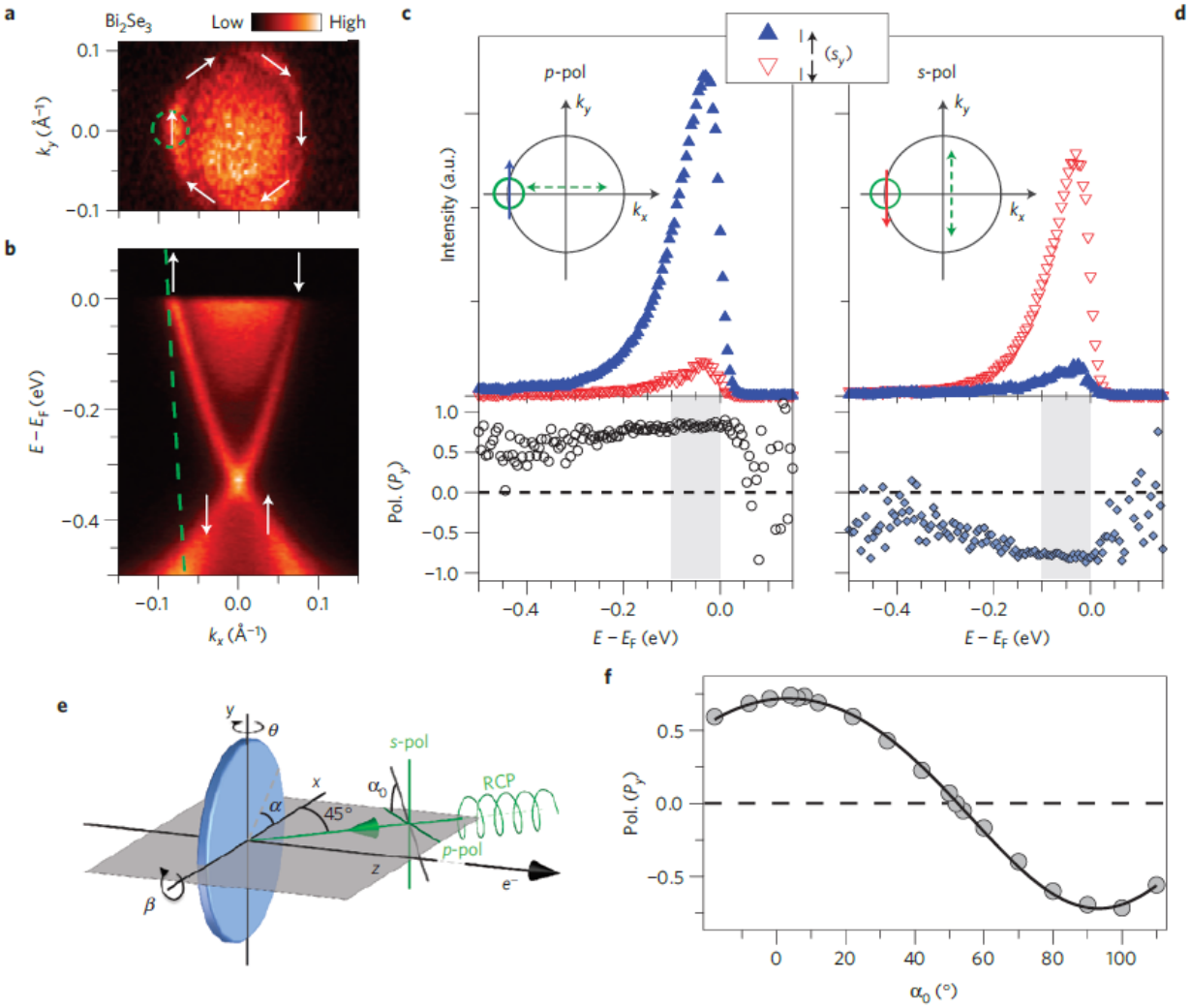

Figure 3.4. **ARPES on Bi_2Se_3 and tunable spin polarization. a,** Fermi surface and **b,** near E_F band structure measured with hν=35 eV. White arrows depict expected spin texture. Dashed green lines show momentum where spin-resolved measurements were made in **c,** with p-polarized photons and **d,** with s-polarized photons. **e,** Experimental geometry, including p-polarized, s-polarized, and right circularly polarized light. **f,** Spin polarization extracted from EDCs such as c and d as a function of photon polarization angle, α_0.

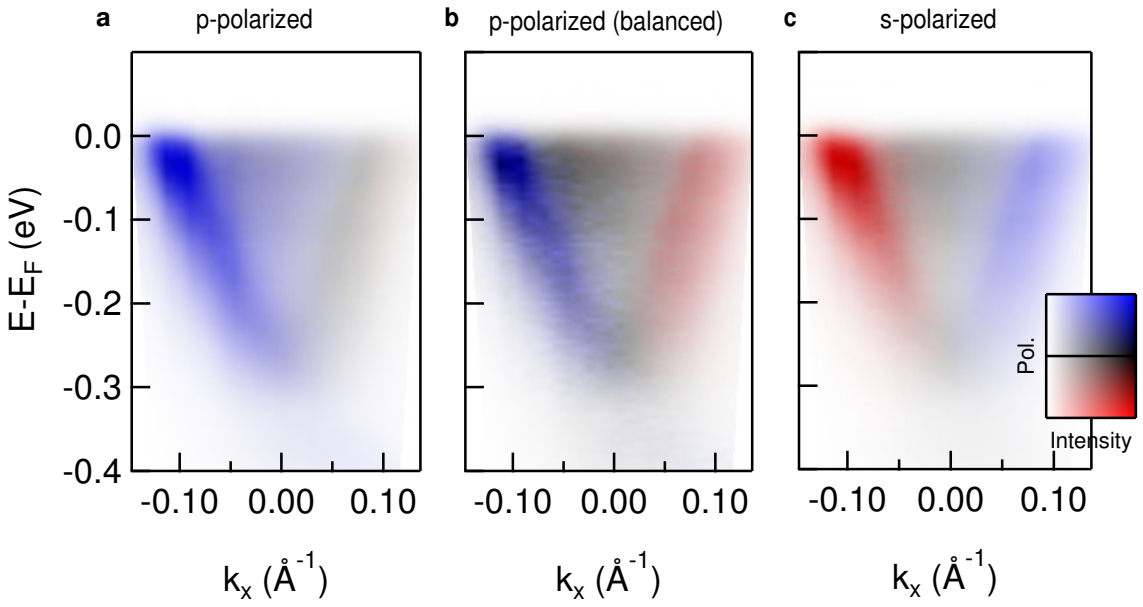

Figure 3.5. **Spin-resolved maps of TSS of Bi_2Se_3 .** Three maps of the topological surface state: **a,** taken with p-polarized light, **b,** same, but with intensity of spin-down electrons multiplied by three, and **c,** taken with s-polarized light.

cone, and consistent with 3.4c and previous works[37]. However, the right branch of the cone appears largely unpolarized: gray. Inside of the cone, intensity is seen for the conduction band up to the Fermi level, above which the white background indicates few counts.

For a spin texture that circles Γ, the right side of the cone would have been expected to have negative spins. A balanced cone with opposite spins on each side is achieved by multiplying the intensity in the spin-down channel by three. The resulting map is presented in 3.5b. This also causes the conduction band to now appear unpolarized, as is expected of a bulk band.

What we see, therefore is that p-polarized light causes an apparent background spin polarization: there are strong spin-dependent matrix elements (SMEs) favoring spin-up electrons. This sort of effect, discussed in chapter 2, is due to the strong spin-orbit coupling in the material and the geometry of the light polarization relative to the trajectory of photoelectrons traveling to the detector. Hence, even as the sample polar angle is rotated to scan momentum space, the SMEs do not change. The photoemission process causes the whole map to skew blue in a momentum-independent manner.

Such SMEs do not exist with s-polarized light in this geometry. Thus, Fig. 3.5c shows a map that is symmetric around Γ, but with opposite spins of the p-polarized measurements. The left branch is now spin-down and right branch is spin-up. Clearly, the apparent flipping of spins probed with s- versus p-polarized photons was not a peculiarity of the angle of the EDCs in 3.4, but is rather a feature of the TSS in Bi_2Se_3. The supposed spin-momentum locking must have some extra complexity. Does it have impacts on other components of spin?

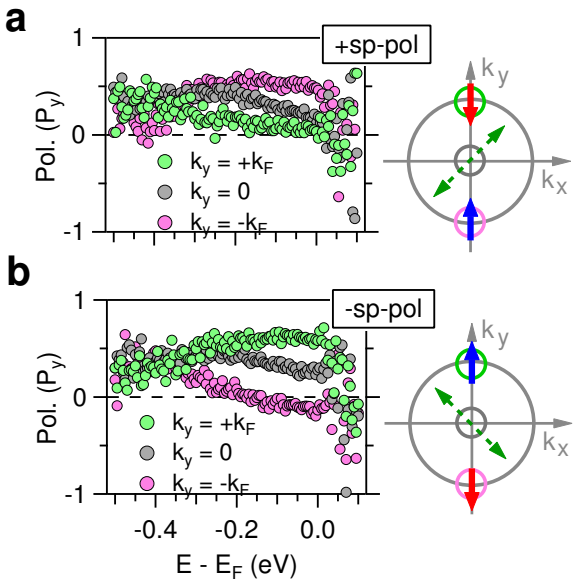

Figure 3.6. **Measurement of spins parallel to momentum. a,** Spin at $\pm k_y$ when probed with +sp-polarized light and **b,** with -sp-polarized light.

3.2.3 Full three dimensional control

Here, we domenstrate the extent of spin tunability in the TSS of Bi_2Se_3. Figures 3.6 and 3.7 show alternative experimental geometries and different components of measured spin. In 3.6, the sample's tilt angle (β in 3.4e) is rotated to access $\pm k_y$. Now, the spin component measured is parallel, rather than perpendicular to k. Note that the spin-TOF cannot measure horizontal in-plane components of spin, so it is only possible to achieve a measurement of this spin component by cutting along k_y.

As can be seen in 3.6a, when the probing light is polarized at α_0=45°(halfway between p-polarized and s-polarized), the TSS has a spin polarization along this direction. While this result contradicts the expectation that spin be locked perpendicular to momentum, it switches sign on the opposite side of the cone, suggesting that the spin has to do with physics of the initial state and is not an artifact of the particle angle measured. Note, however, that SMEs do give an overall offset to the spin polarization.

3.6b reverses the story: rotating the light polarization to α_0=-45° yields spins on both sides of the cone that are opposite to those measured with α_0=+45°. Once more, photoelectron spins can be flipped just by changing the polarization of light used.

Lastly, spins out of the plane of the sample can be generated using circularly polarized light. Fig. 3.7 shows cuts along k_x, as in 3.5c,d, but now the spin detector is rotated to be sensitive to out-of-plane spins. When the map is made with right circularly polarized photons, all of the photoelectron spins point into the sample surface. When the helicity is reversed to left circularly polarized (3.6d), all of the spins point out of the plane. In this way,

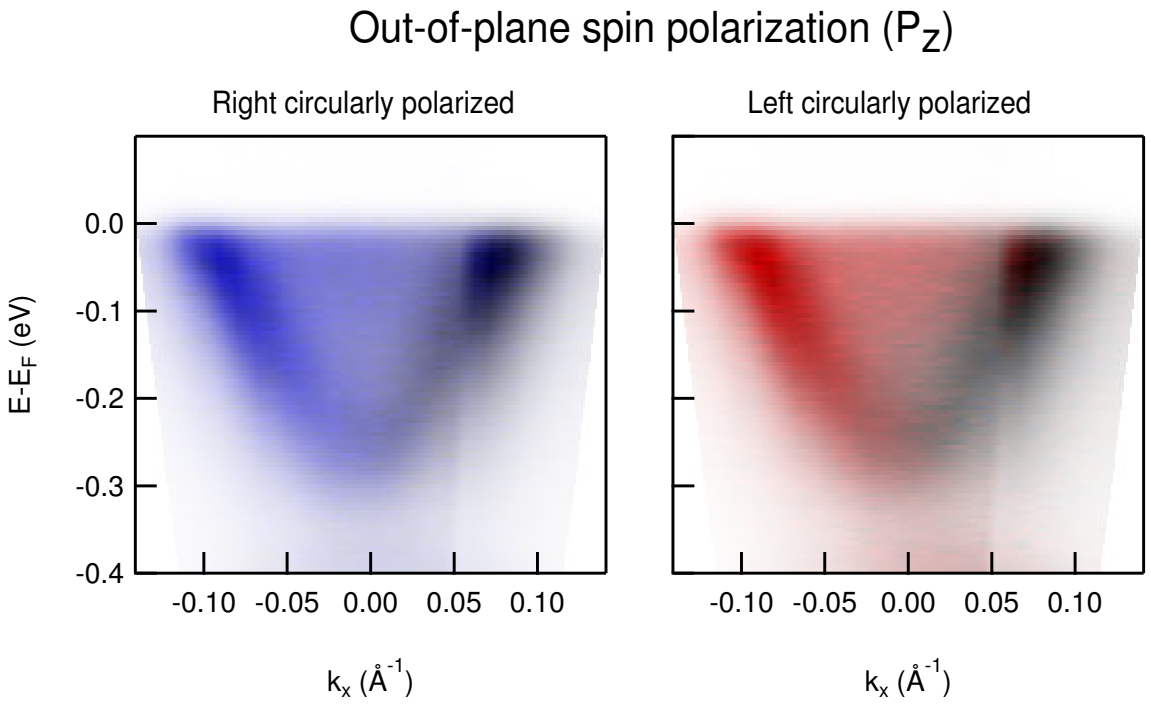

Figure 3.7. **Measurement of out-of-plane component of spin.** Maps along k_x with out-of-plane spin component measured. Measurements made with right and left circularly polarized light.

Bi_2Se_3 can produce photoelectrons with spins pointing in any arbitrary direction in three dimensions, with the spin direction dictated by photon polarization.

To explore where this surprising effect comes from, we can compare these results to measurements of the Rashba states on the (111) surface of Au, which also arise due to strong spin-orbit coupling.

3.2.4 Photon polarization-dependent measurement in Rashba surface states of Au(111)

The Au(111) surface states are frequently used for spin-ARPES measurements[129,132,136]. They are a prototypical Rashba system in which spin-orbit coupling and the loss of inversion symmetry at the surface result in a spin-splitting of the parabolic surface state and two concentric Fermi surface rings with opposite helical spin textures[2,11,186,13] as shown in Fig. 3.8.

The surface was prepared by evaporating Au on a clean W(110) substrate *in-situ* at room temperature and then annealed to ∼500° C, resulting in a well ordered Au(111) surface. Measurements were taken at a sample temperature of ∼20 K with pressures less than 7×10^{-11} torr throughout.

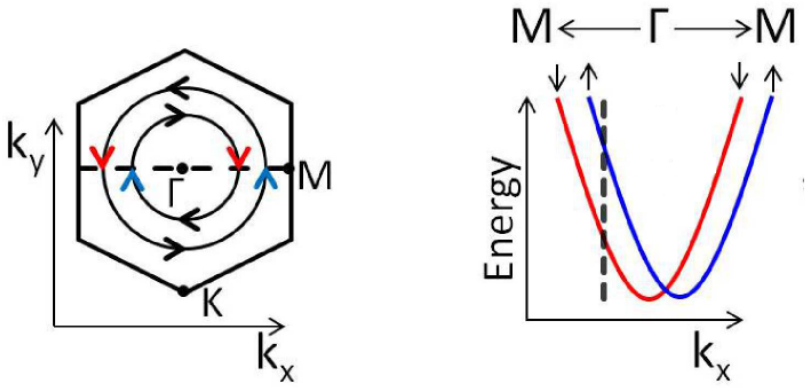

Figure 3.8. **Cartoon of Au(111) Fermi surface and Rashba bands.**

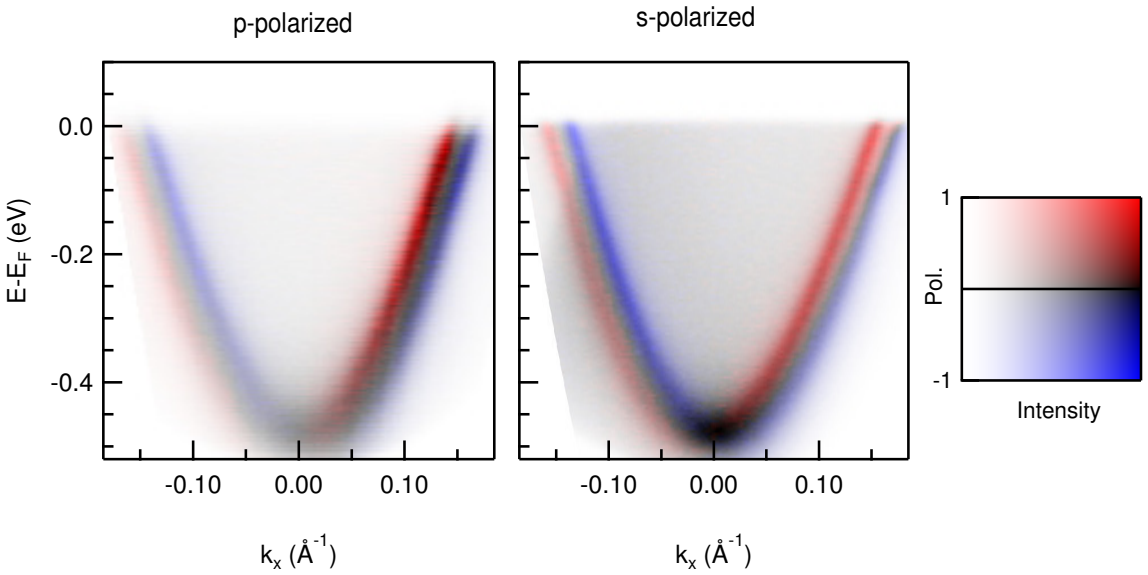

Figure 3.9. **Spin-resolved ARPES maps of Au(111).** Rashba states are seen as two spin-split bands. Equivalent measurements made with p-polarized and s-polarized light. At right, the two-dimensional colorscale is shown.

Fig 3.9 shwos full spin-resolved ARPES as a function of binding energy and momentum along the ΓM direction, indicated by the dotted line in the Fig. 3.8 Fermi surface diagram. The maps are made of data from 48 individual spin-resolved EDCs similar to Fig. 3.8b, taken sequentially in a total acquisition time of just 2 hours. The data are collected through momentum (angle) space by rotating the sample, here in 1° steps, and converted to k-space. The two spin-split parabolic bands of the Rashba system are clearly seen, with their expected spin characters, quantized along the k_y direction, as labeled[2,11,186,13].

As is readily evident, the same spin polarizations are seen with p-polarized and s-polarized light. In both cases, the spin-down parabolic band is shifted towards $-k_x$ while the spin-up band is shifted towards $+k_x$ Rotating the light polarization does not cause photoelectron spins to flip.

Note, however, that overall intensity in the p-polarized measurement increases with k_x. In the spin-TOF geometry, this corresponds to the sample being rotated farther away from the direction of normal incidence of light. The p-polarized light includes an increasingly large component in $\hat{z}$ perpendicular to the sample surface. Hence, there is stronger emission of electrons from p_z orbitals, which dominate the surface state. In contrast, the s-polarized measurement has consistent intensity through the range of k space measured. This matrix element effect is pertinent for understanding why spins do not seem to flip with photon polarization in these samples.

3.3 Spin flipping explained by spin-orbit interaction

Why do photoelectrons from Bi_2Se_3 point in a direction that depends on photon polarization whereas those from Au(111) seem not to? The apparent flipping of spins is actually revealing of the underlying way spin-orbit coupling shapes the surface states of Bi_2Se_3. The phenomenon has been described in two equivalent ways that account for the spin-orbit interaction either in the photoemission process or in the initial state wavefunction.

3.3.1 Photoemission process

The first description was given by Park *et al*[187] and further explained in the experimental context by Jozwiak *et al*[61]. In this description, the wavefunction of the topological surface state has a helical *pseudo*spin texture in momentum space. The photoemission process brings an electron from this initial to a final state at the detector in which it has a defined real spin. Modeling the interaction of light with electrons in the surface state must include a spin-orbit term that is not usually present in photoemission calculations. This term has the effect of connecting an initial pseudospin to different final state spins depending on the photon polarization used.

Figure 3.10 shows the calculated expected spin textures across the Fermi surface of Bi_2Se_3

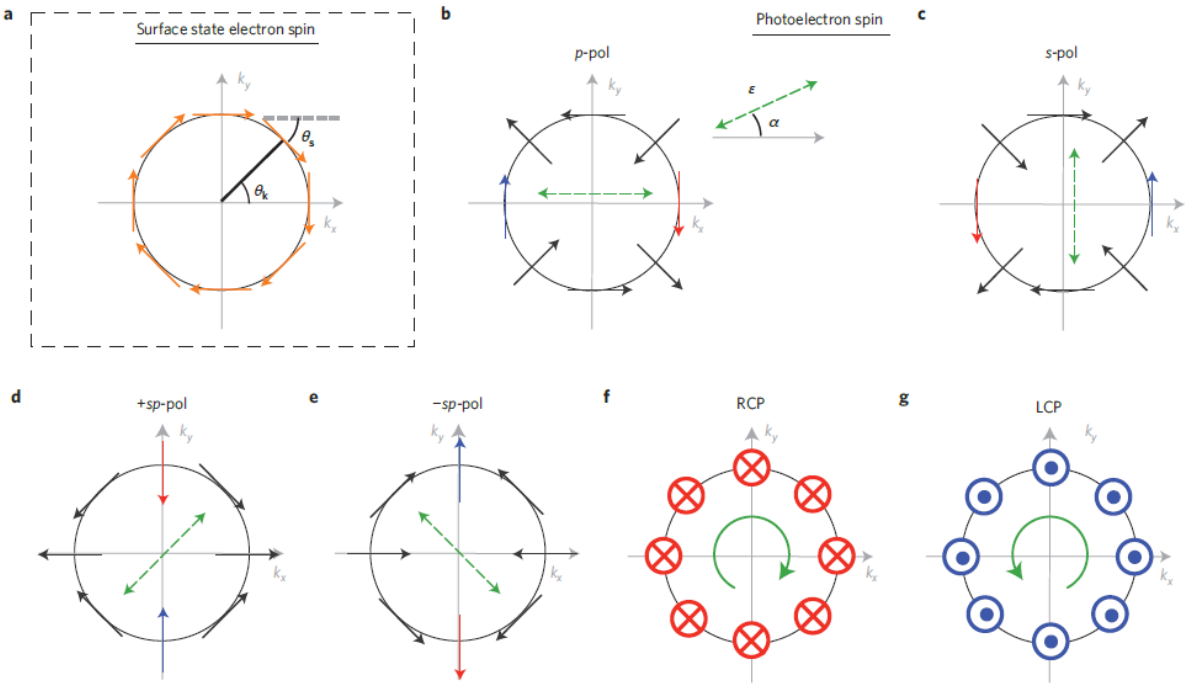

Figure 3.10. **Photoelectron spin texture from TSS with different photon polarizations. a,** Helical pseudospin texture of the TSS initial state, commonly thought of as the spin texture, around the Fermi surface of Bi_2Se_3. This will connect to distinct real spin textures after photoemission by **b-g,** different polarizations of light.

when probed with various photon polarizations. 3.10a shows the pseudospin texture circling the Γ point. This is often thought of as the actual spin texture of the TSS; however, in the strong spin-orbit coupling environment of the material, it cannot have a defined real spin texture. When a photoemission experiment is performed along a k_x cut using p-polarized photons (3.10a), the real spin final state matches the directions of the pseudospin initial state. With s-polarized photons, that pseudospin connects to oppositely pointed real spins along k_x. 3.10b-e are all the same Fermi surfaces rotated to different orientations, yielding photoelectron real spin components that were seen in the experiment.

3.3.2 Orbital dependent spin textures

An alternate description of the same physics could account for the spin-orbit coupling in the initial state wave funtion[188]. In that case, neither spin, **S**, nor orbital angular momentum, **L**, are conserved quantities: electrons in the surface state cannot be in an eigenstate of spin. Instead, this description considers the pseudospin texture to be total angular momentum, **J**. This picture will be used throughout the rest of the work as it more closely ties to familiar quantities in a wave function.

While the surface state is thought to derive from p_z orbitals, the spin-orbit interaction will mix in p_x and p_y components. The constraint on total angular momentum, however, forces each orbital component to couple to a distinct spin texture. The TSS, in fact, has three distinct real spin textures for three distinct orbital components.

This coupling of orbitals to spins stems from the symmetries of the surface state being probed. Near Γ, mirror symmetry of the zone center still applies. This experiment probed along the effective mirror plane perpendicular to the sample surface that cuts through $\hat{x}$. The p_y orbitals are normal to this plane and will thus have the opposite eigenvalue for the mirror operation than p_x and p_z orbitals, which are oriented within this plane. In order for the overall wave function, which has components of all three orbitals, to be an eigenstate of the mirror operation, the spin component of the wavefunction that couples to p_y orbitals must be opposite to that of p_x and p_z orbitals along this cut.

During the photoemission process, linearly polarized light will couple to orbitals oriented along the direction of light polarization. Hence, p-polarized light will photoemit p_x orbitals and p_z orbitals, the most dominant orbitals in the surface. Each of these couple to spins along k_x that match the pseudospin texture. However, s-polarized photons will exclusively couple to p_y orbitals, which are forced to couple to spins pointing opposite to those of p_x and p_z.

Photoemission is acting as a probe of the distinct orbital contributions to the surface state, and the spin detector is revealing the spin textures to which each orbital couples. In Bi_2Se_3, spin and orbital textures in momentum space are entangled with each other. Thanks to the strong spin-orbit coupling, one cannot speak of a surface state's spin texture, but rather of orbital-dependent spin textures. Spin-ARPES with tunable photon polarization is the tool to reveal spin-orbital textures, the full complexity of the surface state. Because the

Rashba states in quantum wells on Bi_2Se_3 are made up of the same orbitals, are subject to the same spin-orbit coupling, and are shaped by the same symmetries as the TSS, they show the same orbital-dependent spin textures.

3.3.3 Distinction between Bi_2Se_3 and Au(111)

So why did states in Bi_2Se_3 of both trivial and non-trivial origin behave differently than the spin-orbit-induced states on the surface of Au? The Au(111) Rashba states have the same symmetry near Γ as the TSS and are also composed of p orbitals. The answer must have to do with the mix of orbital components probed.

In fact, the key distinction is that the Au(111) surface state is much more strongly dominated by p_z orbitals. Calculations by Ryoo *et al* reveal that the in-plane p_x and p_y orbitals combine to make up 35% of the Bi_2Se_3 TSS but less than 2% of the Au(111) Rashba states[189]. A very slight component of p-polarized light mixed in with s-polarized light will cause the intensity of p_z orbitals to swamp that of p_y. Under realistic experimental conditions, this is likely to occur due to imperfect azimuthal orientation of a half wave plate or the introduction of a circular polarization component in a wave plate that is slightly off from perfectly "half wave" for the wavelength of light used. Hence, the measurements of the Au(111) surface states with both photon polarizations were dominated by the same p_z signal with the expected spin texture.

The surface states probed in Bi_2Se_3 demonstrate that spin-orbital entanglement comes from spin-orbit coupling. We could learn further how the interaction serves to orient spins in the Bi_2Se_3 surface state by probing spin-dependent dynamics of electrons out of equilibrium.

3.3.4 Pump-probe measurements of Bi_2Se_3

We present an initial study of how the spin populations behave out of equilibrium in Bi_2Se_3 . These results are meant to demonstrate what the technique is capable of and highlight hints of spin-dependent dynamics that will require further investigation.

The pump-probe technique can be used to study band structure that is unpopulated at equilibrium. Here we use a p-type Bi_2Se_3 sample that is doped with Mg to put the Fermi level in the bulk valence band. This allows us to study dynamics in the surface state and bulk conduction band that would be below E_F in typical Bi_2Se_3 samples[156].

Figure 3.11 shows maps of this band structure. Panel a is the sample in equilibrium: only the bulk valence band is populated. Panel e is a cartoon of the expected band structure with the well known topological surface states as well as the bulk conduction band above the Fermi level. The red and blue colors represent the positive and negative spin polarizations that would be expected from probing linear vertical (s-polarized) photons[61]. Photoemission detects these states after electrons are pumped into them. Panels b-d show spin-integrated maps symmetrized about the Γ point. Soon after pumping (b), the topological surface

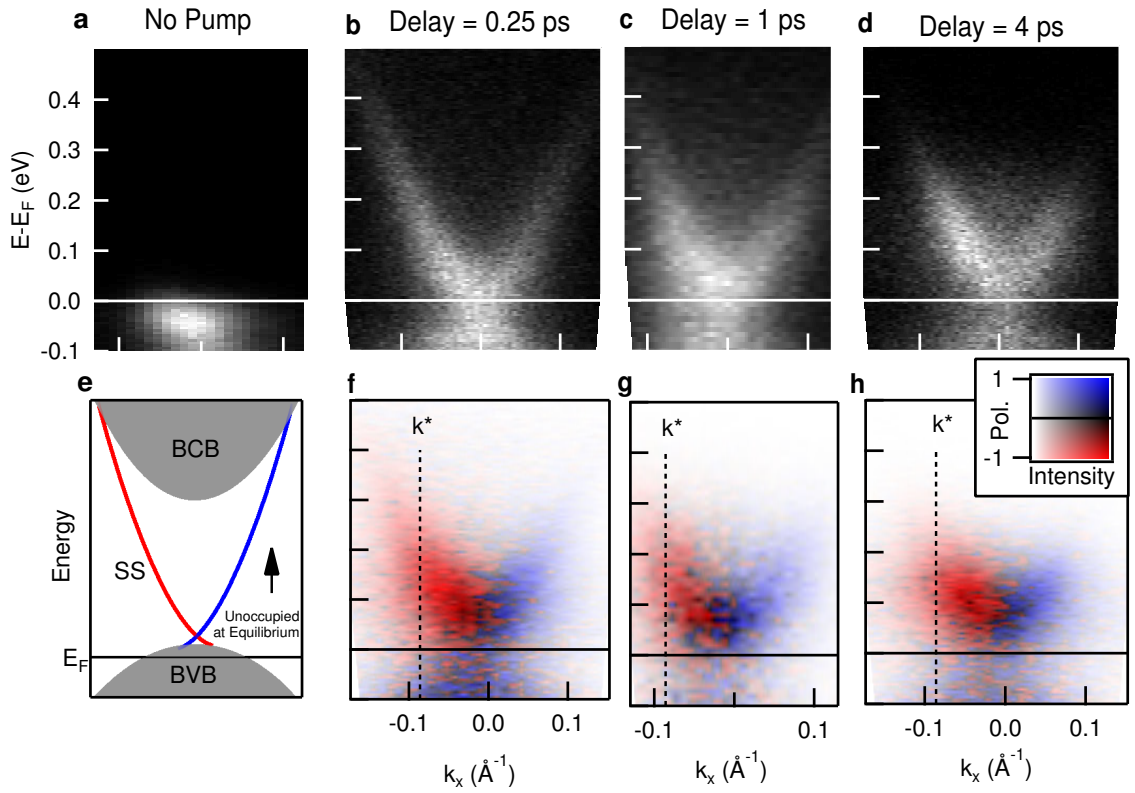

Figure 3.11.

Maps of the band structure of p-type Bi_2Se_3. a-d, Spin-integrated ARPES spectrum without pumping (a), showing only an occupied valence band, and taken at various delay times after optical excitation (b-d). **e,** Schematic of the sample's bandstrucure, with blue and red bands referring to expected positive and negative measured spin polarizations, respectively. **f-h,** Spin-resolved maps taken at the same delay times as b-d. Both are plotted with a colorscale in which darkness represents photoemission intensity, and color from red to blue represents spin polarization.

state is populated well above the Fermi level. Some decay of the highest energy electrons has occurred after 1 ps (c). After 4 ps (d), much of the excited population has moved down towards the equilibrium Fermi level, and electrons pool near the conduction band minimum. From there, they feed the surface state within the bulk bandgap, which remains populated[156]. These maps bear a strong resemblance to the equilibrium maps of n-type Bi_2Se_3 . Note, however, that sample quality issues lead to significantly broadened spectra from the p-type samples.

The key physics of these surface states lies with the spin degree of freedom, which is shown in 3.11f-g using a colorscale in which darkness signifies photoemission intensity, and color from red to blue represents spin polarization. These maps are composed of 30 EDCs each and were acquired with s-polarized probing photons. The spin component measured was in the plane of the sample and perpendicular to the cut through momentum space. The maps reveal a negatively polarized branch of the Dirac cone for negative momentum, and positive spin polarization for positive momentum. This is consistent with previous work using s-polarized photons to probe n-type Bi_2Se_3[61]: the spins are opposite what would be expected with p-polarized. Longer after excitation, the surface state remains polarized, while the electrons that have collected at the conduction band minimum are unpolarized. This, of course, is because the spin polarizations measure the actual spin character of the band; they are not transient spin imbalances introduced by pumping. While the Dirac cone of Bi_2Se_3 has been well studied, the pump-probe technique can be used to reveal spin textures above the Fermi level of materials that have not been previously characterized.

STARPES really demonstrates its power in tracking on the sub-picosecond timescale the spin-dependent decay of electronic populations driven out of equilibrium. Figure 3.12 shows a scan of pump-probe delay times for an EDC marked k* in 3.11f-g. For Delay<0, when the probe beam precedes the pump, only states below the Fermi level are occupied. Soon after excitation, a spin-polarized electronic population appears in the surface state $\approx$ 200 meV above the Fermi level. Higher up in energy, some counts are seen even in the conduction band up to $E - E_F$=400 meV. While these states depopulate within several picoseconds, the surface state still has significant population 12 ps after excitation by the pump pulse.

To extract quantitative information, the total intensity for spin-up and spin-down electrons can be integrated within the energy window of the surface state at this momentum: 120 meV$< E - E_F <$250 meV. 3.12b plots this intensity as a function of pump-probe delay, with spin-up and spin-down intensities each normalized to its maximum for ease in seeing the shapes of their decay. Visual inspection clearly shows a slightly slower decay of spin-up electrons, the minority spin character in this measurement. Fits to the decay after peak intensity yield decay constants of 1.75 ps for spin-down electrons and 1.91 ps for spin-up. 3.12c coroborates this, showing that the spin polarization becomes less negative over time, as spin-down electrons decay out of the band faster than spin-up electrons.

STARPES is unique in its sensitivity to spin-dependent decay times, providing insight into the distinct decay channels available to excited electrons of different spin character. The possible depolarization evinced by this delay scan could be as simple as a return to an unpolarized background of unpopulated states at equilibrium. If the surface state can be considered to have a constant spin polarization as long as it is populated, this is a strong

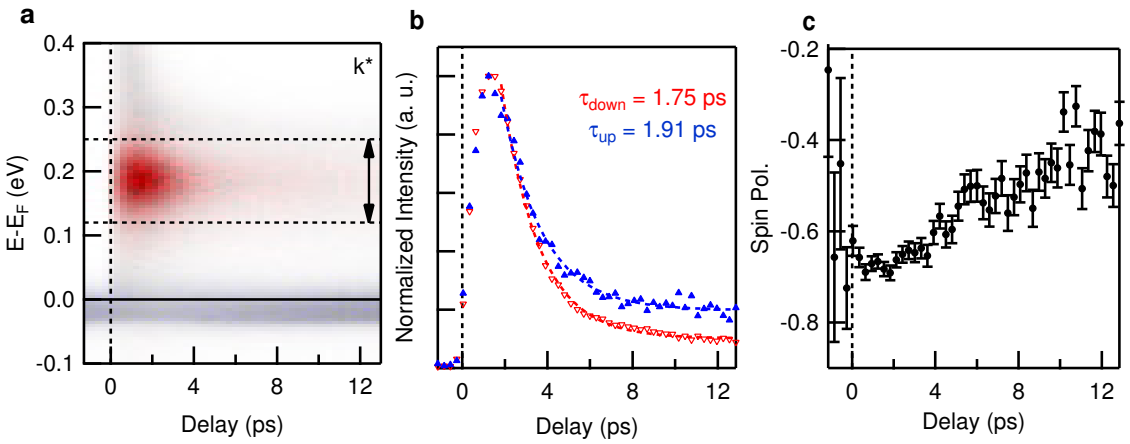

Figure 3.12.

Scan of pump-probe delays. **a,** Spin-resolved energy distribution curve as a function of time after excitation. This was acquired at an angle corresponding to the dotted line in 3.11e,f. **b,** Integrated intensity for spin-up and spin-down electrons within the energy window of the surface state marked in a by dashed lines. Each curve is normalized to its maximum. Decay time constants are extracted by a fit to exponential decay after the peak intensity. **c,** Spin polarization within the same energy window as a function of delay, with statistical error bars shown.

demonstration of the inherent spin texture of the state. In the Bi_2Se_3 cone, this might be no surprise, but in other normally unpopulated states, this can provide valuable insight[63].

On the other hand, one can imagine a few possible causes of spin-dependent realxation appearing in this measurement. To the extent that imperfect photon polarization alignment causes some p_z or p_x orbital components to be probed, the change in spin polarization may signal a shift in the relative proportion of orbital populations. Recall that the dominant p_x and p_z orbitals have the opposite spin character of the p_y orbitals seen in this measurement. Perhaps the relatively smaller population of spin-down electrons seeking to decay into the spin-degenerate bulk valence band could allow them to decay faster.

Alternatively, the EDC may include some contribution from the bulk conduction band, which might be fed a transient spin polarization from higher-lying edges of the surface state cone. The spin-up counts from the majority p_z orbitals might diminish the overall spin polarization measured.

In this way, there are scenarios in which the spin texture, the orbital texture, and the entanglement between the two may guide how out-of-equilibrium populations move between surface and bulk and return to equilibrium. They may provide an avenue for guiding desired electron and spin populations. To be sure, further study would be needed to understand the dynamics of Bi_2Se_3 . However, this experiment highlights the rich new types of physics that can be probed: how spin-orbit coupling shapes electron dynamics.

3.4 Conclusion

This chapter presented several measurements of Bi_2Se_3 as well as a prototypical Rashba surface state. From these, we learned that spin-orbit coupling will give surface states complex spin and orbital textures in momentum space. Moreover, these two textures can be entangled with each other in such a way that each orbital component has its own spin texture. The entanglement between these two crucial degrees of freedom may shape how the surface state behaves out-of-equilibrium, and we showed how STARPES will be uniquely able to probe such physics. However the consequences of this entanglement will be masked if a single orbital dominates the population, as in the case of Au(111).

Full understanding of the important and potentially useful features of surface states will mean characterizing how and when the orbital degree of freedom is coupled to spin. The nature of the entanglement between the two is set by relevant crystal symmetries and mix of orbitals. It would be valuable to test other systems where symmetries change in order to understand fully how spins are coupled to orbitals, and under what conditions one would expect a surface to have several distinct spin textures.

Chapter 4

Limits of Spin-Orbital Entanglement

4.1 Spin-orbital entanglement in surface states

As was shown in the previous chapter, the pseudospin described by commonly used models can actually correspond to several different momentum-dependent spin textures, each belonging to wavefunctions with distinct atomic orbital character. In states subject to spin-orbit coupling, in the atomic limit, spin and orbital angular momenta (**S** and **L**) are not good quantum numbers; total angular momentum **J** is instead the conserved quantity[188]. As in the last chapter, it has recently been observed that in topological surface states, the spin and orbital textures can be "entangled" such that, at a given momentum, there is a mix of orbitals that each have a distinct spin orientation[188,75,190,191]. Thus, to fully understand the wavefunction of these potentially useful states means characterizing the complex spin-orbital texture.

While deepening our understanding of spin-orbit surface states, the dependence of spin texture on wavefunction atomic orbital character can give rise to a rich array of physical phenomena. It causes photoelectron spins to point in a direction dependent on photon polarization, allowing for optical control of spin polarization[187,61]. In fact, the relative weight of $p_{x,y,z}$ orbitals, and hence spin texture of Bi_2Se_3, varies through the atomic layers containing the surface state wavefunction[190,76]. Thus, many distinct spin polarization patterns are possible as different photoemission geometries will be sensitive to the interference of varying contributions from different layers[190]. It has even been seen that in Bi/Cu(111), hybridization at large momentum can abruptly change the relative strength of different orbital components and thereby change the overall spin polarization of a surface band[192]. That orbitals have distinct spin textures even enabled a photoemission experiment to reveal the strength of spin-orbit coupling in spin-degenerate bands in Sr_2RuO_4[44]. Knowledge of how the spin and orbital degrees of freedom mix is key to interpreting experimental results from spin-orbit materials, as well as possibly utilizing them technologically.

To reveal this spin-orbital texture, access is needed to specific orbitals' contributions to the spin-dependent electronic structure. Previously, spin- and angle-resolved photoemission spectroscopy (spin-ARPES) with tunable photon polarization was shown to be uniquely capable of studying this. This effect was predicted based on symmetry arguments and a model Hamiltonian[187], and was further discussed microscopically in terms of the constituent atomic orbitals making up the band[188]. With total angular momentum as the conserved quantity, the $J_z = \pm\frac{1}{2}$ basis is used to describe the surface state near $\bar{\Gamma}$. Under this constraint, spin-orbit coupling gives each of the $p_{x,y,z}$ orbitals its own spin texture. Light will select p orbitals oriented along the direction of photon polarization according to the selection rules for the photoemission process[75].

An optically tunable spin texture was first studied in the topological surface state of Bi_2Se_3, in which the occupied surface state Dirac cone is near the Brillouin zone center and isotropic in momentum space. Previous discussion of this phenomenon therefore focused on strong spin-orbit coupling and the symmetries at the $\bar{\Gamma}$ point in Bi_2Se_3: time reversal, mirror, and C_3 rotational symmetry. Similar phenomena have been observed in Bi/Ag(111)[193], W(110)[194,195], and BiTeI[196]. Thus far, there have been no tests of how it evolves at high wavevector k as the symmetry changes, leaving open questions about the fundamental nature of coupling of orbital textures to distinct spin textures. While it is known that orbital components of a surface state can couple to distinct spins and that a band's overall spin texture can change as the relative strength of orbital components change, the rules that determine how a particular orbital couples to spin and how symmetry shapes this coupling across the Brillouin zone have never been clearly determined.

Antimony, a topologically non-trivial semimetal, provides an intriguing test case. The Sb(111) surface states have been investigated with ARPES and spin-ARPES, confirming the spin polarization due to strong spin-orbit coupling and nonzero Berry's phase[197,198,59,199,200,201]. While the (111) surface of Sb has the same symmetries as Bi_2Se_3, its surface states are distinct in their strong k dependence. They remain separate from the bulk states out to large $|k|$, allowing for a comparison of the spin-orbital texture near $\bar{\Gamma}$ to that in areas of reduced symmetry, where we will demonstrate that there are significant differences.

4.2 Experimental details

Single crystal Sb (Goodfellow Corp.) was cleaved in situ, exposing the (111) surface. It was kept at ≈80 K and inside ultrahigh vacuum of $\approx 5 \times 10^{-11}$ Torr. The sample was probed with 6 eV photons generated through fourth harmonic generation from a Ti:sapphire oscillator and examined with a high efficiency spin- and angle-resolved photoemission spectrometer[136,4]. Instrumental energy resolution was 15 meV and momentum resolution was ± 0.02 Å^{-1}.

The light arrives 45° from the direction of detected photoelectrons. As shown in Fig. 4.4a, the angle of the sample with respect to the analyzer (labeled θ) is rotated to scan emission angle, which corresponds to cutting along k_x. Measurements were made with both

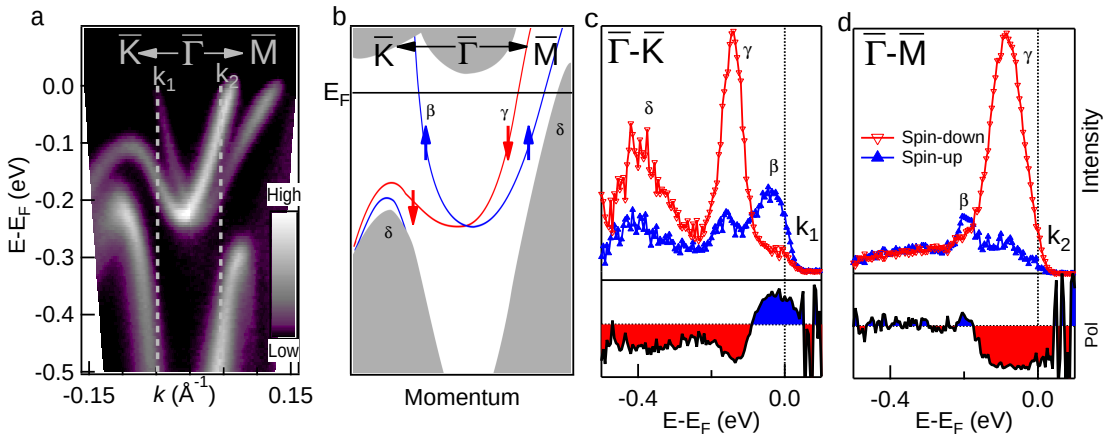

Figure 4.1. **The surface states of Sb(111), as measured with p-polarized (linear horizontal) light. a,** Spin-integrated ARPES map along $\bar{\Gamma}$-$\bar{\mathrm{K}}$ ($-k_x$) and $\bar{\Gamma}$-$\bar{\mathrm{M}}$ ($+k_x$) directions. **b,** Schematic of the surface states, color-coded to indicate spin polarizations measured previously[59]. Blue indicates $P_y > 0$, as defined in 4.3 a,d, and red indicates $P_y < 0$. **c,d,** Representative spin-resolved energy distribution curves (EDCs) taken at momenta shown in a. The spin-polarization, defined as $P_y = (I_\uparrow - I_\downarrow)/(I_\uparrow + I_\downarrow)$, is shown below corresponding EDCs.

s-polarized (linear vertical, $\hat{\epsilon}$ entirely in the sample plane) and p-polarized photons (linear horizontal, $\hat{\epsilon}$ includes an out-of-plane component). In this work, the spin polarization was always measured along $\hat{y}$, the component of spin that is allowed by symmetry along mirror planes. It is worth noting, however, that when experiments are performed with light that is polarized at an angle between s- and p-polarized, finite P_x and P_z spin polarizations are allowed and can yield information about the interference between $+\mathrm{P}_y$ and $-\mathrm{P}_y$ components of the wavefunction[202].

4.3 Spin-Resolved ARPES Results

A spin-integrated ARPES map along $\bar{\Gamma}$-$\bar{\mathrm{K}}$ and $\bar{\Gamma}$-$\bar{\mathrm{M}}$ high-symmetry directions is shown in Fig. 4.1a alongside a schematic (Fig. 4.1b) of the bands indicating the spin texture measured previously,[198,59] that of the dominant p_z orbitals. This work will show that this is part of a larger, more complex spin texture. We will use this finding to demonstrate rules governing the coupling of spins to orbitals. Along $\bar{\Gamma}$-$\bar{\mathrm{M}}$, two surface bands cross the Fermi level near $\bar{\Gamma}$. However, along $\bar{\Gamma}$-$\bar{\mathrm{K}}$, the lower one bends back down towards the bulk valence band rather than cross E_F. Spin-resolved EDCs measured with p-polarized light at two momenta (Fig. 4.1c,d) corroborate this picture. The lower band appears red for $k_x < 0$, indicating $P_y < 0$, while the upper band is blue, indicating $P_y > 0$ on that side of the Brillouin zone.

4.3.1 Photon polarization dependence

Figure 4.2 shows spin-resolved EDCs at select momenta along cuts through both high symmetry directions. By following the maximum peak positions (marked as β, γ, δ,), the spin characters of the bulk valence band and the two surface bands are resolved. Panels b and e show stacks of spin-resolved EDCs along $\bar{\Gamma}$-$\bar{\mathrm{M}}$ and $\bar{\Gamma}$-$\bar{\mathrm{K}}$, respectively. The corresponding spin polarizations for the two high symmetry directions are shown in panels c and f. The intensity peak is primarily spin-up (blue) for the surface band β while it is primarily spin-down (red) for the surface band γ. At the outer Fermi level crossings along $\bar{\Gamma}$-$\bar{\mathrm{M}}$, the absolute value of the spin polarization for both surface state bands is greater than 60% (-67% for γ in k_1 and +65% for β in k_6). As the $\bar{\Gamma}$ point is approached along $\bar{\Gamma}$-$\bar{\mathrm{M}}$, the spin polarization decreases to -47% for γ in k_3 and +34% for β in k_4. Intriguingly, the bulk valence band (δ) shows a small spin polarization of +12% in k_1.

Surprisingly, when the experiment is performed with s-polarized photons, as shown in Figure 4.3, we observe an overall reversal of the spin polarization near the $\bar{\Gamma}$ point. The β band now shows a negative spin polarization while γ shows a positive polarization. Along $\bar{\Gamma}$-$\bar{\mathrm{M}}$, γ now has a polarization of +25% at k_1: somewhat weaker in magnitude than what was measured with p-polarized light, perahps due to imperfect light polarization. We believe that, as was the case for Bi_2Se_3[61], this spin reversal is a manifestation of strong spin-orbital entanglement. Specifically, p_x, p_y, and p_z orbitals couple to different spin textures and are each probed by different polarization components of light. Interestingly, we observe that far from the $\bar{\Gamma}$ point along $\bar{\Gamma}$-$\bar{\mathrm{K}}$, the spin polarization does not reverse upon rotation of light. This is seen in comparing spectra at k_1, k_2, k_5, and k_6 along $\bar{\Gamma}$-$\bar{\mathrm{K}}$ betwen Fig. 4.2 and 4.3.

4.3.2 Momentum dependence

Figure 4.4 shows the full spin-resolved energy maps for both spin-up and spin-down electrons along $\bar{\Gamma}$-$\bar{\mathrm{M}}$ and $\bar{\Gamma}$-$\bar{\mathrm{K}}$ for both light polarizations. The maps are obtained by combining thirty EDCs and are shown with a colorscale in which brightness (from light to dark) corresponds to total photoemission intensity while color (from red to blue) corresponds to spin polarization. These two-dimensional colorscales are scaled nonlinearly in order to clearly resolve each band.

Beginning with the $\bar{\Gamma}$-$\bar{\mathrm{M}}$ direction, the data taken with p-polarized light (Fig. 4.4a) match the cartoon of Fig. 4.1b and previous measurements[198,59]. The $\bar{\Gamma}$ point is enclosed within an electron pocket with positive spin polarization for $-k_x$ and negative spin polarization for $+k_x$. The two branches of the surface state meet at $\bar{\Gamma}$ and bend back up to the Fermi level. Note that with p-polarized light, the stronger photoemission matrix elements for the spin-down branch (also apparent in 4.1c,d and 4.2), which can be strongly affected by experimental geometry[203], yield a net negative measured spin polarization at the $\bar{\Gamma}$ point.

However, when the same map is made with s-polarized light (Fig. 4.4b), both surface bands show the opposite spin polarization. The upper electron pocket encloses $\bar{\Gamma}$ with spin-down electrons at $-k_x$ and spin-up at $+k_x$. The lower branches also fully reverse their spins

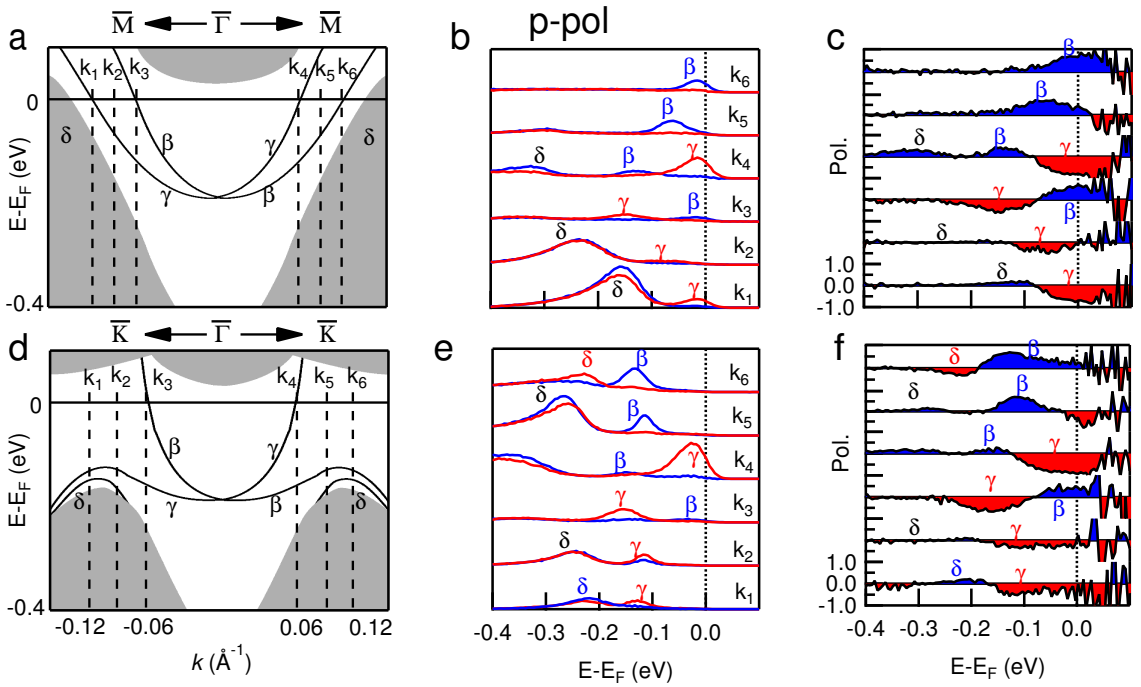

Figure 4.2. **Spin-Resolved measurements with p-polarized light a,** Schematic of band structure along $\bar{\Gamma}$-$\bar{\mathrm{M}}$ with positions of measurements marked by dashed lines. **b,** Spin-resolved EDCs at momenta marked in a. Peaks are marked corresponding to bands in a. **c,** Spin-polarization corresponding to EDCs in b. **d-f** Same as a-c but along the $\bar{\Gamma}$-$\bar{\mathrm{K}}$ direction.

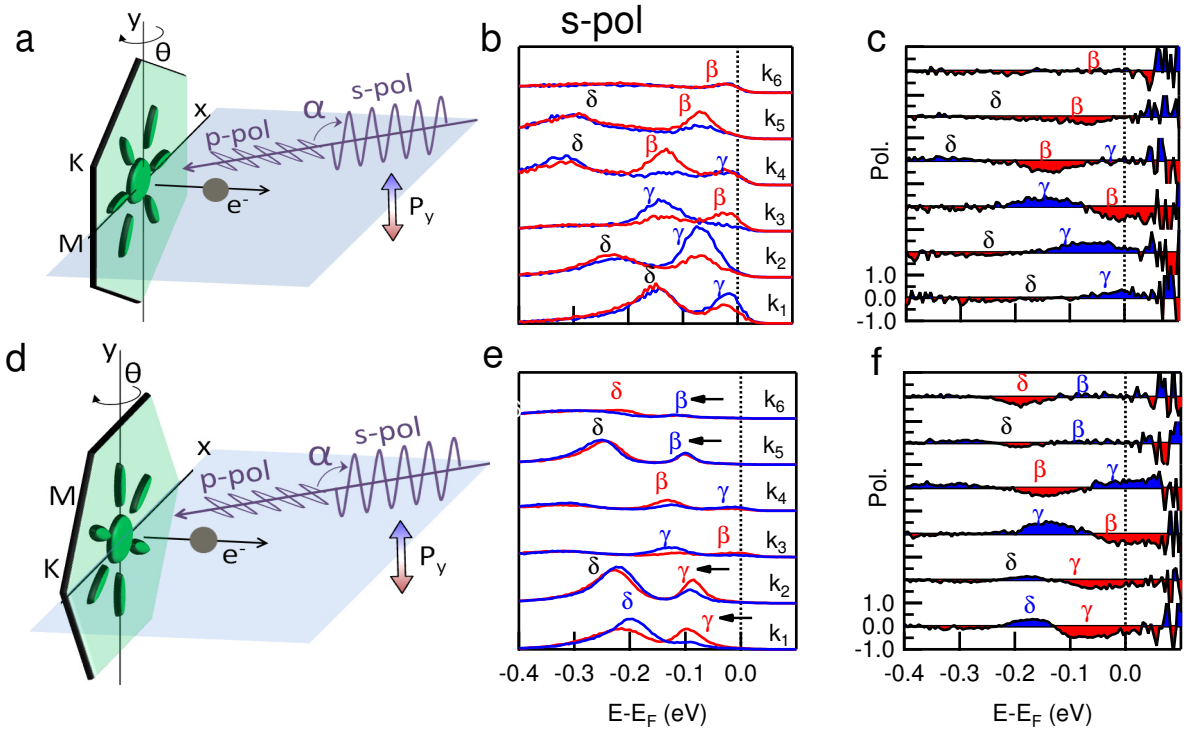

Figure 4.3. **Spin-Resolved measurements with s-polarized light. a,** Experimental geometry for measurement along $\bar{\Gamma}$-$\bar{\mathrm{M}}$. The angle α of photon polarization can be rotated from p-polarized to s-polarized. **b,** Spin-resolved EDCs at momenta marked in a. Peaks are marked corresponding to bands in a. **c,** Spin-polarization corresponding to EDCs in b. **d-f** Same as a-c but along the $\bar{\Gamma}$-$\bar{\mathrm{K}}$ direction. In e, arrows mark the peaks that are not reversed relative to Fig. 4.2 with p-polarized light.

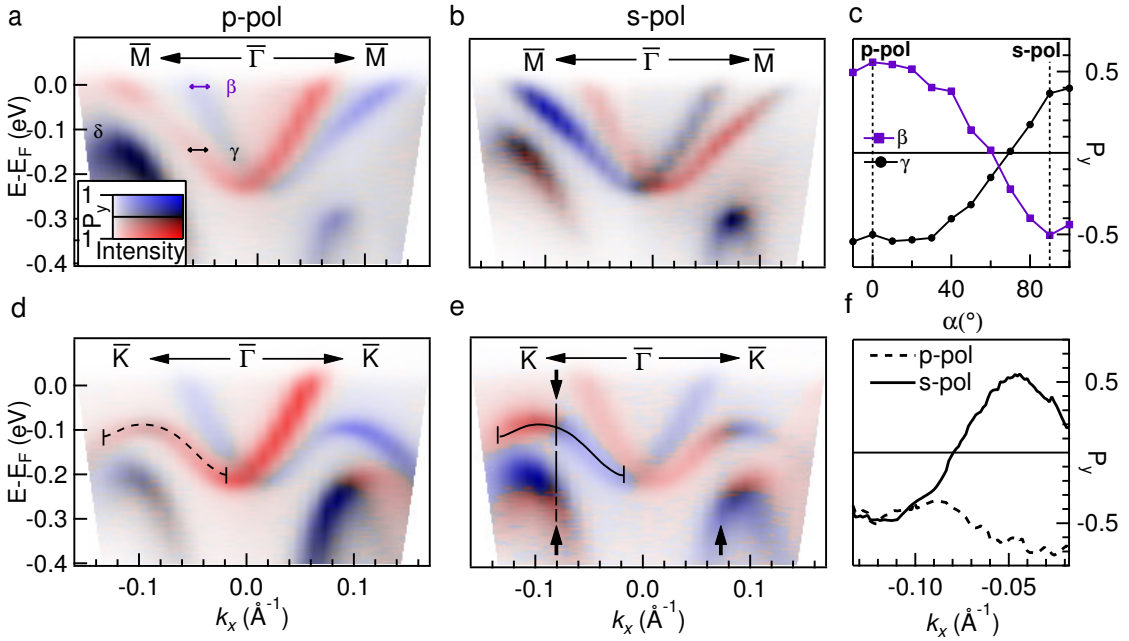

Figure 4.4. **Spin-resolved maps of $\bar{\Gamma}$-$\bar{\mathrm{M}}$ and $\bar{\Gamma}$-$\bar{\mathrm{K}}$ direction of Sb(111). a,b** Spin-resolved maps of the $\bar{\Gamma}$-$\bar{\mathrm{M}}$ direction, taken with p-polarized (a) and s-polarized (b) light. The two-dimensional colorscale displays the total photoelectron intensity by relative darkness and the spin polarization by the balance of red and blue. **c,** Spin polarization of the two surface bands as a function of photon polarization angle. The bands are labeled in a, and spin polarizations were extracted at a fixed k, as indicated by the small regions marked with arrows. **d,e** Similar to a,b but with sample azimuth rotated to cut along $\bar{\Gamma}$-$\bar{\mathrm{K}}$. **f,** Spin polarization along the left branch of the lower band, as measured with both p- and s-polarized light. The stretch of k space plotted here is indicated by dispersive lines in d,e.

at all momenta from $\bar{\Gamma}$ to $k_x \approx \pm 0.13\text{Å}^{-1}$, when they cross E_F. Furthermore, as in Bi_2Se_3, the spin polarization can be adjusted continuously, as shown in Fig. 4.4c, by rotating the angle of linear photon polarization, effectively selecting the orientation of p orbitals being photoemitted.

The $\bar{\Gamma}$-$\bar{\text{K}}$ direction (Fig. 4.4d-f) demonstrates a strong contrast. The same spin dependence on photon polarization is seen near $\bar{\Gamma}$. P-polarized light, selecting p_x and p_z orbitals, shows the electron pocket enclosing $\bar{\Gamma}$ having $+P_y$ at $-k_x$ and $-P_y$ at $+k_x$. S-polarized light reveals the opposite spin polarizations for p_y orbitals near $\bar{\Gamma}$.

However, near $k_x \approx \pm 0.08\text{Å}^{-1}$, this behavior ceases, and for larger $|k|$, s-polarized light yields the same spin polarization as p-polarized in the lower surface band. This abrupt end to p_y having opposite spin of p_x and p_z orbitals is highlighted in Fig. 4.4f, showing rapid reversal of the spin polarization measured with s-polarized light in a fairly small range of k along the left half of the band dispersion. Along the same dispersion, p-polarized light yielded a constantly negative spin polarization. At high k, all orbitals in this band show $-P_y$ at $-k_x$ and $+P_y$ at $+k_x$ regardless of the photon polarization used. Such a transition cannot be captured by previously used two-band models[187,188], but is consistent with predictions made about photoemission from Bi_2Se_3[189] and the photon polarization-independent spin textures measured in its lower Dirac cone[191].

Besides the rapid change in spin texture of the lower surface band, an unusual spin polarization appears around the top of the bulk continuum to the left of the dashed line and arrows in Fig. 4.4g. In particular, the part of the valence band closest in energy to the surface band shows the opposite spin of the surface band: $+P_y$ at $-k_x$ and $-P_y$ at $+k_x$. Normally in the bulk limit of an inversion-symmetric, non-magnetic crystal, each state is spin-degenerate. Thus, these results are indicative of surface effects creating new surface states in addition to the topological surface states[201].

It is seen for the first time that the locking of orbital textures to distinct spin textures can be strongly momentum-dependent. It can change rapidly as the surface band mixes with other nearby bands, yielding similarly oriented spins for all p orbitals. On the other hand, symmetry requires the spin and orbital degrees of freedom to remain tied to each other along the mirror plane in k space.

4.4 *Ab initio* tight-binding calculations

To understand these findings, an *ab initio* tight-binding simulation was performed[190]. The basis is chosen to be the Sb p orbitals, and the hopping parameters and on-site energies for the surface and bulk regions were extracted from first-principles calculations within density functional theory (DFT) using the Quantum Espresso package[204]. Norm-conserving pseudopotentials with the local density approximation by Perdew-Zunger[205] were used for Sb in both scalar- and fully-relativistic forms. DFT calculations for periodic bulk and a 12-bilayer slab were performed to obtain the hopping parameters within the atomic orbital basis by Wannier90 code[206]. The 12-bilayer slab and the bulk DFT calculations are performed

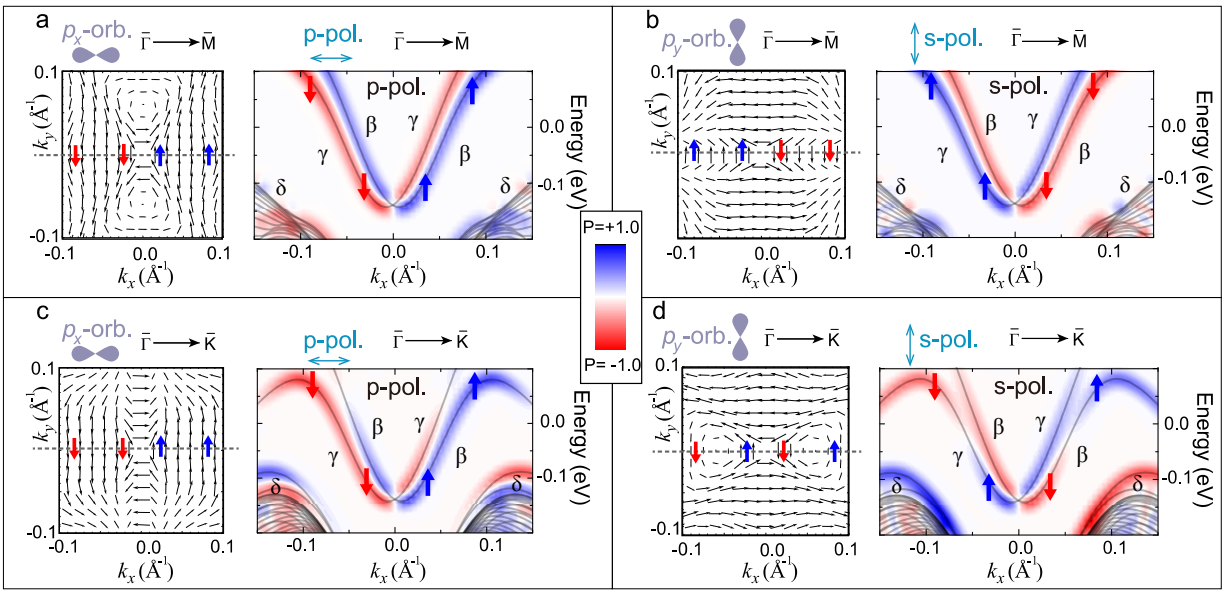

Figure 4.5. **Calculated spin-orbital textures and simulated spin-ARPES plots. a,** Left panel: spin texture of p_x orbitals in the lower surface band, with $\hat{x}$ (horizontal dashed line) oriented along $\bar{\Gamma}$-$\bar{M}$. These states can be photoemitted by p-polarized light. The black vectors are in-plane expectation values $\langle S_{x,y}\rangle$. Right panel: simulated spin-ARPES measurement along $\bar{\Gamma}$-$\bar{M}$ using p-polarized light. Spin polarization of the p_x component of the bands is shown by the color from blue to red, while the band energies are indicated by gray lines. The spin polarization of the lower band (with arrows) is asspin-orbit couplingiated with the spin texture in the left panel. **b,** Left panel: spin texture of p_y orbitals in the lower surface band, with $\hat{x}$ oriented along $\bar{\Gamma}$-$\bar{M}$. These states can be photoemitted by s-polarized light. Right panel: simulated spin-ARPES measurement along $\bar{\Gamma}$-$\bar{M}$ using s-polarized light. **c,d,** Same as a,b, but now with $\hat{x}$ oriented along $\bar{\Gamma}$-$\bar{K}$ and therefore the simulated measurements along $\bar{\Gamma}$-$\bar{K}$. Note that in the lower band, the orbital dependence of the spin texture ceases at large $|k|$ for $\bar{\Gamma}$-$\bar{K}$ but remains in $\bar{\Gamma}$-$\bar{M}$, consistent with experimental results.

to extract the parameters for surface and bulk, respectively. In the tight-binding model, we separate the slab into top and bottom halves, and repeat the bulk unit cell in between to fill the two halves. The onsite energies in the bulk region are adjusted to match the middle layers in the 12-bilayer slab. Eventually a 90-bilayer slab is constructed. All the physical quantities such as band structures, spin textures, orbital projections and photoemission predictions are calculated from this tight-binding model following the method in Ref.[190]. In the tight-binding model, the spin-orbit coupling strength can be tuned by weighting the hopping parameters between those extracted from scalar- and fully-relativistic DFT calculations.

4.4.1 Calculated orbital-dependent spin texture

Fig. 4.5 shows the calculated p orbital-dependent spin textures and the simulated spin-ARPES results. The simulated spin measurements utilize the optical selection rule for the dominant p to s transitions, namely, that photons linearly polarized along the i-direction ($i = x, y, z$) will only allow a p_i to s transition (if spin-orbit effects in the light-matter interaction are neglected). Although the final states reached in the photoemission process can shape the measured spin polarization[207], the s-wave final states reached in this 6 eV experiment should accept any spin, yielding information about the initial state being probed. Our simulations included p_y orbitals, as probed by s-polarized light, and p_x orbitals, as probed by the x-component of p-polarized light. While p_z orbitals also contributed to the measurements with p-polarized light, their spins match those of p_x orbitals along the directions measured, allowing us to focus on a comparison of p_x and p_y only.

In Fig. 4.5, it is clear that in the vicinity of $\bar{\Gamma}$, the spin textures of the lower surface band are the same as those predicted for the Dirac cone in Bi_2Se_3 [187,188,190], with p_y orbitals having opposite spin of p_x. However, when moving far enough away from $\bar{\Gamma}$ along the $\bar{\Gamma}$-$\bar{\mathrm{K}}$ direction, the spin polarization of p_y orbitals matches that of p_x. We note that the calculations of the upper surface band reveal a similar end to the p orbital dependence of the spin orientation, albeit once the band is above the Fermi level in measurements. In contrast, the spin of p_y orbitals along $\bar{\Gamma}$-$\bar{\mathrm{M}}$ remains fixed opposite to p_x orbitals for all k.

The simulation of Fig. 4.5c,d shows another important aspect of the experiment: the apparent spin polarization around the top of the valence band as the surface state dispersion bends down towards it. From $\bar{\Gamma}$ to $\bar{\mathrm{K}}$, as is evident by the spin polarization, around $|k| = 0.06\mathring{A}^{-1}$ the lower surface band is decoupling from the upper surface band, and starts to pair with another surface state band that is closer in energy to the bulk valence continuum. Therefore, the experimentally observed spin polarization around the valence band top and below the topological surface bands should be attributed to this newly emerged surface band.

4.4.2 Orbital texture with and without spin-orbit coupling

The results from Sb(111) indicate that the p orbital dependence of the spin texture breaks down as band mixing alters the basis states for the surface state wavefunction. This is highlighted by tuning the strength of spin-orbit coupling, α, in the tight-binding Hamitonian with $H_\alpha = H_0 + \alpha\Delta H_{spin-orbitcoupling}$, where $\Delta H_{spin-orbitcoupling} = H - H_0$, and H is the Hamiltonian with full spin-orbit coupling, and H_0 without spin-orbit coupling but with scalar relativistic effects. In addition to shrinking the bandgap, reducing α reduces the splitting between coupled bands, affording a clearer picture of which states are paired, meaning that they would be degenerate at each k without spin-orbit coupling ($\alpha = 0$). Fig. 4.6 shows the band structure with varying values of α. Violet is used to highlight the paired surface states. As shown in Fig. 4.6b, along the $\bar{\Gamma}$-$\bar{\mathrm{K}}$ direction, the lower topological surface band clearly couples with the upper topological surface band around the zone center. However, farther from $\bar{\Gamma}$, the two switch partners: the upper one runs into the conduction band continuum,

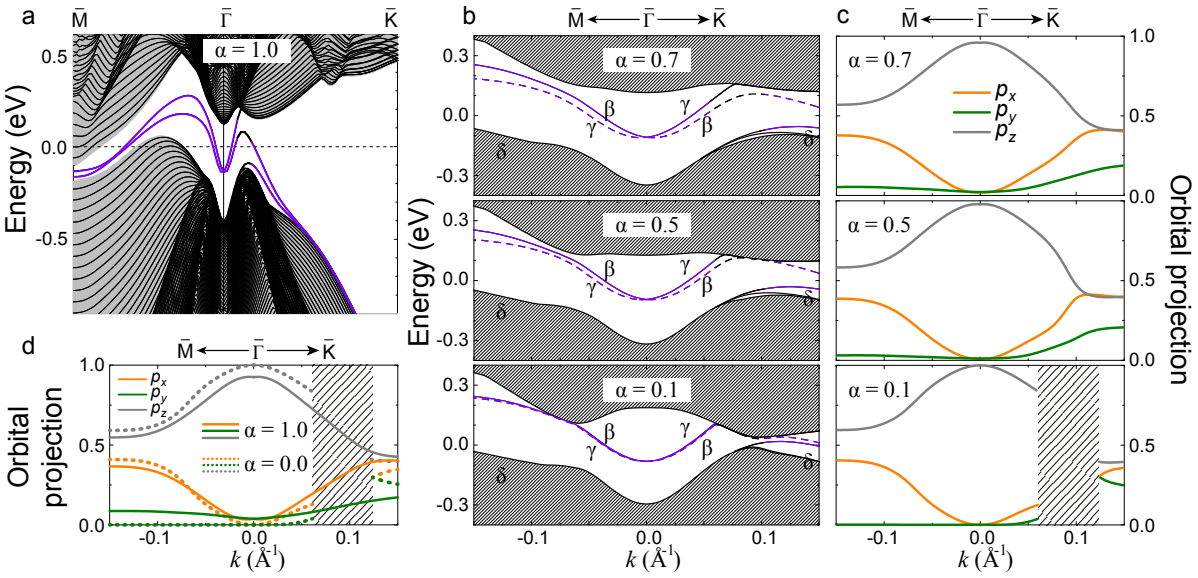

Figure 4.6. **Band structure evolution with spin-orbit coupling strength (α).** **a,** Calculated 90-bilayer Sb band structures with full spin-orbit coupling ($\alpha = 1$). The darkly shaded area is the projection of bulk states onto the surface Brillouin zone. The violet color indicates the surface states that would be degenerate in the absence of spin-orbit coupling ($\alpha = 0$). **b,** Detailed band structures along two directions ($\bar{\text{M}}$-$\bar{\Gamma}$-$\bar{\text{K}}$), with different spin-orbit coupling strength α. Along $\bar{\Gamma}$-$\bar{\text{M}}$, the two surface bands always couple to each other and stay within the gap; along $\bar{\Gamma}$-$\bar{\text{K}}$, the lower surface band couples to the upper surface band near $k = 0$, then switches to a new surface band closer to the valence bulk continuum at larger $|k|$. **c,** Projected p orbital character at various spin-orbit coupling strengths along the lower topological surface band indicated by dashed lines in b. A rapid change in the orbital character is seen along the $\bar{\Gamma}$-$\bar{\text{K}}$ direction. **d,** Similar to c, showing the two limits of full spin-orbit coupling ($\alpha = 1$, solid lines) and no spin-orbit coupling ($\alpha = 0$, dotted lines), respectively. Note that along $\bar{\Gamma}$-$\bar{\text{K}}$, all orbitals have a finite projection even in the absence of spin-orbit coupling, whereas along $\bar{\Gamma}$-$\bar{\text{M}}$, p_y is finite only with spin-orbit coupling. The missing parts of the curves in the $0.06 < k < 0.12$ range (shaded area) shown in c,d in the small α cases represent the fact that the band of interest disperses into the bulk continuum, as can be seen in b.

and the other couples with a new surface state band which emerges above the bulk valence band. These two eventually disperse together into the bulk valence band continuum, as clearly shown in Fig. 4.6a with full spin-orbit effects considered. In contrast, along $\bar{\Gamma}$-$\bar{\mathrm{M}}$ (Fig. 4.6b), the two surface states of interest are always coupled to each other and remain within the gap, maintaining the p orbital dependence of their spins.

The surface bands appear in pairs at any individual k point due to the degeneracy when spin-orbit coupling is completely turned off. The presence of spin-orbit coupling will split the degenerate bands, highlighting the fact that each of the single surface bands connects the valence and conduction bulk continuum, a result of the topologically non-trivial nature of Sb.

In Sb, as in Bi_2Se_3, the electronic states around the Fermi level are dominated by $p_{x,y,z}$ orbitals, which can take on $S_z = \pm\frac{1}{2}$. In the topological surface states near $\bar{\Gamma}$, $\mathbf{L}$ and $\mathbf{S}$ are coupled in such a way that $J_z = \pm\frac{1}{2}$ [188,187]. As shown in Fig. 4.6d, in the absence of spin-orbit coupling, at $\bar{\Gamma}$ there is only p_z character, i.e. the orbital projection is zero for p_x and p_y. An eigenstate of J_z will remain such even with $\mathbf{L} \cdot \mathbf{S}$ turned on. Thus, spin-orbit coupling will mix in $p_{x,y}$ orbitals, giving them a finite projection in 4.6c,d, while keeping $J_z = \pm\frac{1}{2}$ dominant in the vicinity of $\bar{\Gamma}$. This means that in this region, the states can be described sufficiently by a two-band model [187,188]. The $J_z = \pm\frac{1}{2}$ requirement determines the spin texture that each p orbital must have. In other words, for in-plane orbitals $|p_\pm\rangle = \frac{1}{\sqrt{2}}(\mp|p_x\rangle - i|p_y\rangle)$, with angular momentum $L_z = \pm 1$, the surface state can be constructed from two basis states, $|p_+, \downarrow\rangle$ and $|p_-, \uparrow\rangle$, carrying $J_z = \pm\frac{1}{2}$. Such states will always show a p orbital-dependent spin texture, meaning opposite spins will be measured with s-polarized and p-polarized light.

Symmetry provides similar constraints along $\bar{\Gamma}$-$\bar{\mathrm{M}}$. In the absence of spin-orbit coupling, mirror symmetry excludes p_y orbitals along this momentum direction because they cannot mix with $p_{x,z}$ orbitals. This is shown in Fig. 4.6d, where the $\alpha = 0$ case has a p_y projection of zero along the $\bar{\Gamma}$-$\bar{\mathrm{M}}$ line. Turning on spin-orbit coupling will mix in p_y orbitals (making their contribution finite along $\bar{\Gamma}$-$\bar{\mathrm{M}}$ in 4.6c,d) by allowing them to couple to spinors in a way that respects mirror symmetry, i.e. p_y will couple to the opposite spinor of that to which $p_{x,z}$ orbitals couple. The $p_{x,y}$ orbitals at $\bar{\Gamma}$, and the p_y orbitals along $\bar{\Gamma}$-$\bar{\mathrm{M}}$ are present only because of spin-orbit coupling and are subject to symmetry rules. Therefore, they are constrained in the spins to which they couple.

However, at high $|k|$ along $\bar{\Gamma}$-$\bar{\mathrm{K}}$, where there are not the same symmetry constraints, $p_{x,y}$ orbitals contribute appreciably even in the absence of spin-orbit coupling ($\alpha = 0$), as can be seen in 4.6d. Therefore, turning on spin-orbit coupling will change the orbital character only slightly here, and the properties detected with any photon polarization are primarily non-spin-orbit coupling effects. At high $|k|$, two basis states are no longer sufficient to describe the surface complexity, as is evident from the presence of extra bands along $\bar{\Gamma}$-$\bar{\mathrm{K}}$ in 4.6a. In this region with more states, more basis vectors are needed: $|p_+, \uparrow\rangle$ and $|p_-, \downarrow\rangle$, with $J_z = \pm\frac{3}{2}$. Generally, the inclusion of $J_z = \pm\frac{3}{2}$ components without symmetry constraints will alter the phase between the spin-up ($|\uparrow\rangle$) and spin-down ($|\downarrow\rangle$) components of the real spinor wavefunctions that couple to p orbitals, and may lead the spins not to reverse with different photon polarizations (e.g. non-zero linear combinations of $|p_+, \uparrow\rangle$ and $|p_+, \downarrow\rangle$ will never show this effect). This less constrained spin-orbital coupling along $\bar{\Gamma}$-$\bar{\mathrm{K}}$ is in contrast

to $\bar{\Gamma}$ and $\bar{\Gamma}$-$\bar{\mathrm{M}}$, where symmetry protects the way that $J_z = \pm\frac{1}{2}$ and $J_z = \pm\frac{3}{2}$ mix, preserving the observation of opposite spins with different photon polarizations. Lastly, we note that hexagonal warping effects[208], could not be responsible for the sudden change of the spin texture at large $|k|$ because they do not alter the orbital texture and instead just diminish the magnitude of in-plane spin polarizations.

4.5 Conclusion

This chapter showed that the previously discovered coupling between the spin textures and orbital textures can vary across the Brillouin zone. Knowledge of the full complexity of a surface state's wavefunction, including the symmetry rules governing the coupling of spin and orbital degrees of freedom, is a fundamental prerequisite for its application to spintronics or other technologies. One would expect to see orbitals with different spin orientations in the parts of a spin-orbit material's surface Brillouin zone where various symmetries protect it. Away from these momenta, surface states are allowed to mix with other states, ending the requirement that each orbital character couple to distinct spin textures. This picture provides an understanding of the full complexity of a surface state's spin degree of freedom.

Chapter 5

Spin-Orbit Coupling in a Cuprate Superconductor

Up to now, all of the work presented has been on materials whose key properties are known to stem from strong spin-orbit coupling, where broken inversion symmetry at the surface allows for spin-polarized surface states. This chapter presents a material of great importance to the condensed matter community in which spin-orbit effects had been ignored. The results point to a new type of spin structure that can have important implications for materials with centrosymmetric crystals.

5.1 Spin-orbit coupling and electron correlation

Many of the exotic properties of quantum materials stem from the extreme strength of spin-orbit coupling or electron-electron correlation. Topological insulators are the archetypal example of materials at one extreme, with weak electron correlation but strong spin-orbit coupling that yields a nontrivial spin texture with spin-momentum locking, i.e., electron spin dictated by its momentum[31,35]. Cuprate superconductors provide an example of materials at the other extreme, with electron correlation being the dominant interaction that drives the parent compound into a Mott insulating phase. In contrast, the spin-orbit interaction has been mostly neglected or treated as a small perturbation to the Hubbard Hamiltonian and mean field theory in the context of the Dzyaloshinski-Moriya interaction, leading to negligible changes to the electronic ground state of cuprates[209,210,211,212,213].

Recently, there has been an upsurge of interest in materials in which both spin-orbit coupling and strong correlation are important and could potentially lead to exotic quantum states[214,46,42,215]. In the presence of superconductivity, for example, the spin-orbit interaction

can have fundamental consequences for the symmetry of the order parameter[43], in driving a novel pairing mechanism[46,47], and even in hosting new particles[49,50,51].

Spin- and angle-resolved photoemission spectroscopy has been instrumental in studying the consequences of such interplay on the electronic structure of a variety of materials from heavy fermions to iridates[66,216] thanks to its ability to simultaneously probe energy, momentum, and spin structure of quasiparticles. However, because of earlier predictions of negligible spin-orbit interaction in cuprates[210], no experimental studies probing the spin character of quasiparticles exist to date. Here we report the first such study, revealing unexpected consequences of the spin-orbit interaction on the electronic structure of cuprates.

5.2 The mystery of high T_c cuprate superconductors

Ever since their discovery in 1986[217], the high temperature cuprate superconductors have puzzled physicists[218]. They represented a large jump in known critical temperatures for superconductors from 23 K in Nb_3Ge[219] to 92 K in YBCO, discovered months after the first cuprate[220]. More importantly, it is clear that they must be described by physics beyond the BCS theory that had explained all previously known superconductivity. Still, the underlying mechanism that allows electrons to pair up and move through the material without resistance has proven elusive and provided the greatest mystery in the field of condensed matter physics for the last three decades.

Conventional superconductivity was discovered in mercury in 1911 and finally explained by Bardeen, Cooper, and Schrieffer in 1957[221]. Their BCS theory demonstrated that phonons can act as a glue, binding electrons into Cooper pairs: bosons that can behave as a superfluid. BCS superconductivity only emerges at low temperature, where electrons' interactions with atomic vibrations are not drowned out by thermal energy. Below this critical temperature, the electronic structure develops an energy gap at the Fermi surface that represents the energetic cost of breaking Cooper pairs.

The class of cuprate superconductors are all far more complicated compounds than previously known superconductors. All of the cuprates have parent compounds that are ceramic antiferromagnetic insulators[55], a surprising starting point for a superconductor. Through either electron or hole doping, all become metallic superconductors, each with an optimal doping for highest T_c. All consist of CuO_2 layers where the Cooper pairs move and charge reservoir layers in between. $Bi_2Sr_2CaCu_2O_{8+\delta}$, the Bi-based compound with two CuO_2 layers per unit cell is the cuprate most studied by photoemission, and now for the first time, spin-resolved photoemission.

That superconductivity would emerge in compounds so different from conventional superconductors remains puzzling. Whereas BCS superconductors have an energy gap in all directions of momentum space, the gap in cuprates has a strange d-wave symmetry, with four nodes in the Brillouin zone where the spectrum is ungapped[54]. All have a very complex phase diagram, including an enigmatic "pseudogap" phase[222,223,224] that might compete with superconductivity or might represent the beginning of its formation. Competing orders

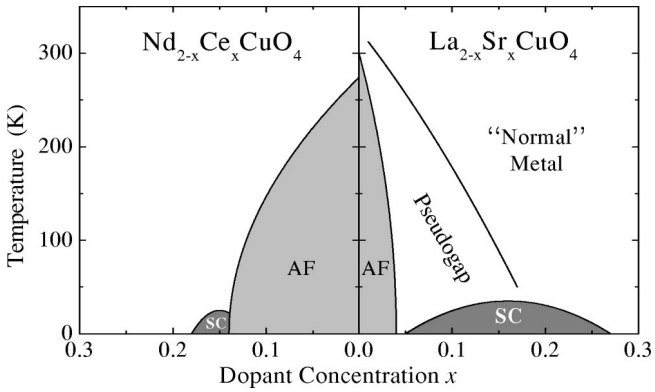

Figure 5.1. **Phase diagram of electron- and hole-doped cuprates, from Ref.[55].**

such as charge density waves[225,226,227] and various structural distortions[228,229,230] complicate things further. Moreover, how the cuprates relate to other unconventional superconductors, especially the recently discovered iron-based superconductors[231] intrigues researchers in the field.

As various experiments have added new riddles to the high T_c field, the fundamental question of what acts as the glue binding Cooper pairs at such high temperature has remained. Resonating valence bonds[232], antiferromagnetic fluctuations[233], and electron-phonon coupling[71] could all play into it[218]. To the accumulation of known complexity in the cuprates we bring our novel experimental technique to bear and add another complication, or perhaps a clue to how superconductivity could emerge.

5.3 Spin-ARPES measurements of $Bi_2Sr_2CaCu_2O_{8+\delta}$

The spin-dependent character of overdoped $Bi_2Sr_2CaCu_2O_{8+\delta}$ (Bi2212) samples (T_c=58 K) is studied with spin-ARPES over a wide range of binding energies, momenta, temperatures, and photon energies. Experiments were performed by coupling our uniquely efficient spectrometer[4] to a 6 eV pulsed laser source and synchrotron light of different photon energies to allow a full energy and momentum mapping of quasiparticle spin polarization over the entire Brillouin zone. Samples were measured both in the superconducting and normal state.

5.3.1 Nodal and off-nodal momentum cuts

Figure 5.2 shows the low-temperature spin-integrated (panels b,e) and spin-resolved (panels c,f) energy ($E - E_F$) vs. momentum (k) maps of the quasiparticle spectrum. Data are shown for two different momentum cuts: along the nodal direction (Γ-Y, panels b,c), where the superconducting gap is zero, and along an off-nodal direction (panels e,f), where the

superconducting gap is approximately 10 meV. The location of the cuts (black line) and the photoelectron spin components (blue and red arrows) are shown in the inset of panels b-f.

Figure 5.2 summarizes the most surprising findings of this experiment, the presence of a nonzero spin polarization in Bi2212 and its strong dependence on momentum. Along the nodal direction, we find that the photoelectron spin component perpendicular to Γ-Y is strongly polarized up, as shown by the spin-resolved intensity map in panel c that is primarily blue. The corresponding spin polarization is positive along this entire cut (see panel d). The polarization shows an overall increase as a function of momentum (or energy) from roughly +20% at the Fermi momentum, k_F (Fermi energy, E_F) to as much as +40% for smaller momentum (or higher binding energies), i.e. closer to the Brillouin zone center, Γ.

Remarkably, when we move away from the nodal direction, the perpendicular photoelectron spin component reverses and is strongly polarized downward, as seen in the spin-resolved intensity map in Fig. 5.2f that is primarily red. The reversal of the intensity peak from primarily spin-up to primarily spin-down can be clearly seen in panel h, where the spin-ARPES spectra at k_F as a function of energy (energy distribution curves or EDCs) are directly compared for both the nodal and off-nodal cuts.

A closer look reveals a similar increase of the spin polarization for the off-nodal cut (Fig. 5.2g) toward smaller $|k|$ or higher binding energy. In this case, the polarization is negative ($P = -15\%$) at k_F but eventually turns slightly positive ($P = +5\%$) at higher binding energy. In summary, along both of these cuts, we observed an unexpected nonzero spin polarization that becomes more positive as one goes toward higher binding energies (i.e., deeper inside the Fermi surface).

5.3.2 Momentum dependence of spin polarization

Figure 5.3 shows the evolution of the photoelectron spin polarization along the Fermi surface and at a binding energy of 160 meV (see, e.g., vertical lines in Fig. 5.2c,f). The spin-resolved EDCs at k_F and at smaller momenta k_{HBE} (high binding energy), are shown in panels a and b, respectively. The location of each spectrum is shown in panel c. This information can alternatively be viewed free of intensity through the spin polarization. Fig. 5.4 shows the spin polarization of the spin-resolved EDCs in Fig. 5.3.

In both cases, we observe a net spin polarization that decreases away from the node ($\phi = 0°$), eventually reaches zero at an intermediate angle and, for the spectra at $k = k_F$, even switches sign far away from the node. These results are summarized quantitatively in panel 5.3d, for both $k = k_F$ and $k = k_{HBE}$. The spin polarization is even about the nodal line, where it reaches its maximum with values as high as +40%. Notably, it is higher at k_{HBE} than at k_F over the entire angular range.

These results combined provide the first spin-resolved measurement of the Fermi surface of a cuprate superconductor. It is clear that the two spin channels $I_\uparrow$ and $I_\downarrow$ are each stronger

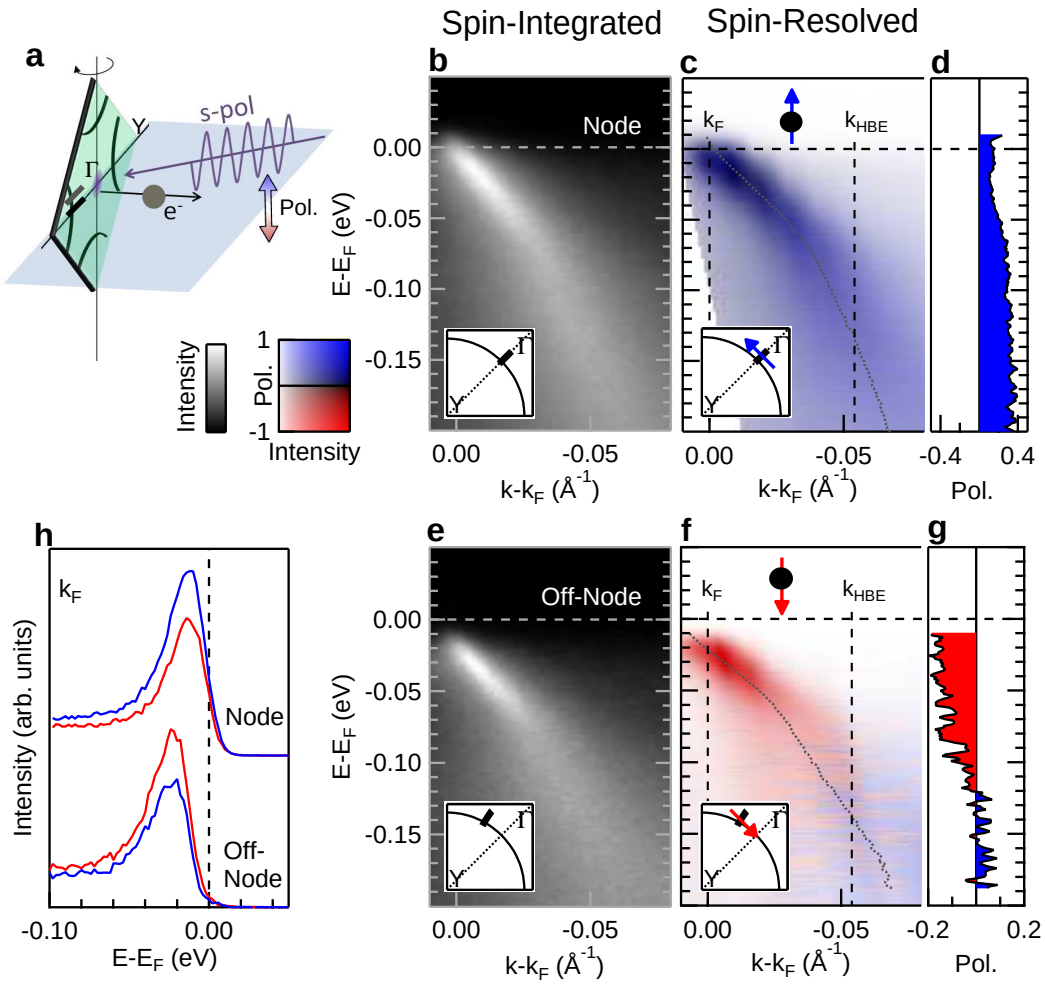

Figure 5.2. **Spin-resolved measurements along nodal (Γ-Y) and off-nodal cuts.** **a,** Experimental geometry. **b,** Spin-integrated map of the band near E_F along the nodal direction. **c,** Spin-resolved map taken along the same cut as in b, presented with darkness representing photoemission intensity, while color represents spin polarization. **d,** Plot of the spin polarization along the band dispersion (dashed gray line in c). **e-g,** Same as b-d but measured along a cut parallel to the nodal direction that intersects the Fermi surface 14° away from the node, as measured from the zone corner. The same spin component was measured in b-d and e-g. **h,** Spin-resolved energy distribution curves (EDCs) taken at the node as well as at the Fermi momentum away from the node.

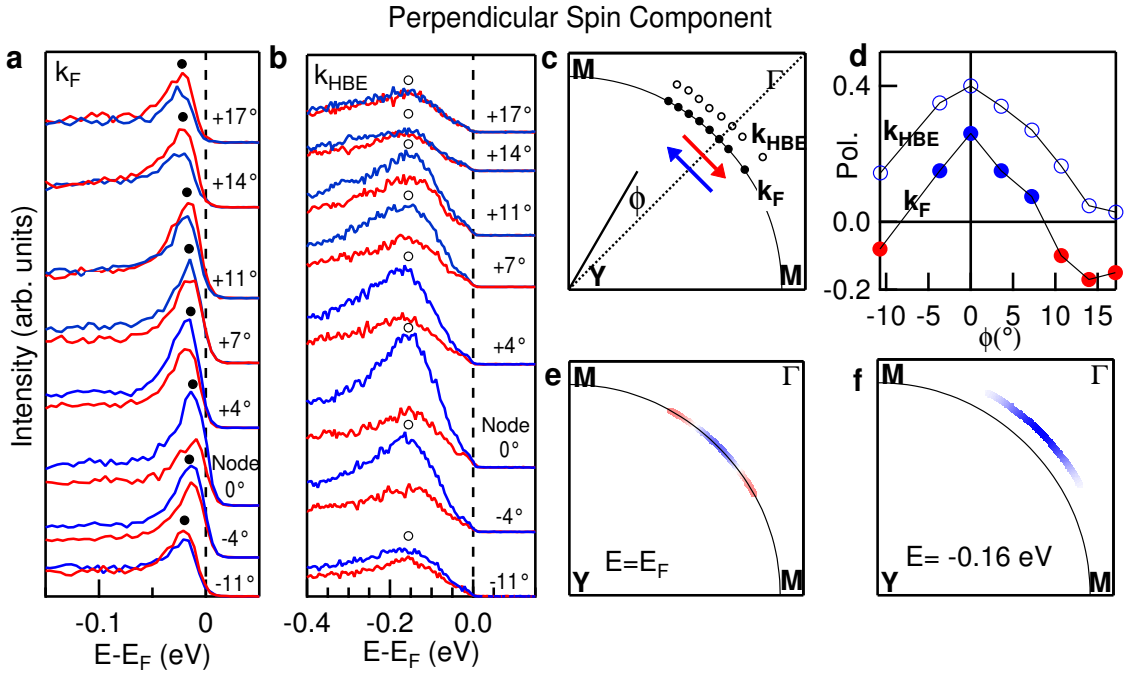

Figure 5.3. **Spin-resolved measurements along Fermi surface and at higher binding energy. a,** Spin-resolved EDCs taken at momenta along the Fermi surface, as well as **b,** inside the Fermi surface where the dispersion is at $E_B \approx$160 meV. EDCs are marked by ϕ, the angle from the zone corner (Y point) to k_F and are taken at momenta indicated in **c,** one quadrant of the Brillouin zone. The spin component measured was perpendicular to the Γ-Y direction and within the plane of the sample surface. **d,** Spin polarization as a function of Fermi surface angle, ϕ at k_F (solid circles) and at higher binding energy (open circles). **e,f,** Schematics of the texture of this spin component.

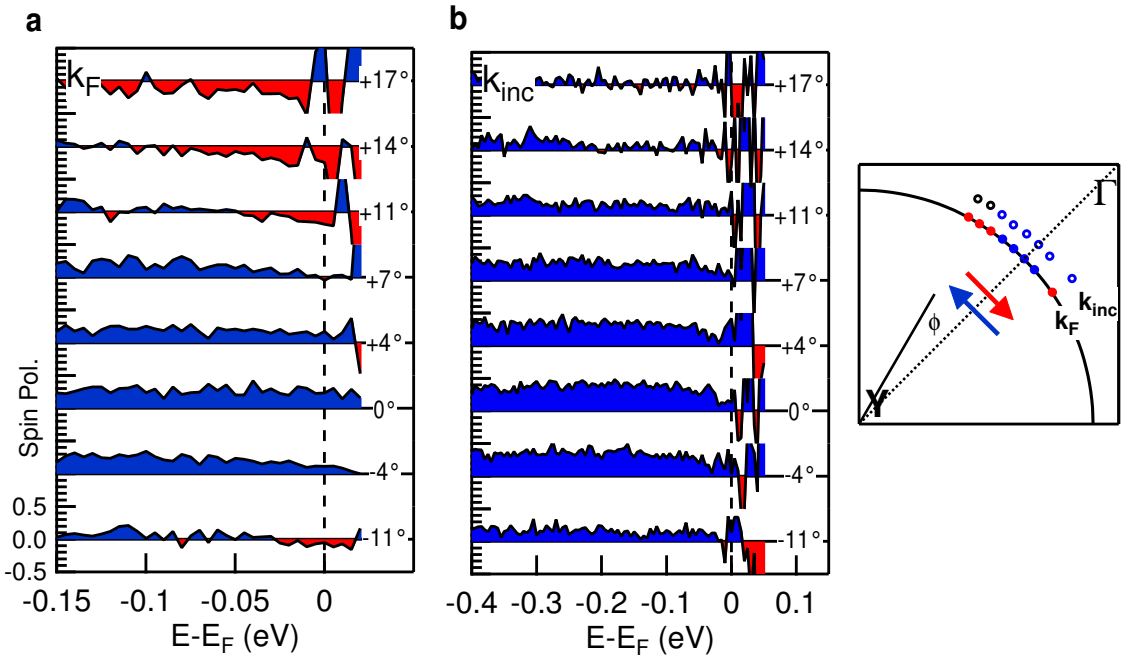

Figure 5.4. **Spin polarizations along the Fermi surface and at $k < k_F$.** Spin polarization as a function of binding energy at k_F (**a**) and at $k < k_F$ (**b**). Each spin polarization EDC is marked with the momentum where it was taken, the angle ϕ from the Y point to k_F. These correspond to the EDCs of intensity in spin-up and spin-down channels shown in Fig. 5.3.

in different parts of momentum space. On the other hand, at higher binding energy (panel 5.3f), the dominant spin channel is spin-up, yielding an overall positive spin polarization.

5.3.3 Initial state effect: measurements around high symmtery points

The presence of any spin polarization in photoemission from Bi2212, let alone a momentum-dependent spin texture, is totally unexpected. It is therefore imperative, before proceeding to discuss the total spin texture, to assess whether the observed spin polarization is the result of a final state effect or represents physics intrinsic to the spin state of itinerant carriers in the material.

Figure 5.5 shows the evolution of the spin polarization across the Brillouin zone boundary (M point, panel b) and Brillouin zone center (Γ point, panel d). Spin-resolved EDCs are shown in 5.5b for the two opposite M points within the first Brillouin zone (points β and γ) and for a point just across the Brillouin zone boundary (α) that is separated by a reciprocal lattice vector from γ. The location of these measurements is represented by vertical arrows in panel a. To access this momentum window, we used higher energy photons: 33 eV. The experimental geometry is shown in Supplementary Materials and the measured spin component is perpendicular to the Γ-M direction.

The data show a clear reversal of this component of spin polarization at the two opposite zone boundaries (curves β and γ) and across the zone boundary (curves α and β). The presence of a nonzero spin polarization at different photon energies (6 eV and 33 eV shown here, additionally 44 eV and 55 eV in Fig. 5.9) asserts that the observed effect is a property of the quasiparticle initial state rather than being a final state effect. Moreover, the observation of (i) a reversal of the spin polarization at two points very near in emission angle (curves α and β) but on opposite sides of the zone boundary and (ii) similar polarizations for points separated by a reciprocal lattice vector and hence with similar momentum (curves α and γ), but with nearly opposite emission angles confirm the intrinsic nature of the effect and its dependence on quasiparticle momentum rather than photoemission angle.

We can learn more about the pattern of spin polarization across momentum space by utilizing a well-known property of Bi2212, i.e., the presence of an incommensurate superstructure along the b-axis due to the modulation of Bi-O layers. This structural distortion creates umklapp bands that are replicas of the main band on the Fermi surface (dashed lines in Fig. 5.5a), shifted by the superstructure vector along the Γ-Y direction[229,55]. Therefore, the second order superstructures of the main band, labeled SS1 and SS2, lie near Γ.

These replica bands are clearly visible in the $h\nu$= 6 eV ARPES intensity maps (Fig. 5.5c) at the two opposite sides of the Γ point, and disperse up toward Γ. The spin-resolved EDCs at k_F, measured along the dotted vertical lines in panel c, are shown in panel d and measure the component of the photoelectron spin perpendicular to the Γ-Y direction. Two clear observations can be made from the data. The first one is that the superstructure bands on

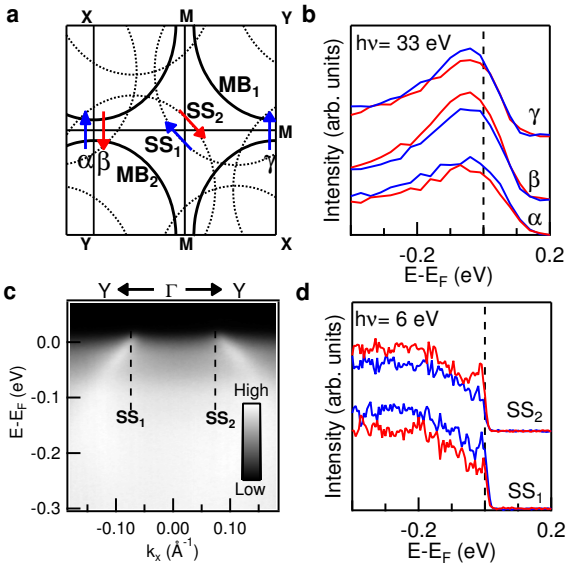

Figure 5.5. **Measured spin polarization near M points and of the superstructure on either side of Γ. a,** Spin textures from the two distinct experiments in b and d plotted in the Bi2212 Brillouin zone. The main band is shown with thick lines, while its superstructure replicas are thin dashed lines. **b,** Spin-resolved EDCs taken with hν=33 eV at momenta shown in a near the M points. **c,** Spin-integrated map of the superstructure taken with hν=6 eV, showing bands that replicate the main band dispersing up as they approach Γ. The dashed lines indicate approximate positions of spin-resolved measurements. **d,** Spin-resolved EDCs on either side of Γ.

the two sides of the Γ point have opposite spin polarization, as seen in the EDCs for SS1 and SS2 in panel d. This reversal of the spin component through a small angle across the Brillouin zone center (SS1 vs. SS2) corroborates the reversal seen at opposite momenta in EDCs β and γ, pointing to a spin polarization that not only is a function of k, but also respects time reversal symmetry by switching sign across the Γ point.

The second observation is that at the node, the superstructure bands show opposite spin polarization with respect to the main bands of which they represent a second order replica. Rather, they match the spin of the main band in the same quadrant of momentum space. Indeed, though the superstructure band SS2 at $+k$ is the second order replica of the main band MB2 at $-k$, the spin direction is opposite to that of MB2 (see MB2 in panel a and Fig. 5.2c for the relative spin polarization). Instead, it is the superstructure band SS1 at $-k$ that matches the positive spin polarization of the main band MB2 at $-k$. A quasiparticle's spin seems to be determined by the quadrant of momentum space that is in, not any scattering effect. The spin polarizations discovered in this work are a true texture in momentum space.

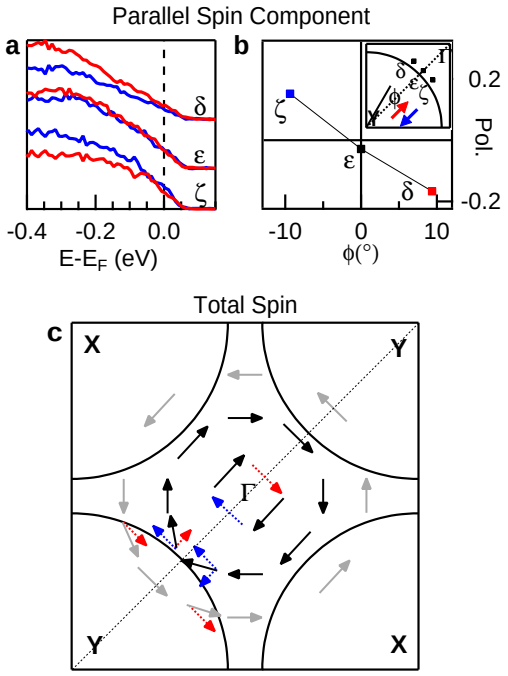

Figure 5.6. **Total in-plane spin texture. a,** Spin-resolved EDCs, acquired with sensitivity to the component of spin parallel to Γ-Y. **b,** Spin polarization as a function of Fermi surface angle, ϕ. The inset shows the positions in one quadrant of the Brillouin zone where EDCs were taken. **c,** Schematic of the addition of the spin textures parallel (from b) and perpendicular to (from Fig. 5.3d) the Γ-Y direction. The counterclockwise circle of gray arrows is consistent with the one component of spin able to be measured at high k.

5.3.4 Helicity of spin texture

The reversal of measured spin polarizations across the Brillouin zone center and the Brillouin zone boundary could suggest a spin texture circling the Γ point. To further investigate such a scenario, we measured the polarization parallel to the Γ-Y direction (i.e., perpendicular to the spin component measured in Figs. 5.2, 5.3, and 5.5b).

In particular, Figure 5.6a shows the spin-resolved EDCs for the momentum cuts indicated in the inset of panel b. At the node (ϵ), the intensity peaks are quite similar for the two spin components (panel a) and the polarization is nearly zero (panel b). Away from the node, the spectra at δ show the opposite spin polarization of those at ζ, which lies on the opposite side of the Γ-Y direction (ϵ). This is true for each measured angle (not shown), implying a reversal across the Γ-Y symmetry line of the spin polarization projection parallel to Γ-Y. Such a reversal is in contrast with the perpendicular spin component (see Fig. 5.3) that remains the same across the nodal direction.

By schematically adding the even behavior of the perpendicular spin component about Γ-

Y with the odd behavior of the parallel component, we obtain the full spin texture of Bi2212 across the Brillouin zone, shown in Figure 5.6c. The reversal of the spin polarization across the Γ-Y symmetry line (Fig. 5.6a,b) and across the Brillouin zone quadrants (Fig. 5.3a,b and Fig. 5.5d) together with the zero spin polarization of the parallel spin component along Γ-Y are suggestive of a spin texture circling the Brillouin zone center (Γ) clockwise. This spin-momentum locking is reminiscent of a Rashba type effect. We note, however, that observations of the Rashba effect typically have two bands of opposite spin polarization that are split in energy. Here, we only observed a single spin polarization at any particular momentum, regardless of the band's binding energy there. This enables drawing a single spin texture in k space.

Meanwhile, at larger k, the larger angle (ϕ) measurements in Fig. 5.3b with spin pointing in the opposite direction of those at small ϕ demonstrate that the texture has a complex momentum dependence. While many parameters discussed in this dissertation can shape the spin pattern seen in a photoemission experiment. One possibility with the geometry used here is the presence of an outer spin texture circling Γ with counterclockwise rotation, sketched in gray in Fig. 5.6c.

5.3.5 Temperature dependence

To test whether the surprising new spin physics is a property of the superconducting state, the spin polarization of the sample was measured above and below the sample's superconducticting critical temperature of 58 K. Figure 5.7 shows EDCs taken at the node and at $\phi = 14°$, similar to Fig. 5.2, with the sample at temperatures 30 K and 90 K.

At the higher temperature, the quasiparticle peaks are broadened and diminished in height as some coherence is lost. Nonetheless, the $\approx 25\%$ spin polarization at the node clearly persists into the normal state. The spin polarization may not be a signature of superconductivity in Bi2212, but the underlying spin-orbit coupling that causes it might still shape the way Cooper pairs form.

5.4 Local inversion symmetry breaking

The presence of any spin polarization in photoemission from Bi2212, let alone its novel spin texture with spin-momentum locking, is completely unexpected. As demonstrated above, this is not the result of a final state effect, but rather the manifestation of an intrinsic property of its initial state. While an exotic spin texture can be accounted for by the interplay of spin-orbit coupling with various mechanisms of symmetry breaking[234,235], such as loop currents[236] that break time reversal symmetry, in the remaining part of this work, we show that a simple model respecting the symmetries of the Bi2212 crystal explains an observed nontrivial spin pattern.

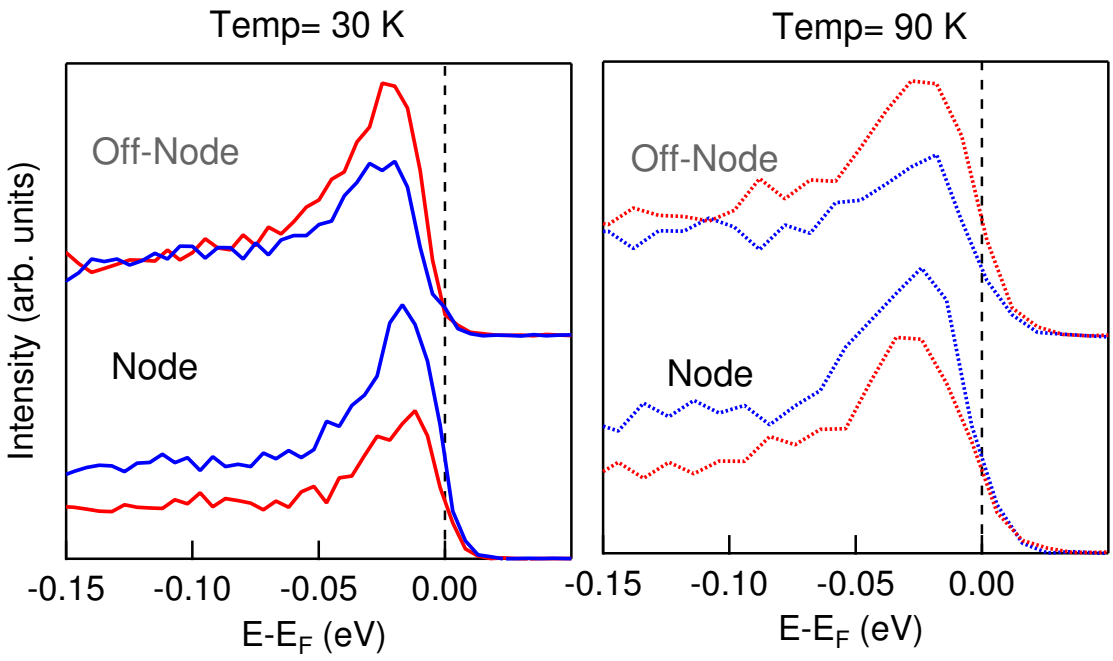

Figure 5.7. **Spin-resolved measurements above and below $T_c = 60K$.** At the node and away from it, the spin polarizations persists into the normal state even as the quasiparticles lose coherence.

Perhaps the most studied spin textures appear due to the Dresselhaus-Rashba effect[9,10], which can be present in non-centrosymmetric materials (i.e., materials lacking inversion symmetry) and is known to produce a momentum spin-splitting of the energy bands. Recently, it has been pointed out that a *local* electric field within the unit cell can also give rise to a spin structure even in centrosymmetric materials [237]. In this case, the spin-split bands are spatially segregated in real space, e.g., top and bottom layers in a layered material[29,28]. Nevertheless, the net spin polarization is zero as the electric field averages to zero within the unit cell. This model has also been adapted to explain the residual energy splitting at the node due to bonding and and anti-bonding bands in $YBa_2Cu_3O_{6+\delta}$[213], and to predict topological superconductivity in Rashba heterostructures[46].

A comparable model can be applied to Bi2212 and can account for the observed spin texture. Indeed, while Bi2212 is a centrosymmetric system, because of its bilayer structure, the inversion center is between Cu-O planes: one Cu-O layer sees Bi-O ions above and Ca ions below, while this is reversed for the other Cu-O layer in the unit cell. The absence of inversion symmetry will allow for a local electric field within the unit cell (see schematic in Fig. 5.8) that is sufficient to generate the spin texture reported here. To calculate the spin texture, we adopt a simple tight-binding model in the presence of such a field, similar to the one used in Ref.[237]. The model accounts for the presence of the local field via a Rashba-type spin-orbit coupling with opposite sign on the two different layers of the unit cell. We find that upon addition of such terms, the bonding (anti-bonding) band loses its purely anti-symmetric (symmetric) character under mirror symmetry while remaining doubly degenerate

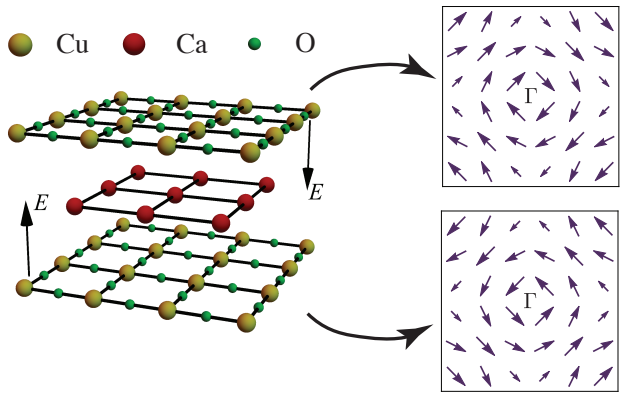

Figure 5.8. **Spin structure within the unit cell.** Schematic view of the two Cu-O bilayer structure in $Bi_2Sr_2CaCu_2O_{8+\delta}$, where we omit layers of Bi-O and Sr-O which separate bilayers. Green atoms correspond to oxygen, yellow to copper, and red atoms in between are Ca. Arrows schematically depict the possible direction of electric field, which leads to the spin-orbit coupling of the opposite sign on different layers. The top and bottom Cu-O layers of the unit cell each have their own theoretical expectations for the spin pattern of the anti-bonding band.

at any momentum in the Brillouin zone as the crystal retains unbroken inversion and time reversal symmetries. Such spin-orbit coupling endows the bonding and anti-bonding bands with opposite spin polarization on each individual Cu-O layer, and provides an additional contribution to splitting between them. The spin textures for the anti-bonding orbital in the two Cu-O layers that result from this model are shown in Figure 5.8.

Photoemission measures the interference pattern of contributions from several near-surface layers[190] and in this case has different intensity from bonding and anti-bonding bands[70,79]. Therefore, a nonzero spin signal is expected despite inversion symmetry and the lack of resolved band splitting. This spin texture stems from differences in photoemission matrix elements for different components of the wave function as well as the surface sensitivity of the measurement and interference effects. This should also result in a complex dependence on photon energy, presented below.

5.4.1 Photon energy dependence

The spin textures that this work discovered in BSCCO exist for a single band within a single Cu-O layer. Bonding and anti-bonding bands have opposite spin textures, just as opposite Cu-O layers within a unit cell do. These hidden spin textures are revealed by the differential sampling of electronic states in the atomic layers located at different depths below the surface. As a function of photon energy, the photoemission matrix elements for each band change, as does the intensity from each Cu-O layer. The measured spin texture is the interference pattern of contributions from different bands at different real space distances from the surface and is thus strongly photon energy dependent[29]. This has been shown to

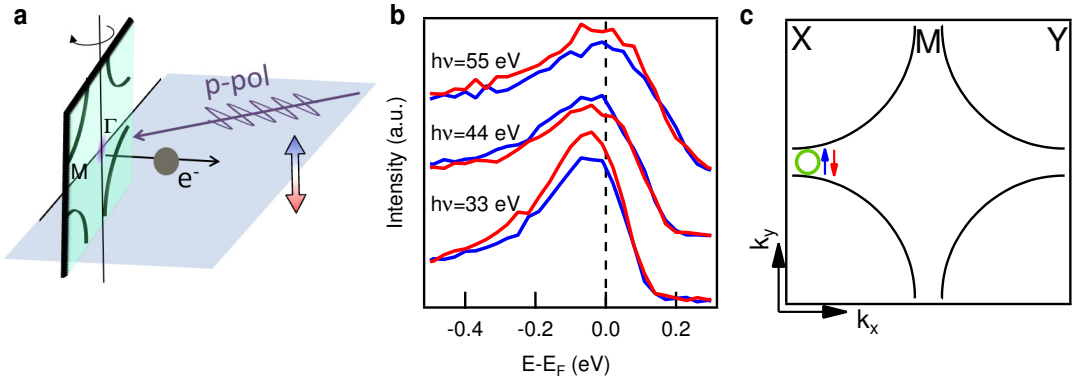

Figure 5.9. **Spin-resolved measurements near the M point as a function of photon energy.** **a**, Experimental geometry for all synchrotron measurements. **b**, Spin-resolved EDCs near the M point as a function of photon energy. **c**, Position in momentum space of the measurement, with arrows to indicate defnitions of spin-up and spin-down.

be true even in a topological insulator whose surface state has a nonvanishing spin texture when integrated through the whole unit cell[76].

Figure 5.9 shows spin-resolved EDCs measured near the M point at various photon energies. The measurement geometry, shown in 5.9a, is the same as for EDC β in Fig. 5.5d. With hν=33 eV, a negative spin polarization was measured, as was shown in the main text. However, with hν=44 eV, a slightly positive spin polarization was seen. This reverses back to a negative spin with hν=55 eV. This strong photon energy dependence corroborates the given explanation for the spins seen in BSCCO. The way the hidden spin textures are revealed by spin-ARPES depends significantly on the coupling of photons to the different electronic states.

5.4.2 Other forms of local inversion symmetry breaking

Though the tight-binding model reproduces the finite spin polarization observed in these experiments, more involved calculations are needed for both a quantitative description of the observed effects and to unambiguously identify the pattern of electric field within a unit cell. While the mechanism described here applies to bilayer materials, in principle, any structural distortion that breaks local inversion symemtry on Cu or O sites can induce electric fields and could potentially lead to analogous effects. Indeed, unscreened electric fields along the c-axis in cuprates have been reported[238]. Moreover, Jahn-Teller type distortions due to vertical displacements of the Cu atoms and tilting of the Cu-O octahedra[228,230] can also generate local fields. The observation of a nonzero spin polarization in single layer Bi2201[239] suggests that these additional factors might play a role in generating novel spin textures.

5.5 Conclusion

This chapter has shown that our previous understanding of how spin-orbit coupling can be manifested in crystals was incomplete. Even in a crystal that retains inversion symmetry, there can be a spin structure in real and momentum space. Important spin-orbit effects were shown in a material in which the interaction was previously thought to be irrelevant.

Given the surprising relevance of spin-orbit coupling in creating spin structure in Bi2212, it will be vital to understand its interplay with strong electron-electron correlation and superconductivity. In particular, the spin-orbit coupling may admix the triplet pairing component to the superconducting gap[43,240], affect spin susceptibility[241], alter the structure of the gap nodes, and even allow for the pairing due to Amperean-type attraction mediated by spin fluctuations[242,47]. More detailed studies of the interplay between spin textures and superconductivity are urgently needed.

Chapter 6

Conclusion and Future Directions

This dissertation has demonstrated the surprising ways spin-orbit coupling can be manifest in a crystal, and how that manifestation can be shaped by the crystal symmetry. It highlighted rules that should be considered in the search for new types of spin textures.

In the case of orbital-dependent spin textures, we saw that mirror symmetry can cause distinct atomic orbital components of a wave function to couple to distinct spin textures. The entanglement between spin and orbital components means that one must seek to understand a spin-orbital texture of a surface state. However, it was shown that at momenta away from mirror planes and high symmetry points, a single, orbital-independent spin texture returns. These rules can be extrapolated to other surface states that experience a strong spin-orbit interaction to provide guidance about where and how the key degrees of freedom would be entangled.

In the case of the cuprate superconductors, it had been thought that spin-orbit coupling is negligible and the structure of the crystal requires spin degeneracy in the bands. However, we discovered that there is still structure to the spins in the crystal: there are two spin textures with opposite spin in opposite parts of the unit cell. Symmetry may require equal number of spins along any axis, but it also provides a structure within which those spins become spatially segregated.

Taken together, these two sets of findings point to how incomplete our understanding of spin-orbit coupling in crystals has been. Research has focused on finding spin textures in momentum space, when in fact, there are several other parameters that must be considered: where in the crystal is the spin texture of interest and of which orbitals is it composed? Clearly, there is still very rich physics to explore in how spins arrange themselves in crystals and how that can be manipulated. Some ideas for future directions are discussed below.

6.1 Cuprates and Layered Materials

The study presented here demonstrated that a spin ordering in momentum space exists in overdoped Bi2212. Only with differential sensitivity to distinct bands and distinct parts of the unit cell can this structure be seen.

This discovery suggests a need to better understand the impact of spin-orbit coupling on cuprate physics. Theoretical work should seek to understand how it affects superconductivity: does it help or hurt it? Does it create a triplet component of Cooper pairs[43,240]? Does it even provide a way for Cooper pairs to form[242,47]? Initial theory work could provide motivation for further experiments.

On the experimental side, it will be important to understand how alterations to the crystal affect the spin structure since that structure is enabled by the crystal's symmetry. Studies that track the spin texture across a range of hole doping (by varying how much oxygen is doped in) will be insightful about how the spin ordering interacts with superconductivity. Are there meaningful differences at lower doping in the pseudogap phase?

We know that a similar effect exists in single layer Bi2201, though the mechanism of local inversion symmetry breaking is less clear. It will be valuable to study crystals in which the inherent structural distortions are altered[228,230]. How would Pb doping, replacing some Bi sites and eliminating the superstructure alter the spin texture? Would the three layer compound, Bi2223 behave more similarly to Bi2201 as both have odd numbers of layers? Would stretching the bond lengths of Bi2201 by doping in Lanthanides[243] alter the strength of spin polarization or shape of the spin texture by stretching the unit cell?

Lastly, the models used to account for the spin texture solely involve hopping within the Cu-O layers, where there is structural asymmetry. Thus, it will be valuable to test whether other cuprates that do not have the heavy Bi atoms still have hidden spin structures. Do other single layer cuprates still have the requisite structural elements to locally break inversion symmetry and create a spin texture?

The findings of meaningful spin-orbit coupling in the cuprates point to a need to study how spin-orbit interacts with superconductivity and electron-electron correlation. It was found that spin-orbit coupling creates a triplet component of Cooper pairs in Sr_2RuO_4[44]. In the iridates, the Coulomb interaction is able to open a Mott gap because the band at the Fermi level has already been spin-orbit split. The combination of the two interactions turns what would be a metal into an insulator. How else could they interact in other contexts?

More, broadly, the work on the cuprates demonstrates that there could be an enormous number of layered materials that could harbor hidden spin order. Similar spin textures were recently discovered in dichalcogenide materials[29,28]. These findings suggest an opportunity to explore how spin textures can be tuned by altering substrates, sample thickness, or by creating heterostructures to engineer electric fields through a thin film. The search for more hidden spin textures may come to encompass materials of technological interest and create ways to design materials with desired spin structures.

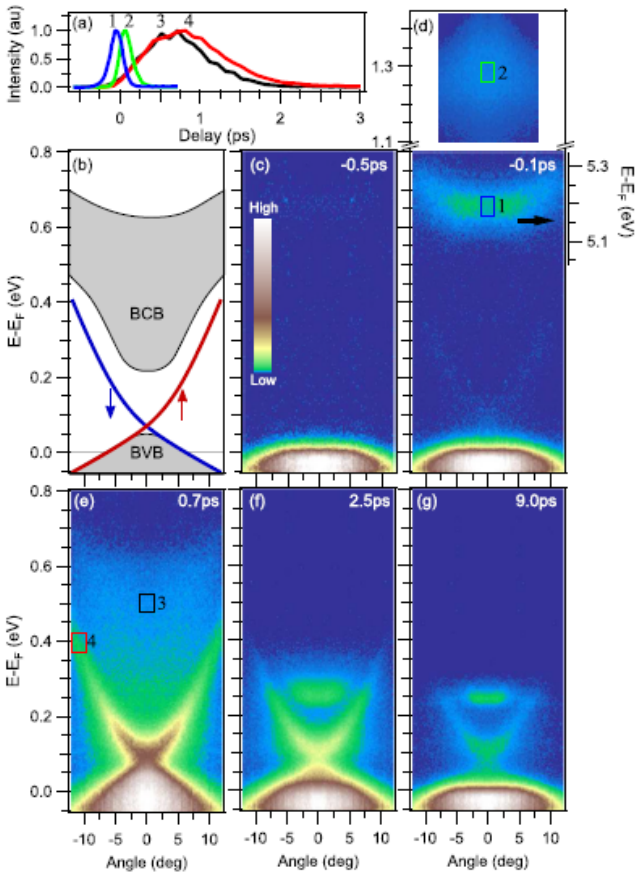

Figure 6.1. **Dynamics in Bi_2Se_3 from Ref.[156]. a,** Population dynamics for various states, corresponding to boxes in d,e. **b,** Schematic of the band structure of Bi_2Se_3 , including color coding for spin texture of the surface state. **c,** Equilibrium population before pumping. **d,** During temporal overlap of pump and probe beams, an image potential state (1) and a high energy bulk state (2) are populated. **e-g,** After pumping, the transient population decays into the bulk conduction band and Dirac surface state, where dynamics slow down signiicantly.

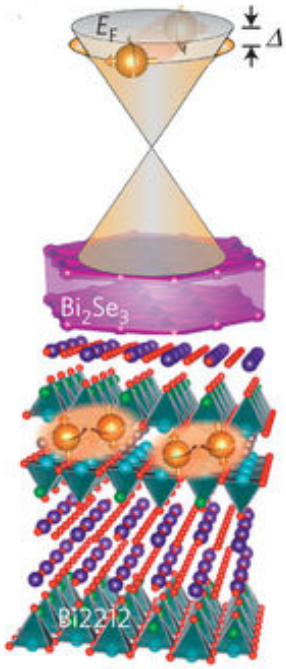

Figure 6.2. **Bi_2Se_3 thin films on Bi2212 substrate from Ref.[48].** Schematic of crystals at interface and resulting surface state band structure in Bi_2Se_3 . The cone features an *s*-wave superconducting gap.

6.2 Manipulating spin-orbit materials

If the work presented in this dissertation added complexity to the story of spin-orbit coupling by introducing important degrees of freedom that must be accounted for, it also suggests opportunities to manipulate spin-orbit coupling in materials. For example, ferromagnetism is known to open up a band gap in otherwise massless topological surface states by breaking time reversal symmetry[244]. The same alteration of symmetry could be achieved by the application of circularly polarized light. One could test whether such irradiation could, on an ultrafast timescale, allow for opening and closing a gap and what effect that has on the spin-orbital texture of the surface state.

More broadly, time domain studies could demonstrate how any spin-orbit materials behave out of equilibrium. For example, spin-integrated pump-probe measurements of Bi_2Se_3 were used to study how carriers move between the surface state and bulk as they return to equilibrium[156], shown in Fig. 6.1. Such studies are key to understanding any potential utility of spin-orbit materials, as any device applications will involve pushing them out of equilibrium. However, the spin degree of freedom is key to their proposed utility, and pump-probe studies are needed to understand *spin-dependent* dynamics. Knowing that dynamics happen in bands shaped by spin-orbit coupling, it will be important to understand what decay mechanisms are available separately for opposite spins. For example, does spin-orbit coupling affect the recovery of superconductivity in the previously discussed case of Sr_2RuO_4?

Time domain measurements can even yield insight about how spin-orbit coupling shapes

the formation of states in the first place. Studying normally unpopulated bands with spin resolution led to the discovery of new states that yielded insight about the topological phase transition[63].

On top of this, layering and tuning the thickness of spin-orbit materials provides a mechanism to control the interaction and its effects. For example, in transition metal dichalcogenides, spin splittings are altered dramatically between monolayer and bulk samples, pointing to the possibility of building an ideal material for valleytronics[245,246,247]. More spin-resolved work is needed to understand how changing sample thickness and the strength of interlayer interactions can alter spin-orbit coupling in these materials.

Mixing spin-orbit materials with others also provides the opportunity to engineer novel properties. For example, it was shown that layering thin films of Bi_2Se_3 on $Bi_2Sr_2CaCu_2O_{8+\delta}$, two of the materials presented in this dissertation, turns the former into a superconductor. A schematic of these findings are shown in Fig. 6.2. Intriguingly, it had an *s*-wave superconducting gap, rather than the *d*-wave gap of the Bi2212 substrate[48]. How superconductivity emerges in this topological surface state, and how it is affected by the spin-orbit interaction will be key to understand as part of the effort to use these materials to study Majorana modes.

Moreover, layering topological insulators with magnetic materials can lead to a new mechanism to control magnetism. It has been shown that in passing current through topological insulator/ferromagnet bilayers, the former can cause a large spin transfer torque on the latter, reorienting its magnetization[248,249]. Superlattices of antiferromagnets and magnetically-doped topological insulators exhibit tunable surface spin textures and new forms of magnetic ordering[250]. These developments could lead to very low power means for manipulating magnetic memory in spintronics.

The work presented in this dissertation highlighted the rich, unexplored physics of spin-orbit coupling in exotic materials. There is considerable opportunity for the field to use thes new insights about how spin-orbit materials behave to manipulate and engineer the interaction.

Bibliography

1. Sakurai, J. J. *Modern Quantum Mechanics* (Addison-Wesley, 1994).

2. LaShell, S., McDougall, B. A. & Jensen, E. Spin Splitting of an Au(111) Surface State Band Observed with Angle Resolved Photoelectron Spectroscopy. *Phys. Rev. Lett.* **77**, 3419 (1996).

3. Hoesch, M., Greber, T., Petrov, V. N., Muntwiler, M., Hengsberger, M., Auwrter, W. & Osterwalder, J. Spin-polarized Fermi surface mapping. *J. Electron Spectrosc. Relat. Phenom.* **124**, 263 (2002).

4. Gotlieb, K., Hussain, Z., Bostwick, A., Lanzara, A. & Jozwiak, C. Rapid high-resolution spin- and angle-resolved photoemission spectroscopy with pulsed laser source and time-of-flight spectrometer. *Rev. Sci. Instrum.* **84**, 093904–5 (2013).

5. Tamai, A., Meevasana, W., King, P. D. C., Nicholson, C. W., de la Torre, A., Rozbicki, E. & Baumberger, F. Spin-orbit splitting of the Shockley surface state on Cu(111). *Phys. Rev. B* **87**, 075113 (2013).

6. Pierce, D. T., Celotta, R. J., Wang, G.-C., Unertl, W. N., Galejs, A., Kuyatt, C. E. & Mielczarek, S. R. The GaAs spin polarized electron source. *Rev. Sci. Instrum.* **51**, 478 (1980).

7. Winkler, R. *Introduction*, 1–8 (Springer Berlin Heidelberg, Berlin, Heidelberg, 2003).

8. Winkler, R. *Electron and Hole States in Quasi-Two-Dimensional Systems*, 35–60 (Springer Berlin Heidelberg, Berlin, Heidelberg, 2003).

9. Dresselhaus, G. Spin-Orbit Coupling Effects in Zinc Blende Structures. *Phys. Rev.* **100**, 580–586 (1955).

10. Bychkov, Y. A. & Rashba, E. I. Oscillatory effects and the magnetic susceptibility of carriers in inversion layers. *Journal of Physics C: Solid State Physics* **17**, 6039 (1984).

11. Petersen, L. & Hedegrd, P. A simple tight-binding model of spinorbit splitting of sp-derived surface states. *Surface Science* **459**, 49 – 56 (2000).

12. Reinert, F., Nicolay, G., Schmidt, S., Ehm, D. & Hüfner, S. Direct measurements of the L-gap surface states on the (111) face of noble metals by photoelectron spectroscopy. *Phys. Rev. B* **63**, 115415 (2001).

13. Hoesch, M. *et al.* Spin structure of the Shockley surface state on Au(111). *Phys. Rev. B* **69**, 241401 (2004).

14. Kawakami, R. K. *et al.* Quantum-well states in copper thin films. *Nature* **398**, 132–134 (1999).

15. Grundler, D. Large Rashba Splitting in InAs Quantum Wells due to Electron Wave Function Penetration into the Barrier Layers. *Phys. Rev. Lett.* **84**, 6074–6077 (2000).

16. Hochstrasser, M., Tobin, J. G., Rotenberg, E. & Kevan, S. D. Spin-Resolved Photoemission of Surface States of W(110)-(1×1)H. *Phys. Rev. Lett.* **89**, 216802 (2002).

17. Krupin, O. *et al.* Rashba effect at magnetic metal surfaces. *Phys. Rev. B* **71**, 201403 (2005).

18. Hirahara, T. *et al.* Direct observation of spin splitting in bismuth surface states. *Phys. Rev. B* **76**, 153305 (2007).

19. Weber, C. P., Orenstein, J., Bernevig, B. A., Zhang, S.-C., Stephens, J. & Awschalom, D. D. Nondiffusive Spin Dynamics in a Two-Dimensional Electron Gas. *Phys. Rev. Lett.* **98**, 076604 (2007).

20. Dil, J. H., Meier, F., Lobo-Checa, J., Patthey, L., Bihlmayer, G. & Osterwalder, J. Rashba-Type Spin-Orbit Splitting of Quantum Well States in Ultrathin Pb Films. *Phys. Rev. Lett.* **101**, 266802– (2008).

21. He, K., Hirahara, T., Okuda, T., Hasegawa, S., Kakizaki, A. & Matsuda, I. Spin Polarization of Quantum Well States in Ag Films Induced by the Rashba Effect at the Surface. *Phys. Rev. Lett.* **101**, 107604 (2008).

22. He, K. *et al.* Direct Spectroscopic Evidence of Spin-Dependent Hybridization between Rashba-Split Surface States and Quantum-Well States. *Phys. Rev. Lett.* **104**, 156805 (2010).

23. Nitta, J., Akazaki, T., Takayanagi, H. & Enoki, T. Gate Control of Spin-Orbit Interaction in an Inverted $In_{0.53}Ga_{0.47}As/In_{0.52}Al_{0.48}As$ Heterostructure. *Phys. Rev. Lett.* **78**, 1335–1338 (1997).

24. Heida, J. P., van Wees, B. J., Kuipers, J. J., Klapwijk, T. M. & Borghs, G. Spin-orbit interaction in a two-dimensional electron gas in a InAs/AlSb quantum well with gate-controlled electron density. *Phys. Rev. B* **57**, 11911–11914 (1998).

25. Miller, J. B., Zumbühl, D. M., Marcus, C. M., Lyanda-Geller, Y. B., Goldhaber-Gordon, D., Campman, K. & Gossard, A. C. Gate-Controlled Spin-Orbit Quantum Interference Effects in Lateral Transport. *Phys. Rev. Lett.* **90**, 076807 (2003).

26. Zutić, I., Fabian, J. & Das Sarma, S. Spintronics: Fundamentals and applications. *Rev. Mod. Phys.* **76**, 323–410 (2004).

27. Zhang, W. *et al.* Ultrafast quenching of electronboson interaction and superconducting gap in a cuprate superconductor. *Nat Commun* **5**, – (2014).

28. Yao, W. *et al.* Direct observation of spin-layer locking by local Rashba effect in monolayer semiconducting PtSe2 film. *Nature Communications* **8**, 14216 (2017).

29. Riley, J. M. *et al.* Direct observation of spin-polarized bulk bands in an inversion-symmetric semiconductor. *Nat Phys* **10**, 835–839 (2014).

30. Dyakonov, M. & Perel, V. Current-induced spin orientation of electrons in semiconductors. *Physics Letters A* **35**, 459–460 (1971).

31. Qi, X.-L. & Zhang, S.-C. The quantum spin Hall effect and topological insulators. *Physics Today* **63**, 33–38 (2010).

32. Sinova, J., Valenzuela, S. O., Wunderlich, J., Back, C. H. & Jungwirth, T. Spin Hall effects. *Rev. Mod. Phys.* **87**, 1213–1260 (2015).

33. Kato, Y. K., Myers, R. C., Gossard, A. C. & Awschalom, D. D. Observation of the Spin Hall Effect in Semiconductors. *Science* **306**, 1910–1913 (2004).

34. Knig, M. *et al.* Quantum Spin Hall Insulator State in HgTe Quantum Wells. *Science* **318**, 766 (2007).

35. Moore, J. E. The birth of topological insulators. *Nature* **464**, 194–198 (2010).

36. Hasan, M. Z. & Kane, C. L. Colloquium: Topological insulators. *Rev. Mod. Phys.* **82**, 3045 (2010).

37. Jozwiak, C. *et al.* Widespread spin polarization effects in photoemission from topological insulators. *Phys. Rev. B* **84**, 165113 (2011).

38. Wolf, S. A. *et al.* Spintronics: A Spin-Based Electronics Vision for the Future. *Science* **294**, 1488 (2001).

39. Datta, S. & Das, B. Electronic analog of the electro-optic modulator. *Appl. Phys. Lett.* **56**, 665–667 (1990).

40. Koo, H. C., Kwon, J. H., Eom, J., Chang, J., Han, S. H. & Johnson, M. Control of Spin Precession in a Spin-Injected Field Effect Transistor. *Science* **325**, 1515–1518 (2009).

41. Wunderlich, J. *et al.* Spin Hall Effect Transistor. *Science* **330**, 1801–1804 (2010).

42. Witczak-Krempa, W., Chen, G., Kim, Y. B. & Balents, L. Correlated Quantum Phenomena in the Strong Spin-Orbit Regime. *Annual Review of Condensed Matter Physics* **5**, 57–82 (2014).

43. Gor'kov, L. P. & Rashba, E. I. Superconducting 2D System with Lifted Spin Degeneracy: Mixed Singlet-Triplet State. *Phys. Rev. Lett.* **87**, 037004 (2001).

44. Veenstra, C. N. *et al.* Spin-Orbital Entanglement and the Breakdown of Singlets and Triplets in Sr_2RuO_4 Revealed by Spin- and Angle-Resolved Photoemission Spectroscopy. *Phys. Rev. Lett.* **112**, 127002 (2014).

45. Stern, A., Dzero, M., Galitski, V. M., Fisk, Z. & Xia, J. Surface-dominated conduction up to 240?K in the Kondo insulator SmB6 under strain. *Nature Materials* **16**, 708 (2017).

46. Nakosai, S., Tanaka, Y. & Nagaosa, N. Topological Superconductivity in Bilayer Rashba System. *Phys. Rev. Lett.* **108**, 147003 (2012).

47. Kargarian, M., Efimkin, D. K. & Galitski, V. Amperean Pairing at the Surface of Topological Insulators. *Phys. Rev. Lett.* **117**, 076806 (2016).

48. Wang, Q. *et al.* Dimensionality-controlled Mott transition and correlation effects in single-layer and bilayer perovskite iridates. *Phys. Rev. B* **87**, 245109 (2013).

49. Fu, L. & Kane, C. L. Superconducting Proximity Effect and Majorana Fermions at the Surface of a Topological Insulator. *Phys. Rev. Lett.* **100**, 096407 (2008).

50. Fujimoto, S. Topological order and non-Abelian statistics in noncentrosymmetric *s*-wave superconductors. *Phys. Rev. B* **77**, 220501 (2008).

51. Sau, J. D., Lutchyn, R. M., Tewari, S. & Das Sarma, S. Generic New Platform for Topological Quantum Computation Using Semiconductor Heterostructures. *Phys. Rev. Lett.* **104**, 040502 (2010).

52. Kim, B. J. *et al.* Novel $J_{\text{eff}} = 1/2$ Mott State Induced by Relativistic Spin-Orbit Coupling in Sr_2IrO_4. *Phys. Rev. Lett.* **101**, 076402 (2008).

53. Jackeli, G. & Khaliullin, G. Mott Insulators in the Strong Spin-Orbit Coupling Limit: From Heisenberg to a Quantum Compass and Kitaev Models. *Phys. Rev. Lett.* **102**, 017205 (2009).

54. Shen, Z.-X. *et al.* Anomalously large gap anisotropy in the a-b plane of $Bi_2Sr_2CaCu_2O_{8+\delta}$. *Phys. Rev. Lett.* **70**, 1553 (1993).

55. Damascelli, A., Hussain, Z. & Shen, Z.-X. Angle-resolved photoemission studies of the cuprate superconductors. *Rev. Mod. Phys.* **75**, 473 (2003).

56. Koralek, J. D. *et al.* Experimental setup for low-energy laser-based angle resolved photoemission spectroscopy. *Review of Scientific Instruments* **78**, 053905 (2007).

57. Perfetti, L., Loukakos, P. A., Lisowski, M., Bovensiepen, U., Eisaki, H. & Wolf, M. Ultrafast Electron Relaxation in Superconducting $Bi_2Sr_2CaCu_2O_{8+\delta}$ by Time-Resolved Photoelectron Spectroscopy. *Phys. Rev. Lett.* **99**, 197001 (2007).

58. Smallwood, C. L., Jozwiak, C., (), W. Z. & Lanzara, A. An ultrafast angle-resolved photoemission apparatus for measuring complex materials. *Review of Scientific Instruments* **83** (2012).

59. Hsieh, D. *et al.* Observation of Unconventional Quantum Spin Textures in Topological Insulators. *Science* **323**, 919–922 (2009).

60. Sobota, J. A. *et al.* Direct Optical Coupling to an Unoccupied Dirac Surface State in the Topological Insulator Bi_2Se_3. *Phys. Rev. Lett.* **111**, 136802– (2013).

61. Jozwiak, C. *et al.* Photoelectron spin-flipping and texture manipulation in a topological insulator. *Nat Phys* **9**, 293–298 (2013).

62. Xu, S.-Y. *et al.* Discovery of a Weyl fermion state with Fermi arcs in niobium arsenide. *Nat Phys* **11**, 748–754 (2015).

63. Jozwiak, C. *et al.* Spin-polarized surface resonances accompanying topological surface state formation **7**, 13143 (2016).

64. Bostwick, A., Ohta, T., Seyller, T., Horn, K. & Rotenberg, E. Quasiparticle dynamics in graphene. *Nat. Phys.* **3**, 36 (2007).

65. Zhou, S. Y. *et al.* Substrate-induced bandgap opening in epitaxial graphene. *Nat. Mater.* **6**, 770 (2007).

66. Liu, C. *et al.* Spin-correlated electronic state on the surface of a spin-orbit Mott system. *Phys. Rev. B* **90**, 045127 (2014).

67. Yi, M. *et al.* Observation of universal strong orbital-dependent correlation effects in iron chalcogenides **6**, 7777 (2015).

68. Affeldt, G. *et al.* Spectral weight suppression near a metal-insulator transition in a double-layer electron-doped iridate. *Phys. Rev. B* **95**, 235151 (2017).

69. Ishizaka, K. *et al.* Giant Rashba-type spin splitting in bulk BiTeI. *Nat Mater* **10**, 521–526 (2011).

70. Koralek, J. D. *et al.* Laser Based Angle-Resolved Photoemission, the Sudden Approximation, and Quasiparticle-Like Spectral Peaks in $Bi_2Sr_2CaCu_2O_{8+\delta}$. *Phys. Rev. Lett.* **96**, 017005 (2006).

71. Lanzara, A. *et al.* Evidence for ubiquitous strong electron-phonon coupling in high-temperature superconductors. *Nature* **412**, 510 (2001).

72. Valla, T., Fedorov, A. V., Johnson, P. D. & Hulbert, S. L. Many-Body Effects in Angle-Resolved Photoemission: Quasiparticle Energy and Lifetime of a Mo(110) Surface State. *Phys. Rev. Lett.* **83**, 2085–2088 (1999).

73. Einstein, A. ber einen die Erzeugung und Verwandlung des Lichtes betreffenden heuristischen Gesichtspunkt. *Ann. Phys. (Leipzig)* **322**, 132 (1905).

74. Damascelli, A. Probing the Electronic Structure of Complex Systems by ARPES. *Physica Scripta* **2004**, 61 (2004).

75. Cao, Y. *et al.* Mapping the orbital wavefunction of the surface states in three-dimensional topological insulators. *Nat Phys* **9**, 499–504 (2013).

76. Zhu, Z.-H. *et al.* Photoelectron Spin-Polarization Control in the Topological Insulator Bi_2Se_3. *Phys. Rev. Lett.* **112**, 076802 (2014).

77. Chuang, Y. D. *et al.* Bilayer splitting and coherence effects in optimal and underdoped $Bi_2Sr_2CaCu_2O_{8+\delta}$. *Phys. Rev. B* **69**, 094515 (2004).

78. Borisenko, S. V. *et al.* Kinks, Nodal Bilayer Splitting, and Interband Scattering in $YBa_2Cu_3O_{6+x}$. *Phys. Rev. Lett.* **96**, 117004 (2006).

79. Yamasaki, T. *et al.* Unmasking the nodal quasiparticle dynamics in cuprate superconductors using low-energy photoemission. *Phys. Rev. B* **75**, 140513 (2007).

80. Smallwood, C. L. *et al.* Tracking Cooper Pairs in a Cuprate Superconductor by Ultrafast Angle-Resolved Photoemission. *Science* **336**, 1137–1139 (2012).

81. Zhou, S. Y. *et al.* First direct observation of Dirac fermions in graphite. *Nat. Phys.* **2**, 595 (2006).

82. Kisker, E., Schrder, K., Campagna, M. & Gudat, W. Temperature Dependence of the Exchange Splitting of Fe by Spin-Resolved Photoemission Spectroscopy with Synchrotron Radiation. *Phys. Rev. Lett.* **52**, 2285 (1984).

83. Fedorov, A. V., Valla, T., Liu, F., Johnson, P. D., Weinert, M. & Allen, P. B. Spin-resolved photoemission study of photohole lifetimes in ferromagnetic gadolinium. *Phys. Rev. B* **65**, 212409 (2002).

84. Sánchez-Barriga, J. *et al.* Strength of Correlation Effects in the Electronic Structure of Iron. *Phys. Rev. Lett.* **103**, 267203 (2009).

85. Shikin, A. M. *et al.* Origin of Spin-Orbit Splitting for Monolayers of Au and Ag on W(110) and Mo(110). *Phys. Rev. Lett.* **100**, 057601 (2008).

86. Varykhalov, A. *et al.* Electronic and Magnetic Properties of Quasifreestanding Graphene on Ni. *Phys. Rev. Lett.* **101**, 157601 (2008).

87. Varykhalov, A., Sanchez-Barriga, J., Shikin, A. M., Gudat, W., Eberhardt, W. & Rader, O. Quantum Cavity for Spin due to Spin-Orbit Interaction at a Metal Boundary. *Phys. Rev. Lett.* **101**, 256601 (2008).

88. Miyamoto, K. *et al.* Spin-Polarized Dirac-Cone-Like Surface State with *d* Character at W(110). *Phys. Rev. Lett.* **108**, 066808 (2012).

89. Hsieh, D. *et al.* A tunable topological insulator in the spin helical Dirac transport regime. *Nature* **460**, 1101–1105 (2009).

90. Nishide, A. *et al.* Direct mapping of the spin-filtered surface bands of a three-dimensional quantum spin Hall insulator. *Phys. Rev. B* **81**, 041309 (2010).

91. Hirahara, T. *et al.* Anomalous transport in an n -type topological insulator ultrathin Bi_2Se_3 film. *Phys. Rev. B* **82**, 155309 (2010).

92. Xu, S.-Y. *et al.* Topological Phase Transition and Texture Inversion in a Tunable Topological Insulator. *Science* **332**, 560–564 (2011).

93. Souma, S. *et al.* Direct Measurement of the Out-of-Plane Spin Texture in the Dirac-Cone Surface State of a Topological Insulator. *Phys. Rev. Lett.* **106**, 216803 (2011).

94. Pan, Z.-H. *et al.* Electronic Structure of the Topological Insulator Bi2Se3 Using Angle-Resolved Photoemission Spectroscopy: Evidence for a Nearly Full Surface Spin Polarization. *Phys. Rev. Lett.* **106**, 257004 (2011).

95. Miyamoto, K. *et al.* Topological Surface States with Persistent High Spin Polarization across the Dirac Point in Bi_2Te_2Se and Bi_2Se_2Te. *Phys. Rev. Lett.* **109**, 166802 (2012).

96. Okamoto, K. *et al.* Observation of a highly spin-polarized topological surface state in $GeBi_2Te_4$. *Phys. Rev. B* **86**, 195304 (2012).

97. Schmitt, F. *et al.* Transient Electronic Structure and Melting of a Charge Density Wave in $TbTe_3$. *Science* **321**, 1649 (2008).

98. Rameau, J. D. *et al.* Photoinduced changes in the cuprate electronic structure revealed by femtosecond time- and angle-resolved photoemission. *Phys. Rev. B* **89**, 115115 (2014).

99. Petersen, J. C. *et al.* Clocking the Melting Transition of Charge and Lattice Order in $1T$-TaS_2 with Ultrafast Extreme-Ultraviolet Angle-Resolved Photoemission Spectroscopy. *Phys. Rev. Lett.* **107**, 177402 (2011).

100. Smallwood, C. L., Zhang, W., Miller, T. L., Jozwiak, C., Eisaki, H., Lee, D.-H. & Lanzara, A. Time- and momentum-resolved gap dynamics in $Bi_2Sr_2CaCu_2O_{8+\delta}$. *Phys. Rev. B* **89**, 115126 (2014).

101. Smallwood, C. L. *et al.* Influence of optically quenched superconductivity on quasiparticle relaxation rates in $Bi_2Sr_2CaCu_2O_{8+\delta}$. *Phys. Rev. B* **92**, 161102 (2015).

102. Wang, Y. H., Steinberg, H., Jarillo-Herrero, P. & Gedik, N. Observation of Floquet-Bloch States on the Surface of a Topological Insulator. *Science* **342**, 453–457 (2013).

103. Mahmood, F., Chan, C.-K., Alpichshev, Z., Gardner, D., Lee, Y., Lee, P. A. & Gedik, N. Selective scattering between Floquet-Bloch and Volkov states in a topological insulator. *Nature Physics* **12**, 306 (2016).

104. Carpene, E., Mancini, E., Dallera, C., Ghiringhelli, G., Manzoni, C., Cerullo, G. & De Silvestri, S. A versatile apparatus for time-resolved photoemission spectroscopy via femtosecond pump-probe experiments. *Review of Scientific Instruments* **80** (2009).

105. Faure, J., Mauchain, J., Papalazarou, E., Yan, W., Pinon, J., Marsi, M. & Perfetti, L. Full characterization and optimization of a femtosecond ultraviolet laser source for time and angle-resolved photoemission on solid surfaces. *Rev. Sci. Instrum.* **83**, 043109–7 (2012).

106. Smallwood, C. L., Jozwiak, C., Zhang, W. & Lanzara, A. An ultrafast angle-resolved photoemission apparatus for measuring complex materials. *Rev. Sci. Instrum.* **83**, 123904–6 (2012).

107. Rossnagel, K. Shooting Electronic Structure Movies with Time-resolved Photoemission. *Synchrotron Radiation News* **25**, 12–18 (2012).

108. Ishida, Y. *et al.* Time-resolved photoemission apparatus achieving sub-20-meV energy resolution and high stability. *Review of Scientific Instruments* **85** (2014).

109. Boschini, F. *et al.* An innovative Yb-based ultrafast deep ultraviolet source for time-resolved photoemission experiments. *Review of Scientific Instruments* **85** (2014).

110. Cilento, F. *et al.* Advancing non-equilibrium {ARPES} experiments by a 9.3 eV coherent ultrafast photon source. *Journal of Electron Spectroscopy and Related Phenomena* **207**, 7 – 13 (2016).

111. Hajlaoui, M. *et al.* Ultrafast Surface Carrier Dynamics in the Topological Insulator Bi2Te3. *Nano Letters* **12**, 3532–3536 (2012).

112. Wang, Y. H. *et al.* Measurement of Intrinsic Dirac Fermion Cooling on the Surface of the Topological Insulator Bi_2Se_3 Using Time-Resolved and Angle-Resolved Photoemission Spectroscopy. *Phys. Rev. Lett.* **109**, 127401 (2012).

113. Gierz, I. *et al.* Snapshots of non-equilibrium Dirac carrier distributions in graphene. *Nat Mater* **12**, 1119–1124 (2013).

114. Miller, T. L., Smallwood, C. L., Zhang, W., Eisaki, H., Orenstein, J. & Lanzara, A. Photoinduced changes of the chemical potential in superconducting$Bi_2Sr_2CaCu_2O_{8+\delta}$. *Phys. Rev. B* **92**, 144506 (2015).

115. Aeschlimann, M., Bauer, M., Pawlik, S., Weber, W., Burgermeister, R., Oberli, D. & Siegmann, H. C. Ultrafast Spin-Dependent Electron Dynamics in fcc Co. *Phys. Rev. Lett.* **79**, 5158 (1997).

116. Aeschlimann, M., Burgermeister, R., Pawlik, S., Bauer, M., Oberli, D. & Weber, W. Spin-dependent electron dynamics investigated by means of time- and spin-resolved photoemission. *J. Electron Spectrosc. Relat. Phenom.* **88-91**, 179 (1998).

117. Cinchetti, M. *et al.* Spin-Flip Processes and Ultrafast Magnetization Dynamics in Co: Unifying the Microscopic and Macroscopic View of Femtosecond Magnetism. *Phys. Rev. Lett.* **97**, 177201 (2006).

118. Schmidt, A. B. *et al.* Ultrafast Magnon Generation in an Fe Film on Cu(100). *Phys. Rev. Lett.* **105**, 197401 (2010).

119. Goris, A., Döbrich, K. M., Panzer, I., Schmidt, A. B., Donath, M. & Weinelt, M. Role of Spin-Flip Exchange Scattering for Hot-Electron Lifetimes in Cobalt. *Phys. Rev. Lett.* **107**, 026601 (2011).

120. Weber, A., Pressacco, F., Günther, S., Mancini, E., Oppeneer, P. M. & Back, C. H. Ultrafast demagnetization dynamics of thin Fe/W(110) films: Comparison of time- and spin-resolved photoemission with time-resolved magneto-optic experiments. *Phys. Rev. B* **84**, 132412 (2011).

121. Roth, C., Hillebrecht, F. U., Park, W. G., Rose, H. B. & Kisker, E. Spin Polarization in Cu Core-Level Photoemission with Linearly Polarized Soft X Rays. *Phys. Rev. Lett.* **73**, 1963 (1994).

122. Rose, H. B., Fanelsa, A., Kinoshita, T., Roth, C., Hillebrecht, F. U. & Kisker, E. Spin-orbit-induced spin polarization in W 4f photoemission. *Phys. Rev. B* **53**, 1630 (1996).

123. Yu, S.-W. & Tobin, J. G. Breakdown of spatial inversion symmetry in core-level photoemission of Pt(001). *Phys. Rev. B* **77**, 193409 (2008).

124. Nishitani, T. *et al.* Highly polarized electrons from GaAs-GaAsP and InGaAs-AlGaAs strained-layer superlattice photocathodes. *Journal Of Applied Physics* **97**, 094907 (2005).

125. Cherepkov, N. A. Spin polarisation of photoelectrons ejected from unpolarised atoms. *Journal of Physics B: Atomic and Molecular Physics* **12**, 1279 (1979).

126. Iori, K. *et al.* The self-calibration of a retarding-type Mott spin polarimeter with a large collection angle. *Review of Scientific Instruments* **77**, 013101 (2006).

127. Okuda, T., Takeichi, Y., Maeda, Y., Harasawa, A., Matsuda, I., Kinoshita, T. & Kakizaki, A. A new spin-polarized photoemission spectrometer with very high efficiency and energy resolution. *Rev. Sci. Instrum.* **79**, 123117–5 (2008).

128. Moreschini, L., Ghiringhelli, G., Larsson, K., Veit, U. & Brookes, N. B. A time-of-flight–Mott apparatus for soft x-ray spin resolved photoemission on solid samples. *Rev. Sci. Instrum.* **79**, 033905 (2008).

129. Cacho, C. M., Vlaic, S., Malvestuto, M., Ressel, B., Seddon, E. A. & Parmigiani, F. Absolute spin calibration of an electron spin polarimeter by spin-resolved photoemission from the Au(111) surface states. *Rev. Sci. Instrum.* **80**, 043904–4 (2009).

130. Meier, F., Dil, J. H. & Osterwalder, J. Measuring spin polarization vectors in angle-resolved photoemission spectroscopy. *New Journal of Physics* **11**, 125008 (2009).

131. Souma, S., Takayama, A., Sugawara, K., Sato, T. & Takahashi, T. Ultrahigh-resolution spin-resolved photoemission spectrometer with a mini Mott detector. *Review of Scientific Instruments* **81**, 095101 (2010).

132. Berntsen, M. H. *et al.* A spin- and angle-resolving photoelectron spectrometer. *Review of Scientific Instruments* **81**, 035104 (2010).

133. Okuda, T., Miyamaoto, K., Miyahara, H., Kuroda, K., Kimura, A., Namatame, H. & Taniguchi, M. Efficient spin resolved spectroscopy observation machine at Hiroshima Synchrotron Radiation Center. *Review of Scientific Instruments* **82**, 103302 (2011).

134. Kolbe, M. *et al.* Highly Efficient Multichannel Spin-Polarization Detection. *Phys. Rev. Lett.* **107**, 207601 (2011).

135. Kutnyakhov, D. *et al.* Imaging spin filter for electrons based on specular reflection from iridium (001). *Ultramicroscopy* **130**, 63 – 69 (2013).

136. Jozwiak, C. *et al.* A high-efficiency spin-resolved photoemission spectrometer combining time-of-flight spectroscopy with exchange-scattering polarimetry. *Rev. Sci. Instrum.* **81**, 053904 (2010).

137. Qiao, S., Kimura, A., Harasawa, A., Sawada, M., Chung, J.-G. & Kakizaki, A. A new compact electron spin polarimeter with a high efficiency. *Review of Scientific Instruments* **68**, 4390–4395 (1997).

138. Petrov, V. N., Galaktionov, M. S. & Kamochkin, A. S. Comparative tests of conventional and retarding-potential Mott polarimeters. *Review of Scientific Instruments* **72**, 3728–3730 (2001).

139. Neufeld, D. D., Aliabadi, H. & Dunning, F. B. Compact retarding-potential Mott polarimeter. *Rev. Sci. Instrum.* **78**, 025107 (2007).

140. Bertacco, R., Marcon, M., Trezzi, G., Duo, L. & Ciccacci, F. Spin and energy analysis of electron beams: Coupling a polarimeter based on exchange scattering to a hemispherical analyzer. *Rev. Sci. Instrum.* **73**, 3867 (2002).

141. Hillebrecht, F. U. *et al.* High-efficiency spin polarimetry by very-low-energy electron scattering from Fe(100) for spin-resolved photoemission. *Rev. Sci. Instrum.* **73**, 1229 (2002).

142. Gay, T. J. & Dunning, F. B. Mott electron polarimetry. *Rev. Sci. Instrum.* **63**, 1635 (1992).

143. Getzlaff, M., Heidemann, B., Bansmann, J., Westphal, C. & Schonhense, G. A variable-angle electron spin polarization detection system. *Rev. Sci. Instrum.* **69**, 3913–3923 (1998).

144. Winkelmann, A., Hartung, D., Engelhard, H., Chiang, C.-T. & Kirschner, J. High efficiency electron spin polarization analyzer based on exchange scattering at Fe/W(001). *Rev. Sci. Instrum.* **79**, 083303–6 (2008).

145. Tusche, C. *et al.* Spin resolved photoelectron microscopy using a two-dimensional spin-polarizing electron mirror. *Applied Physics Letters* **99**, 032505 (2011).

146. Tusche, C. *et al.* Quantitative spin polarization analysis in photoelectron emission microscopy with an imaging spin filter. *Ultramicroscopy* **130**, 70 – 76 (2013).

147. Kiss, T. *et al.* A versatile system for ultrahigh resolution, low temperature, and polarization dependent Laser-angle-resolved photoemission spectroscopy. *Review of Scientific Instruments* **79**, 023106 (2008).

148. Liu, G. *et al.* Development of a vacuum ultraviolet laser-based angle-resolved photoemission system with a superhigh energy resolution better than 1 meV. *Rev. Sci. Instrum.* **79**, 023105–11 (2008).

149. Zhang, W. *et al.* Identification of a New Form of Electron Coupling in the $Bi_2Sr_2CaCu_2O_8$ Superconductor by Laser-Based Angle-Resolved Photoemission Spectroscopy. *Phys. Rev. Lett.* **100**, 107002 (2008).

150. Vishik, I. M. *et al.* Doping-Dependent Nodal Fermi Velocity of the High-Temperature Superconductor $Bi_2Sr_2CaCu_2O_{8+\delta}$ Revealed Using High-Resolution Angle-Resolved Photoemission Spectroscopy. *Phys. Rev. Lett.* **104**, 207002 (2010).

151. Wang, Y. H., Hsieh, D., Pilon, D., Fu, L., Gardner, D. R., Lee, Y. S. & Gedik, N. Observation of a Warped Helical Spin Texture in Bi_2Se_3 from Circular Dichroism Angle-Resolved Photoemission Spectroscopy. *Phys. Rev. Lett.* **107**, 207602– (2011).

152. Chen, C. *et al.* Robustness of topological order and formation of quantum well states in topological insulators exposed to ambient environment. *Proceedings of the National Academy of Sciences* **109**, 3694–3698 (2012).

153. Graf, J., Jozwiak, C., Smallwood, C. L., Eisaki, H., Kaindl, R. A., Lee, D.-H. & Lanzara, A. Nodal quasiparticle meltdown in ultrahigh-resolution pump-probe angle-resolved photoemission. *Nat Phys* **7**, 805–809 (2011).

154. Rohwer, T. *et al.* Collapse of long-range charge order tracked by time-resolved photoemission at high momenta. *Nature* **471**, 490–493 (2011).

155. Rettig, L. *et al.* Ultrafast Momentum-Dependent Response of Electrons in Antiferromagnetic $EuFe_2As_2$ Driven by Optical Excitation. *Phys. Rev. Lett.* **108**, 097002 (2012).

156. Sobota, J. A., Yang, S., Analytis, J. G., Chen, Y. L., Fisher, I. R., Kirchmann, P. S. & Shen, Z.-X. Ultrafast Optical Excitation of a Persistent Surface-State Population in the Topological Insulator Bi_2Se_3. *Phys. Rev. Lett.* **108**, 117403– (2012).

157. Kummer, K. *et al.* Ultrafast quasiparticle dynamics in the heavy-fermion compound $YbRh_2Si_2$. *Phys. Rev. B* **86**, 085139 (2012).

158. Souma, S., Sato, T., Takahashi, T. & Baltzer, P. High-intensity xenon plasma discharge lamp for bulk-sensitive high-resolution photoemission spectroscopy. *Review of Scientific Instruments* **78**, 123104 (2007).

159. He, Y. *et al.* Invited Article: High resolution angle resolved photoemission with tabletop 11 eV laser. *Review of Scientific Instruments* **87**, 011301 (2016).

160. Wang, H., Xu, Y., Ulonska, S., Robinson, J. S., Ranitovic, P. & Kaindl, R. A. Bright high-repetition-rate source of narrowband extreme-ultraviolet harmonics beyond 22 eV **6**, 7459 (2015).

161. Kirchmann, P., Rettig, L., Nandi, D., Lipowski, U., Wolf, M. & Bovensiepen, U. A time-of-flight spectrometer for angle-resolved detection of low energy electrons in two dimensions. *Applied Physics A* **91**, 211–217 (2008).

162. Casey, P. A., Koralek, J. D., Plumb, N. C., Dessau, D. S. & Anderson, P. W. Accurate theoretical fits to laser-excited photoemission spectra in the normal phase of high-temperature superconductors. *Nat Phys* **4**, 210–212 (2008).

163. Hüfner, S. *Photoelectron Spectroscopy: Principles and applications* (Springer-Verlag, 2003), 3rd edn.

164. Seah, M. P. & Dench, W. A. Quantitative electron spectroscopy of surfaces: A standard data base for electron inelastic mean free paths in solids. *Surface and Interface Analysis* **1**, 2–11 (1979).

165. Hemmers, O., Whitfield, S. B., Glans, P., Wang, H., Lindle, D. W., Wehlitz, R. & Sellin, I. A. High-resolution electron time-of-flight apparatus for the soft x-ray region. *Rev. Sci. Instrum.* **69**, 3809 (1998).

166. Xu, S.-Y. *et al.* Hedgehog spin texture and Berry/'s phase tuning in a magnetic topological insulator. *Nat Phys* **8**, 616–622 (2012).

167. Takayama, A., Sato, T., Souma, S. & Takahashi, T. Giant Out-of-Plane Spin Component and the Asymmetry of Spin Polarization in Surface Rashba States of Bismuth Thin Film. *Phys. Rev. Lett.* **106**, 166401 (2011).

168. Takayama, A., Sato, T., Souma, S., Oguchi, T. & Takahashi, T. Tunable Spin Polarization in Bismuth Ultrathin Film on Si(111). *Nano Letters* **12**, 1776–1779 (2012).

169. Park, J.-H., Vescovo, E., Kim, H.-J., Kwon, C., Ramesh, R. & Venkatesan, T. Magnetic Properties at Surface Boundary of a Half-Metallic Ferromagnet $La_{0.7}Sr_{0.3}MnO_3$. *Phys. Rev. Lett.* **81**, 1953 (1998).

170. Beaurepaire, E., Merle, J.-C., Daunois, A. & Bigot, J.-Y. Ultrafast Spin Dynamics in Ferromagnetic Nickel. *Phys. Rev. Lett.* **76**, 4250–4253 (1996).

171. Vahaplar, K. *et al.* Ultrafast Path for Optical Magnetization Reversal via a Strongly Nonequilibrium State. *Phys. Rev. Lett.* **103**, 117201 (2009).

172. Kimel, A. V., Kirilyuk, A., Hansteen, F., Pisarev, R. V. & Rasing, T. Nonthermal optical control of magnetism and ultrafast laser-induced spin dynamics in solids. *Journal of Physics: Condensed Matter* **19**, 043201 (2007).

173. Hsieh, D., Mahmood, F., McIver, J. W., Gardner, D. R., Lee, Y. S. & Gedik, N. Selective Probing of Photoinduced Charge and Spin Dynamics in the Bulk and Surface of a Topological Insulator. *Phys. Rev. Lett.* **107**, 077401 (2011).

174. Crepaldi, A. *et al.* Ultrafast photodoping and effective Fermi-Dirac distribution of the Dirac particles in Bi_2Se_3. *Phys. Rev. B* **86**, 205133 (2012).

175. Cacho, C. *et al.* Momentum-Resolved Spin Dynamics of Bulk and Surface Excited States in the Topological Insulator Bi_2Se_3. *Phys. Rev. Lett.* **114**, 097401 (2015).

176. Sánchez-Barriga, J. *et al.* Ultrafast spin-polarization control of Dirac fermions in topological insulators. *Phys. Rev. B* **93**, 155426 (2016).

177. Cortés, R., Rettig, L., Yoshida, Y., Eisaki, H., Wolf, M. & Bovensiepen, U. Momentum-Resolved Ultrafast Electron Dynamics in Superconducting $Bi_2Sr_2CaCu_2O_{8+\delta}$. *Phys. Rev. Lett.* **107**, 097002 (2011).

178. Yang, S.-L., Sobota, J. A., Kirchmann, P. S. & Shen, Z.-X. Electron propagation from a photo-excited surface: implications for time-resolved photoemission. *Applied Physics A* **116**, 85–90 (2013).

179. Qi, X.-L. & Zhang, S.-C. Topological insulators and superconductors. *Rev. Mod. Phys.* **83**, 1057–1110 (2011).

180. Awschalom, D. D. & Flatte, M. E. Challenges for semiconductor spintronics. *Nat Phys* **3**, 153–159 (2007).

181. Wu, C. & Zhang, S.-C. Dynamic Generation of Spin-Orbit Coupling. *Phys. Rev. Lett.* **93**, 036403– (2004).

182. Zhang, H., Liu, C.-X., Qi, X.-L., Dai, X., Fang, Z. & Zhang, S.-C. Topological insulators in Bi2Se3, Bi2Te3 and Sb2Te3 with a single Dirac cone on the surface. *Nat Phys* **5**, 438–442 (2009).

183. Xia, Y. *et al.* Observation of a large-gap topological-insulator class with a single Dirac cone on the surface. *Nat Phys* **5**, 398–402 (2009).

184. Chen, Y. L. *et al.* Experimental Realization of a Three-Dimensional Topological Insulator, Bi_2Te_3. *Science* **325**, 178–181 (2009).

185. Wray, L. A. *et al.* A topological insulator surface under strong Coulomb, magnetic and disorder perturbations. *Nat Phys* **7**, 32–37 (2011).

186. Nicolay, G., Reinert, F., Hüfner, S. & Blaha, P. Spin-orbit splitting of the L-gap surface state on Au(111) and Ag(111). *Phys. Rev. B* **65**, 033407 (2001).

187. Park, C.-H. & Louie, S. G. Spin Polarization of Photoelectrons from Topological Insulators. *Phys. Rev. Lett.* **109**, 097601 (2012).

188. Zhang, H., Liu, C.-X. & Zhang, S.-C. Spin-Orbital Texture in Topological Insulators. *Phys. Rev. Lett.* **111**, 066801– (2013).

189. Ryoo, J. H. & Park, C.-H. Spin-conserving and reversing photoemission from the surface states of Bi_2Se_3 and Au (111). *Phys. Rev. B* **93**, 085419 (2016).

190. Zhu, Z.-H. *et al.* Layer-By-Layer Entangled Spin-Orbital Texture of the Topological Surface State in Bi_2Se_3. *Phys. Rev. Lett.* **110**, 216401– (2013).

191. Xie, Z. *et al.* Orbital-selective spin texture and its manipulation in a topological insulator. *Nat Commun* **5**, 3382 (2014).

192. Mirhosseini, H. *et al.* Unconventional spin topology in surface alloys with Rashba-type spin splitting. *Phys. Rev. B* **79**, 245428 (2009).

193. Wissing, S. N. P., Schmidt, A. B., Mirhosseini, H., Henk, J., Ast, C. R. & Donath, M. Ambiguity of Experimental Spin Information from States with Mixed Orbital Symmetries. *Phys. Rev. Lett.* **113**, 116402 (2014).

194. Mirhosseini, H., Flieger, M. & Henk, J. Dirac-cone-like surface state in W(110): dispersion, spin texture and photoemission from first principles. *New Journal of Physics* **15**, 033019 (2013).

195. Miyamoto, K. *et al.* Orbital-symmetry-selective spin characterization of Dirac-cone-like state on W(110). *Phys. Rev. B* **93**, 161403 (2016).

196. Maaß, H. *et al.* Spin-texture inversion in the giant Rashba semiconductor BiTeI. *Nat Commun* **7**, – (2016).

197. Sugawara, K., Sato, T., Souma, S., Takahashi, T., Arai, M. & Sasaki, T. Fermi Surface and Anisotropic Spin-Orbit Coupling of Sb(111) Studied by Angle-Resolved Photoemission Spectroscopy. *Phys. Rev. Lett.* **96**, 046411 (2006).

198. Kadono, T. *et al.* Direct evidence of spin-polarized band structure of Sb(111) surface. *Applied Physics Letters* **93**, – (2008).

199. Bian, G., Miller, T. & Chiang, T.-C. Passage from Spin-Polarized Surface States to Unpolarized Quantum Well States in Topologically Nontrivial Sb Films. *Phys. Rev. Lett.* **107**, 036802– (2011).

200. Bianchi, M. *et al.* Surface states on a topologically nontrivial semimetal: The case of Sb(110). *Phys. Rev. B* **85**, 155431 (2012).

201. Takayama, A., Sato, T., Souma, S. & Takahashi, T. Rashba effect in antimony and bismuth studied by spin-resolved ARPES. *New Journal of Physics* **16**, 055004 (2014).

202. Kuroda, K. *et al.* Coherent control over three-dimensional spin polarization for the spin-orbit coupled surface state of Bi_2Se_3. *Phys. Rev. B* **94**, 165162 (2016).

203. Wortelen, H., Mirhosseini, H., Miyamoto, K., Schmidt, A. B., Henk, J. & Donath, M. Tuning the spin signal from a highly symmetric unpolarized electronic state. *Phys. Rev. B* **91**, 115420 (2015).

204. Giannozzi, P. *et al.* QUANTUM ESPRESSO: a modular and open-source software project for quantum simulations of materials. *Journal of Physics: Condensed Matter* **21**, 395502 (2009).

205. Perdew, J. P. & Zunger, A. Self-interaction correction to density-functional approximations for many-electron systems. *Phys. Rev. B* **23**, 5048–5079 (1981).

206. Mostofi, A. A., Yates, J. R., Lee, Y.-S., Souza, I., Vanderbilt, D. & Marzari, N. wannier90: A tool for obtaining maximally-localised Wannier functions. *Computer Physics Communications* **178**, 685 – 699 (2008).

207. Sánchez-Barriga, J. *et al.* Photoemission of Bi_2Se_3 with Circularly Polarized Light: Probe of Spin Polarization or Means for Spin Manipulation? *Phys. Rev. X* **4**, 011046 (2014).

208. Fu, L. Hexagonal Warping Effects in the Surface States of the Topological Insulator Bi_2Te_3. *Phys. Rev. Lett.* **103**, 266801 (2009).

209. Coffey, D., Rice, T. M. & Zhang, F. C. Dzyaloshinskii-Moriya interaction in the cuprates. *Phys. Rev. B* **44**, 10112–10116 (1991).

210. Koshibae, W., Ohta, Y. & Maekawa, S. Electronic and magnetic structures of cuprates with spin-orbit interaction. *Phys. Rev. B* **47**, 3391–3400 (1993).

211. Edelstein, V. M. Magnetoelectric Effect in Polar Superconductors. *Phys. Rev. Lett.* **75**, 2004–2007 (1995).

212. Wu, C., Zaanen, J. & Zhang, S.-C. Spin-Orbit Coupling-Induced Magnetic Phase in the d-Density-Wave Phase of $La_{2-x}Ba_xCuO_4$ Superconductors. *Phys. Rev. Lett.* **95**, 247007 (2005).

213. Harrison, N., Ramshaw, B. J. & Shekhter, A. Nodal bilayer-splitting controlled by spin-orbit interactions in underdoped high-Tc cuprates. *Scientific Reports* **5**, 10914 (2015).

214. Pesin, D. & Balents, L. Mott physics and band topology in materials with strong spin-orbit interaction. *Nat Phys* **6**, 376–381 (2010).

215. Rau, J. G., Lee, E. K.-H. & Kee, H.-Y. Spin-Orbit Physics Giving Rise to Novel Phases in Correlated Systems: Iridates and Related Materials. *Annual Review of Condensed Matter Physics* **7**, 195–221 (2016).

216. Xu, N. *et al.* Direct observation of the spin texture in SmB6 as evidence of the topological Kondo insulator. *Nature Communications* **5**, 4566 (2014).

217. Bednorz, J. G. & Mller, K. A. Possible highTc superconductivity in the BaLaCuO system. *Z. Phys. B* **64**, 189 (1986).

218. Norman, M. R. The Challenge of Unconventional Superconductivity. *Science* **332**, 196–200 (2011).

219. Gavaler, J. R. Superconductivity in Nb-Ge films above 22 K. *Appl. Phys. Lett.* **23**, 480–482 (1973).

220. Wu, M. K. *et al.* Superconductivity at 93 K in a new mixed-phase Y-Ba-Cu-O compound system at ambient pressure. *Phys. Rev. Lett.* **58**, 908–910 (1987).

221. Bardeen, J., Cooper, L. N. & Schrieffer, J. R. Theory of Superconductivity. *Phys. Rev.* **108**, 1175–1204 (1957).

222. Marshall, D. S. *et al.* Unconventional Electronic Structure Evolution with Hole Doping in $Bi_2Sr_2CaCu_2O_{8+\delta}$: Angle-Resolved Photoemission Results. *Phys. Rev. Lett.* **76**, 4841–4844 (1996).

223. Ding, H. *et al.* Electronic Excitations in $Bi_2Sr_2CaCu_2O_8$: Fermi Surface, Dispersion, and Absence of Bilayer Splitting. *Phys. Rev. Lett.* **76**, 1533 (1996).

224. Loeser, A. G., Shen, Z.-X., Dessau, D. S., Marshall, D. S., Park, C. H., Fournier, P. & Kapitulnik, A. Excitation Gap in the Normal State of Underdoped Bi2Sr2CaCu2O8+? *Science* **273**, 325–329 (1996).

225. Chen, C. H., Cheong, S.-W. & Cooper, A. S. Charge modulations in $La_{2-x}Sr_xNiO_{4+y}$: Ordering of polarons. *Phys. Rev. Lett.* **71**, 2461–2464 (1993).

226. Tranquada, J. M., Buttrey, D. J., Sachan, V. & Lorenzo, J. E. Simultaneous Ordering of Holes and Spins in $La_2NiO_{4.125}$. *Phys. Rev. Lett.* **73**, 1003–1006 (1994).

227. Comin, R. *et al.* Charge Order Driven by Fermi-Arc Instability in Bi2Sr2-xLaxCuO6+? *Science* **343**, 390–392 (2014).

228. Bianconi, A., Lusignoli, M., Saini, N. L., Bordet, P., Kvick, A. & Radaelli, P. G. Stripe structure of the CuO_2 plane in $Bi_2Sr_2CaCu_2O_{8+y}$ by anomalous x-ray diffraction. *Phys. Rev. B* **54**, 4310–4314 (1996).

229. Saini, N. L. *et al.* Topology of the Pseudogap and Shadow Bands in $Bi_2Sr_2CaCu_2O_{8+\delta}$ at Optimum Doping. *Phys. Rev. Lett.* **79**, 3467–3470 (1997).

230. Suh, B. J., Hammel, P. C., Hücker, M. & Büchner, B. Local magnetic and structural properties of the low-temperature orthorhombic to low-temperature tetragonal transition: A ^{139}La NQR study in lightly hole-doped $La_{1.8-x}Eu_{0.2}Sr_xCuO_4$. *Phys. Rev. B* **59**, R3952–R3955 (1999).

231. Kamihara, Y., Watanabe, T., Hirano, M. & Hosono, H. Iron-Based Layered Superconductor La[O1-xFx]FeAs (x = 0.05?0.12) with Tc = 26 K. *Journal of the American Chemical Society* **130**, 3296–3297 (2008). PMID: 18293989.

232. Anderson, P. W. The Resonating Valence Bond State in La2CuO4 and Superconductivity. *Science* **235**, 1196–1198 (1987).

233. Le Tacon, M. *et al.* Intense paramagnon excitations in a large family of high-temperature superconductors. *Nat Phys* **7**, 725–730 (2011).

234. Chakravarty, S., Laughlin, R. B., Morr, D. K. & Nayak, C. Hidden order in the cuprates. *Phys. Rev. B* **63**, 094503 (2001).

235. Xia, J. *et al.* Polar Kerr-Effect Measurements of the High-Temperature $YBa_2Cu_3O_{6+x}$ Superconductor: Evidence for Broken Symmetry near the Pseudogap Temperature. *Phys. Rev. Lett.* **100**, 127002 (2008).

236. Aji, V. & Varma, C. M. Spin order accompanying loop-current order in cuprate superconductors. *Phys. Rev. B* **75**, 224511 (2007).

237. Zhang, X., Liu, Q., Luo, J.-W., Freeman, A. J. & Zunger, A. Hidden spin polarization in inversion-symmetric bulk crystals. *Nat Phys* **10**, 387–393 (2014).

238. De Luca, G. M. *et al.* Weak magnetism in insulating and superconducting cuprates. *Phys. Rev. B* **82**, 214504 (2010).

239. To be published (????).

240. Yada, K., Onari, S., Tanaka, Y. & Inoue, J.-i. Electrically controlled superconducting states at the heterointerface $SrTiO_3/LaAlO_3$. *Phys. Rev. B* **80**, 140509 (2009).

241. Maruyama, D., Sigrist, M. & Yanase, Y. Locally Non-centrosymmetric Superconductivity in Multilayer Systems. *Journal of the Physical Society of Japan* **81**, 034702 (2012).

242. Lee, P. A. Amperean Pairing and the Pseudogap Phase of Cuprate Superconductors. *Phys. Rev. X* **4**, 031017 (2014).

243. Graf, J. *et al.* Bond Stretching Phonon Softening and Kinks in the Angle-Resolved Photoemission Spectra of Optimally Doped $Bi_2Sr_{1.6}La_{0.4}Cu_2O_{6+delta}$ Superconductors. *Phys. Rev. Lett.* **100**, 227002– (2008).

244. Chen, Y. L. *et al.* Massive Dirac Fermion on the Surface of a Magnetically Doped Topological Insulator. *Science* **329**, 659–662 (2010).

245. Zhang, Y. *et al.* Direct observation of the transition from indirect to direct bandgap in atomically thin epitaxial MoSe2. *Nat Nano* **9**, 111–115 (2014).

246. Yeh, P.-C. *et al.* Layer-dependent electronic structure of an atomically heavy two-dimensional dichalcogenide. *Phys. Rev. B* **91**, 041407 (2015).

247. Latzke, D. W. *et al.* Electronic structure, spin-orbit coupling, and interlayer interaction in bulk MoS_2 and WS_2. *Phys. Rev. B* **91**, 235202 (2015).

248. Mellnik, A. R. *et al.* Spin-transfer torque generated by a topological insulator. *Nature* **511**, 449–451 (2014).

249. Fan, Y. *et al.* Magnetization switching through giant spin-orbit torque in a magnetically doped topological insulator heterostructure. *Nat Mater* **13**, 699–704 (2014).

250. He, Q. L. *et al.* Tailoring exchange couplings in magnetic topological-insulator/antiferromagnet heterostructures. *Nat Mater* **16**, 94–100 (2017).